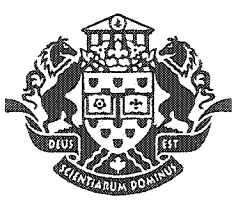

Université d'Ottawa · University of Ottawa

Université d'Ottawa · University of Ottawa

FACULTÉ DES ÉTUDES SUPÉRIEURES ET POSTDOCTORALES

FACULTY OF GRADUATE AND POSTDOCTORAL STUDIES

George PSOFOGIANNAKIS

AUTEUR DE LA THÈSE - AUTHOR OF THESIS

M. A. Sc. (Chemical Engineering)

GRADE - DEGREE

Department of Chemical Engineering

FACULTÉ, ÉCOLE, DÉPARTEMENT - FACULTY, SCHOOL, DEPARTMENT

TITRE DE LA THÈSE - TITLE OF THE THESIS

A Mathematical Model for a Direct Propane Phosphoric Acid Fuel Cell

M. Ternan

DIRECTEUR DE LA THÈSE - THESIS SUPERVISOR

Y. Bourgault

CO-DIRECTEUR DE LA THÈSE - THESIS CO-SUPERVISOR

EXAMINATEURS DE LA THÈSE - THESIS EXAMINERS

V. Hornof

A. Novruzi

J.-M. De Koninck, Ph.D.

LE DOYEN DE LA FACULTÉ DES ÉTUDES SUPÉRIEURES ET POSTDOCTORALES

SIGNATURE

DEAN OF THE FACULTY OF GRADUATE AND POSTDOCTORAL STUDIES

A Mathematical Model for a Direct Propane Phosphoric Acid Fuel Cell

GEORGE PSOFOGIANNAKIS

Thesis submitted to the
Faculty of Graduate and Postdoctoral Studies
in partial fulfillment of the requirements
for the degree of Master of Applied Science in Chemical Engineering

Department of Chemical Engineering
Faculty of Engineering
University of Ottawa

Your file Votre référence
ISBN: 0-612-89905-5
Our file Notre référence
ISBN: 0-612-89905-5

ABSTRACT

In direct hydrocarbon fuel cells, a hydrocarbon fuel is oxidised in the anode electrode. This thesis presents a mathematical model to predict the performance of a unit cell that utilises propane as the fuel, oxygen as the oxidant, phosphoric acid as the electrolyte, and platinum as the catalyst, supported on porous carbon electrodes. The phenomena considered include the electrochemical reactions of propane oxidation and oxygen reduction on platinum, the diffusion of the gases in gas-filled electrode pores, the dissolution and diffusion of dissolved gases in liquid-filled electrode pores as well as ionic conduction of protons. The model was based on the multi-layered physical structure of a modern unit fuel cell. The description of the physical structure of the gas diffusion electrodes was based on the concept of agglomerated catalyst particles filled with electrolyte and surrounded by gas-filled macropores. The performance of the cell was described by a different set of differential equations for each fuel cell layer and their numerical solution was based on an iterative technique known as "the shooting method".

The model was first applied to a phosphoric acid fuel cell cathode electrode and was found capable of simulating half-cell polarization curves for oxygen reduction reported in the literature. Two parameters were adjusted in order to fit the experimental data. Physically realistic values were used for these parameters. The model was used to study the magnitude of electrical potential losses contributed by the various processes (surface reaction, diffusion, ionic conduction) as a function of current density and oxygen conversion. It was also used to predict the effect of several critical operating conditions and electrode design parameters.

Subsequently, the model was applied to a direct propane-oxygen cell. The exchange current density for the oxidation reaction in the anode and the standard activation energy were estimated from experimental data. Using the chosen values for these parameters, the effects of phosphoric acid concentration and temperature on the polarization curves were accurately predicted. Possible performance improvements are suggested by the model-predicted performance of propane-oxygen cells at temperatures of ~200°C and high pressures on state-of-the-art Pt/C electrodes. The effects of platinum loading and catalyst layer thickness were considered. It was also found that the propane electro-oxidation reaction on platinum contributes the greatest loss of working potential in the cell.

ACKNOWLEDGEMENTS

I am deeply grateful to my thesis supervisor, Dr. Marten Ternan, for his continuous guidance, support and enthusiasm throughout this work, and for being an inspiring teacher for me.

I would also like to express my most sincere thanks to Dr. Yves Bourgault and Dr. Brian Conway for co-supervising my work, for their generous help, and invaluable suggestions and advice.

I am grateful to my mother, my father and my sister for their endless love and support.

TABLE OF CONTENTS

Abstract i
Acknowledgements ii
Table of Contents iii
List of Figures vi
List of Tables xi
Nomenclature xii

CHAPTER 1: INTRODUCTION TO DIRECT HYDROCARBON FUEL CELLS

1.1 A brief history of fuel cells 1
1.2 Fuel cells and how they operate – Physical description of a unit cell 2
1.3 Incentive for research on direct hydrocarbon fuel cells 5
1.4 Improving the performance of direct hydrocarbon fuel cells 7
1.5 Scope and limitations of research 8
1.6 Objectives of research 10
1.7 Review of direct hydrocarbon fuel cell literature-major findings 11
1.8 Review of literature related to phosphoric acid fuel cell cathode modeling 14

CHAPTER 2: MATHEMATICAL MODEL DEVELOPMENT

2.1 The structure of the catalyst layer: description and model assumptions 17
2.2 Estimation of some model-specific catalyst layer properties 19
2.3 Derivation of reaction-rate equations 25
2.4 Transport of gas-phase species 34
2.5 Ionic conduction 38

CHAPTER 3: DESCRIPTION OF COMPUTATIONAL METHOD

3.1 Summary of model equations 41
3.2 Boundary conditions 44
3.3 Simulation of half-cell polarization curves: Strategy 49

3.4 Simulation of cell polarization curves: Strategy ..... .50
3.5 Solution of the differential-algebraic equation system: the Shooting method ..... .51

CHAPTER 4: ELECTROCHEMICAL AND PHYSICOCHEMICAL PROPERTIES

4.1 Introduction ..... .55
4.2 Electrochemical parameters ..... .56
4.3 The diffusivity of oxygen in phosphoric acid ..... .58
4.4 The solubility of oxygen in phosphoric acid ..... .60
4.5 The diffusivity and solubility of propane in phosphoric acid ..... .62
4.6 Binary gas diffusion coefficients ..... .63
4.7 Knudsen diffusion coefficients ..... .64
4.8 The available specific surface area of platinum ..... .64
4.9 The activity of water in phosphoric acid ..... .66
4.10 The specific conductivity of phosphoric acid ..... .68
4.11 Porosity / tortuosity corrections for diffusivities and electrolyte conductivity ..... .70
4.12 Vapour pressure and boiling point of phosphoric acid ..... .71
4.13 Equilibrium potentials for the reactions ..... .74

CHAPTER 5: APPLICATION OF THE MODEL TO A PHOSPHORIC ACID FUEL CELL CATHODE

5.1 Introduction ..... .75
5.2 Comparison of model results with experimental data ..... .77
5.3 The magnitude of potential-loss contributing processes ..... .79
5.4 The effect of the extent of oxygen conversion on the potential losses ..... .85
5.5 The effect of operating conditions and electrode design parameters ..... .91
5.6 The effect of electrochemical and physicochemical model parameters (Sensitivity analysis) ..... .96

CHAPTER 6: APPLICATION OF THE MODEL TO A DIRECT PROPANE FUEL CELL

6.1 Introduction 102

6.2 Comparison of model results with experimental data 103
6.3 Model predictions of the performance of propane-oxygen cells utilizing Pt/C electrodes – Effects of operating conditions and electrode properties 109
6.4 The effect of some model parameters 114
6.5 The magnitude of electrical potential-loss contributing processes 117
6.6 Power density and fuel efficiency 119

CHAPTER 7: CONTRIBUTIONS TO ORIGINAL RESEARCH, CONCLUSIONS AND RECOMMENDATIONS

7.1 Contributions to knowledge 122
7.2 Conclusions 124
7.3 Recommendations 126

APPENDICES

A) Solution to equation 2.28 127
B1) MATLAB code for cathode model 130
B2) MATLAB code for anode model 141
B3) MATLAB code for potential loss across the electrolyte layer 152

References 154

LIST OF FIGURES

Figure 1.1: Propane fuel cell unit constituent layers 4

Figure 1.2: Unit cell coordinate system 9

Figure 2.1: Modeled physical structure of the catalyst layer 18

Figure 2.2: Schematic representation of agglomerate and liquid film showing the boundary conditions 26

Figure 3.1: Boundaries nomenclature and system variables (anode) 45

Figure 3.2: Boundaries nomenclature and system variables (cathode) 48

Figure 3.3: Normalised solution variables across the cathode electrode's catalyst layer and gas diffusion layer at convergence 54

Figure 4.1: Temperature dependence of oxygen diffusivity in phosphoric acid 59

Figure 4.2: Viscosity of phosphoric acid as a function of concentration 60

Figure 4.3: Temperature dependence of oxygen solubility in phosphoric acid 61

Figure 4.4: Solubility of oxygen in phosphoric acid as a function of concentration 61

Figure 4.5: Platinum surface-area as a function of the weight fraction of platinum in Pt/C catalyst 65

Figure 4.6: Molality of phosphoric acid solutions as a function of weight percentage 67

Figure 4.7: Activity of water in phosphoric acid as a function of solution molality 67

Figure 4.8: Specific conductivity of phosphoric acid as a function of concentration 68

Figure 4.9: Temperature coefficient of conductivity of phosphoric acid as a function of concentration 69

Figure 4.10: Water vapour pressure values corresponding to conditions of Table 4.3 72

Figure 4.11: Boiling point of phosphoric acid as a function of concentration 73

Figure 5.1: Performance curves for electrode A, reported by Kunz and Gruver (1975) and model predictions 78

Figure 5.2: Performance curves for electrode B, reported by Maoka (1988) and model predictions 79

Figure 5.3: Predicted performance curves for electrode A after successive elimination of various resistances....81

Figure 5.4: Predicted performance curves for electrode B after successive elimination of various resistances....81

Figure 5.5: Electrical potential distributions in the electrolyte in the catalyst layer for electrode B....83

Figure 5.6: Dissolved oxygen concentration distributions in an agglomerate and the surrounding liquid film for electrode A....84

Figure 5.7: Model predictions of contour lines for constant loss of electrical potential (volts) as a function of both local oxygen conversion (%) and local current density (A/cm^2)....86

Figure 5.8: Model predictions for contour lines of constant percent of electrical potential loss caused by cathode overpotential (surface polarization) as a function of local oxygen conversion (%) and local current density (A/cm^2)....87

Figure 5.9: Model predictions for contour lines of constant percent of electrical potential loss caused by ionic conduction (ohmic polarization) as a function of local oxygen conversion (%) and local current density (A/cm^2)....87

Figure 5.10: Model predictions for contour lines of constant percent of electrical potential loss caused by oxygen diffusion in the agglomerates as a function of local oxygen conversion (%) and local current density (A/cm^2)....88

Figure 5.11: Model predictions for contour lines of constant percent of electrical potential loss caused by oxygen diffusion in the liquid film surrounding the agglomerates as a function of local oxygen conversion (%) and local current density (A/cm^2)....88

Figure 5.12: Model predictions for contour lines of constant percent of electrical potential loss caused by oxygen diffusion in the gas phase in the catalyst layer and the gas diffusion layer as a function of local oxygen conversion (%) and local current density (A/cm^2)....89

Figure 5.13: Model predictions of polarization curves at different operating temperatures for electrode B, air feed....91

Figure 5.14: Model predictions of polarization curves at different gas pressures for electrode B, air feed 92

Figure 5.15: Model predictions of polarization curves for different phosphoric acid concentrations at constant operating temperature (160°C) for electrode A, air feed 93

Figure 5.16: Model predictions of polarization curves for different combinations of phosphoric acid concentration and operating temperature resulting in same water vapour pressure (0.9 atm) for electrode A, air feed 94

Figure 5.17: Effect of platinum loading (catalyst composition) on electrode performance 95

Figure 5.18: Polarization curves predicted by the model for different thicknesses of the electrode's catalyst layer (different platinum loading) for operation of electrode B in air 96

Figure 5.19: Effect of exchange current-density for oxygen reduction on electrode performance 98

Figure 5.20: Effect of cathodic transfer coefficient for oxygen reduction on electrode performance 98

Figure 5.21: Effect of agglomerate's radius on electrode performance 99

Figure 5.22: Effect of liquid film thickness on electrode performance 99

Figure 5.23: Effect of oxygen effective diffusion coefficient Do in the electrolyte-filled pores of the catalyst layer 100

Figure 5.24: Effect of oxygen solubility in the electrolyte on the performance of electrode B 100

Figure 5.25: Effect of the effective electrolyte's specific conductivity on the performance of electrode B 101

Figure 6.1: Experimental data and model results for H_2/O_2 cells used in by Grubb and Michalske (1964). Platinum loading is 45 mg/cm^2 on cathode 104

Figure 6.2: Experimental data (Grubb and Michalske, 1964) and model predictions for C_3H_8/O_2 cells for different phosphoric acid concentrations 105

Figure 6.3: Normalised residuals for model predictions of Figure 6.2 106

Figure 6.4: Variance of model predicted curves of Figure 6.2 for the four curves corresponding to four different acid concentrations as a function of acid concentration 106

Figure 6.5: Experimental data (Grubb and Michalske, 1964) and model predictions for C_3H_8 / O_2 cells for different combinations of phosphoric acid concentration and temperature 107

Figure 6.6: Normalised residuals for model predictions of Figure 6.5 108

Figure 6.7: Variance of model predicted curves of Figure 6.5 for the four curves corresponding to four different temperature / acid concentration combinations as a function of temperature 109

Figure 6.8: Predicted performance curves for C_3H_8/O_2 cells for Pt/C electrodes, 200°C, 95% H_3PO_4, 1 atm and 20% utilization 110

Figure 6.9: Predicted effect of reactant gas pressure on performance of C_3H_8/O_2 cells, 200°C, 95% H_3PO_4, 20% utilization 111

Figure 6.10: Predicted effect of reactant gas utilization on performance of C_3H_8/O_2 cells, 200°C, 95% H_3PO_4, 1 atm, 5 mg Pt/cm^2 112

Figure 6.11: Predicted effect of temperature on performance of C_3H_8/O_2 cells for Pt/C electrodes, 10 atm, 5 mg Pt / cm^2 113

Figure 6.12: Predicted performance curves for C_3H_8 cells for Pt/C electrodes, 200°C, 95% H_3PO_4, 1 atm, 20% utilization, 5 mg Pt/cm^2: (1) oxygen cathode; (2) air cathode 113

Figure 6.13: Predicted electrode potential loss at 200°C, 1 atm for: (1) an oxygen cathode, 1mg Pt/ cm^2; (2) an air cathode, 1mg Pt/ cm^2; (3) a propane anode, 4mg Pt/ cm^2 114

Figure 6.14: Predicted effect of exchange current-density on the performance of a propane anode electrode 115

Figure 6.15: Predicted effect of anodic transfer coefficient for the oxidation reaction on the performance of a propane anode electrode 116

Figure 6.16: Effect of agglomerate radius on the predicted performance of propane anode electrode 117

Figure 6.17: Predicted polarization curve for propane anode (200°C, 1 atm, 4 mg Pt/ cm^2) after successive elimination of various resistances at 20% local propane conversion.....118

Figure 6.18: Predicted polarization curve for propane anode (200°C, 1 atm, 4 mg Pt/ cm^2) after successive elimination of various resistances at 80% local propane conversion.....119

Figure 6.19: Predicted power density versus current-density curve for a propane/oxygen cell utilizing Pt/C electrodes and 95% phosphoric acid electrolyte at 200°C, 1atm pressure and 5 mg Pt/cm^2 total platinum loading.....120

Figure 6.20: Predicted energy conversion efficiency versus current-density curve for a propane/oxygen cell utilizing Pt/C electrodes and 85% phosphoric acid electrolyte at 150°C, 5 mg Pt/cm^2 total platinum loading and; (1) 1 atm pressure; (2) 10 atm pressure.....121

LIST OF TABLES

Table 4.1: Platinum surface area for different platinum / carbon catalyst concentrations....65

Table 4.2: Molality, mole fraction and activity of water in phosphoric acid of different concentrations....66

Table 4.3: Data of equilibrium water vapour pressure of phosphoric acid for different temperatures and acid concentrations....72

Table 4.4: Boiling point of phosphoric acid for different solution concentrations....73

Table 5.1: Electrode properties and operating conditions for electrodes A and B reported in the literature....78

Table 5.2: Physicochemical and electrochemical parameters used or calculated for electrode B....97

Table 6.1: Electrode parameters corresponding to Figure 6.8 polarization curves....110

Table 6.2: Physicochemical and electrochemical parameters used in the simulation of propane anode electrode....115

NOMENCLATURE

Any symbols not appearing in the following list are explained in the text. The units for the following quantities are not SI units. They are the units used in the equations in the text and the computer program (cm, g were more convenient quantities in the calculations than m, kg):

$\bar{V}$: Molar volume (cm^3 / mole)

a_a: Anodic transfer coefficient for the oxygen reduction reaction or propane oxidation reaction

a_c: Cathodic transfer coefficient for the oxygen reduction reaction or propane oxidation reaction

a_W: Activity of water in phosphoric acid solution

c*: Solubility of reactant gas in H_3PO_4 at 1 atm reactant gas partial pressure (moles / cm^3atm)

$c^*_{O2,\ 98\%}$: Solubility of oxygen in 98 wt%H_3PO_4 at 1 atm partial pressure (moles / cm^3atm)

c: Concentration of dissolved reactant gas at any position r within agglomerates (moles/cm^3)

c_{CO2}: Carbon dioxide concentration in gas-filled pores (moles /cm^3)

$c_{CO2(GC)}$: Concentration of carbon dioxide in the anode gas channel (moles /cm^3)

c_G: Reactant gas concentration in the gas-filled electrode pores (moles/cm^3)

c_i: Reactant gas concentration at the agglomerate / liquid film boundary (moles/cm^3)

c_k: Concentration of component k in the gas phase (moles / cm^3)

c_{N2}: Nitrogen concentration in gas-filled pores (moles /cm^3)

$c_{N2(GC)}$: Nitrogen concentration in the cathode gas channel (moles /cm^3)

c_{O2}*: Solubility of oxygen in H_3PO_4 at 1 atm partial pressure (moles / cm^3atm)

c_{O2}: Oxygen concentration in gas-filled pores (moles /cm^3)

$c_{O2(GC)}$: Concentration of oxygen in the cathode gas channel (moles /cm^3)

c_P*: Solubility of propane in H_3PO_4 at 1 atm partial pressure (moles / cm^3atm)

c_P: Propane concentration in gas-filled pores (moles /cm^3)

$c_{P(GC)}$: Concentration of propane in the anode gas channel (moles /cm^3)

c_T: Total concentration of gas mixture in electrode pores (moles / cm^3)

c_W: Water vapour concentration in gas-filled pores (moles /cm^3)

D: Diffusivity of reactant gas in the electrolyte (cm^2/s)

$D_{CO2/W}$: Binary diffusion coefficient between carbon dioxide and water vapour (cm^2/s)

D_{CO2}^{K}: Effective Knudsen diffusivity of carbon dioxide is gas pores (cm^2/s)

D_e: Effective diffusivity of reactant gas within agglomerates (cm^2/s)

$D_{k,e}^{K}$: Effective Knudsen diffusivity of gas mixture component k (cm^2/s)

$D_{km,e}$: Effective binary molecular diffusion coefficient between components k and m (cm^2/s)

$D_{N2/W}$: Binary diffusion coefficient between nitrogen and water vapour (cm^2/s)

$D_{O2,98\%}$:Diffusivity of oxygen in 98% phosphoric acid (cm^2/s)

$D_{O2,e}$: Effective diffusivity of oxygen in electrolyte-filled pores in agglomerates (cm^2/s)

$D_{O2/N2}$: Binary diffusion coefficient between oxygen and nitrogen (cm^2/s)

$D_{O2/W}$: Binary diffusion coefficient between oxygen and water vapour (cm^2/s)

D_{O2}: Diffusivity of oxygen in phosphoric acid (cm^2/s)

D_{O2}^{K}: Effective Knudsen diffusivity of oxygen is gas pores (cm^2/s)

$D_{P,e}$: Effective diffusivity of propane in electrolyte-filled pores in agglomerates (cm^2/s)

$D_{P/CO2}$: Binary diffusion coefficient between propane and carbon dioxide (cm^2/s)

$D_{P/W}$: Binary diffusion coefficient between propane and water vapour (cm^2/s)

D_P: Diffusivity of propane in phosphoric acid (cm^2/s)

D_P^{K}: Effective Knudsen diffusivity of propane is gas pores (cm^2/s)

E: Electrode potential (Volts)

$E_{EQ,AN}$: Equilibrium potential for propane oxidation reaction

$E_{EQ,CAT}$: Equilibrium potential for oxygen reduction reaction

E_{EQ}: Equilibrium potential for oxygen reduction reaction or propane oxidation reaction

F: Faraday's constant (96487 Cb /equivalent)

f: The fraction of total pore volume that is micropores in the catalyst layer = volume of micropores / total pore volume

$F_{A,MAX}$: F_A at which all micro-pores in catalyst layer are filled

F_A: Fraction of acid occupation = volume of liquid in pores / pore volume of catalyst layer

i: Current-density per unit area of platinum (amp /cm^2 Pt)

I: Current produced (transferred) per unit electrode face area (amp / cm^2 electrode)

i_o*: Exchange current-density at the reference temperature T*(amp / cm^2 Pt)

i_o: Exchange current-density for the oxygen reduction reaction or propane oxidation reaction on platinum at the specified temperature (amp/cm^2 Pt)

i_{oo}: Exchange-current density at 298K (amp/cm^2 Pt)

i_{VA}: Current transferred per unit volume of agglomerate (amp /cm^3)

K: Henry's law constant for oxygen or propane in phosphoric acid ((moles/ cm^3 in liquid) / (moles / cm^3 in gas))

K_{O2}: Henry's law constant for oxygen in phosphoric acid ((moles/ cm^3 in liquid) / (moles / cm^3 in gas))

K_P: Henry's law constant for propane in phosphoric acid ((moles/ cm^3 in liquid) / (moles / cm^3 in gas))

k: Specific conductivity of electrolyte (S/cm)

k_e: Effective specific conductivity of electrolyte in electrode pores (S/cm)

L: Thickness of catalyst layer (cm)

L_{EL}: Thickness of electrolyte layer (cm)

L_F: Thickness of liquid film (cm)

L_{GDL}: Thickness of gas diffusion layer (cm)

m: Molality of phosphoric acid solution (moles H_3PO_4 / kg H_2O)

M: Molecular mass (g /mole)

M_C: Mass of carbon per unit electrode area (g C / cm^2)

M_{Pt}: Platinum loading per unit electrode surface area (g Pt / cm^2 electrode)

M_T: Mass of PTFE per unit electrode area (g PTFE / cm^2)

N: Dissolved reactant gas flux (moles / cm^2s)

n: Number of equivalents transferred per mole of reactant consumed (n = 4 for oxygen reduction, n = 20 for propane oxidation)

N_+: Ionic current density (amp/cm^2)

N_A: Total agglomerate density = number of agglomerates per unit volume catalyst layer (agglomerates / cm^3)

N_{CO2}: Flux of carbon dioxide in the gas-filled electrode pores (moles / cm^2s)

N_k: Flux of component k of gas mixture in the gas-filled electrode pores (moles / cm^2s)

N_{N2}: Flux of nitrogen in the gas-filled electrode pores (moles / cm^2s)

N_{O2}: Flux of oxygen in the gas-filled electrode pores (moles / cm^2s)

N_P: Flux of propane in the gas-filled electrode pores (moles / cm^2s)

N_{uA}: Utilised agglomerates' density = number of utilised agglomerates per unit volume catalyst layer (agglomerates filled with liquid / cm^3)

N_W: Flux of water vapour in the gas-filled electrode pores (moles / cm^2s)

r: Coordinate within agglomerate (measured from center)

R: Ideal gas constant (8.3143 J/moleK)

R_+: Volumetric rate of production of ionic charge in catalyst layer (Cb / cm^3s = A / cm^2)

R_A: The agglomerates' radii (cm)

R_{AG}: Reaction rate in one agglomerate = moles reactant gas consumed in one agglomerate / unit time (moles/s)

$R_{V,AN}$: Volumetric reaction rate in the anode catalyst layer (moles/cm^3s)

$R_{V,CAT}$: Volumetric reaction rate in the cathode catalyst layer (moles/cm^3s)

R_V: Volumetric reaction rate in the catalyst layer = moles reactant gas consumed / unit volume catalyst layer/unit time (moles/cm^3s)

R_{VA}: Volumetric reaction rate within one agglomerate (moles reactant gas consumed / unit volume of agglomerate/unit time) (moles/cm^3s)

S: The surface area per unit mass of platinum that is available for reaction (cm^2 Pt / g Pt)

S_A: Surface area of platinum per unit volume in agglomerate

S_T: Total surface area of platinum per unit electrode face surface area (cm^2Pt / cm^2 electrode)

S_V: Surface area of platinum per unit volume in the catalyst layer

T: Temperature (K)

T_B: Boiling point of phosphoric acid solution (°C)

u: Fraction of agglomerates that are utilised = fraction of micropores' volume that is filled with electrolyte

V_A: Volume fraction of agglomerates in the catalyst layer = volume occupied by agglomerates / total volume of catalyst layer

V_C: Volume fraction of carbon in the catalyst layer = volume occupied by C / total volume of catalyst layer

V_F: Volume fraction of liquid films in the catalyst layer = volume occupied by liquid films / total volume of catalyst layer

V_G: Volume fraction of gas in the catalyst layer = volume occupied by gas / total volume of catalyst layer

V_L: Volume fraction of liquid in the catalyst layer = volume occupied by liquid / total volume of catalyst layer

V_m: Volume fraction of micropores in the catalyst layer = volume occupied by micropores / total volume of catalyst layer

V_{mA}: Volume fraction occupied by micropores in agglomerate = agglomerates' porosity

V_P: Volume fraction of pores in the catalyst layer = volume occupied by pores / total volume of catalyst layer

V_{Pt}: Volume fraction of platinum in the catalyst layer = volume occupied by Pt / total volume of catalyst layer

V_S: Volume fraction of solid in the catalyst layer = volume occupied by solid / total volume of catalyst layer

V_T: Volume fraction of PTFE in the catalyst layer = volume occupied by PTFE / total volume of catalyst layer

V_{uA}: Volume fraction of utilised agglomerates in the catalyst layer = volume occupied by utilised agglomerates / total volume of catalyst layer

W: The weight percentage of phosphoric acid solution

W_{Pt}: Weight fraction of platinum in catalyst = mass of Pt / mass of (Pt+C)

W_T: Weight fraction of Teflon in catalyst layer = mass of PTFE / mass of (Pt+C+PTFE)

x_m: Mole fraction of component m in gas mixture (moles m / total moles)

x_W: Mole fraction of water vapour in equilibrium with phosphoric acid solution

z: Coordinate along catalyst layer or gas diffusion layer (increasing towards the electrolyte side of electrode)

z_0: Boundary between gas channel and gas diffusion layer

z_1: Boundary between gas diffusion layer and catalyst layer

z_2: Boundary between catalyst layer and electrolyte layer

Greek symbols

α_T: Temperature coefficient of specific conductivity (1/K)

$\Delta G^{\ddagger}$: Activation energy for the exchange current density for the oxygen reduction reaction or the propane oxidation reaction (Joules/mole)

$\Delta\Phi_{EL}$: Electrical potential difference between the two sides of the electrolyte layer (between z_2 of anode electrode and z_2 of cathode electrode)

μ: Viscosity of phosphoric acid (cP)

$\mu_{98\%}$: Viscosity of 98 wt% phosphoric acid (cP)

η: Local overpotential (Volts)

ρ_C: The density of solid carbon (g/cm^3)

ρ_{Pt}: The density of solid platinum (g/cm^3)

ρ_T: The density of solid PTFE (g/cm^3)

Φ_S: Electrical potential of the electrode's solid phase (Volts)

Φ_E: Electrical potential in the electrolyte (Volts)

Ψ: Quantity defined by equation 2.30

Subscripts

A or AG: agglomerate
AN: anode
C: carbon
CAT: cathode
e: effective property
E: electrolyte
EQ: equilibrium
F: Film
G: Gas
i: interfacial
L: Liquid
m: micropores
P: propane
Pt: platinum
S: Solid
T: Teflon
u: utilized
V: volumetric

Superscripts

i: Iteration number
K: Knudsen

CHAPTER 1: INTRODUCTION TO DIRECT HYDROCARBON FUEL CELLS AND LITERATURE REVIEW

1.1 A brief history of fuel cells

The fuel cell was discovered in 1839 by Sir William Grove. He described the production of electricity from hydrogen and oxygen supplied separately on platinum foils immersed in a sulphuric acid electrolyte and used his apparatus in order to decompose water (Grove, 1839, Grove, 1842). Mond and Langer (1889) advanced the hydrogen fuel cell and were able to obtain greater reactivity by using powdered platinum-black electrocatalyst, current collectors and porous electrolyte matrices (Liebhafsky and Cairns, 1968). They were the first to recognize that fossil fuels can be treated to supply hydrogen and that the fuel cell can be used as an all-purpose source of electrical energy (Liebhafsky and Cairns, 1968). Haber (1905) was the first to recognize and show that the maximum attainable terminal voltage of a cell corresponds to the thermodynamic reversible potential of the overall reaction.

At the end of the 19^{th} century the dream of producing electrical energy directly from coal led to further research on fuel cells. Significant but ultimately unsuccessful attempts to realize this objective were made by various workers, including Jacques (1896) and Baur (1910). Baur made significant contributions in developing good oxygen electrodes and in achieving good cell design (Liebhafsky and Cairns, 1968). Research on fuel cells was gradually shifted towards the use of hydrogen after it was realized that hydrogen reacts much more readily in the anode. A very important technical development was the replacement of flat electrodes with porous electrodes, which came mainly as a result of the experimental work of Schmid (1923). The use of porous electrodes, in which the reactant gas, the liquid electrolyte and the electrocatalyst co-exist, greatly improved the attainable current density of a fuel cell.

During the early 1930's, F.T.Bacon devised the first successfully operating fuel cell with alkaline electrolyte and nickel electrodes. He continued working on modifying his design until the 50's, and ultimately succeeded in producing multi-kilowatt power from the first practical working type of fuel cell, the Bacon cell (Bacon, 1960). Bacon's pioneering work paved the way toward the modern state of fuel cell development. In the early 1960's the first proton-exchange membrane fuel cell was developed by General Electric and was used in NASA's Gemini space project

(Bockris, 1969). That was the first important use of a fuel cell. Meanwhile, the Bacon alkaline cell was further developed (Bockris, 1969) and used in the Apollo spacecraft missions and subsequently in the Space Shuttle flights.

Since then, constant developments have led to fuel cells being used in a wide variety of terrestrial applications. From the time of William Grove's discovery until now, understanding of the phenomena in fuel cells through advancements in the areas of thermodynamics, electrode kinetics and transport processes, and their application on fuel cell research, has provided the greatest aid in their continuous and on-going development.

It should be noted that Canada is one of the world's leading countries in research and development of fuel cell systems. For example, Ballard Co. is specializing in research and development of polymer electrolyte membrane (PEM) fuel cells for many diverse applications, including buses powered by fuel cells and power back-up systems for residential and industrial use.

1.2 Fuel Cells and how they operate – Physical description of a unit cell

A fuel cell is a device that converts the chemical energy of a fuel directly into electrical energy. The main components of a fuel unit cell are an anode electrode, a cathode electrode and the electrolyte. A fuel, such as hydrogen or a hydrocarbon, is supplied to the anode and is electrochemically oxidized. An oxidant, such as oxygen or air, is supplied to the cathode and is electrochemically reduced. The anode and cathode of a fuel cell are connected by an external electrical circuit containing an electrical load that consumes the generated energy. The electrons produced in the anode of the fuel cell flow through the electronically conducting anode material to the external circuit. The purpose of the electrolyte is to conduct ionic species (such as protons) from one side of the fuel cell to the other without permitting the electrodes to be in physical contact and therefore cause a short circuit. The ions of the electrolyte are also required to establish the potential difference at the interface of each electrode, across which charge transfer takes place.

The overall reaction taking place in a fuel cell is equivalent to a combustion reaction. The difference is that in a fuel cell the oxidation of a fuel and the reduction of the oxidant are spatially

separated in order to convert part of the free energy of reaction to electrical energy rather than thermal energy. For example, the overall reaction for the electrochemical oxidation of propane is:

$$C_3H_8 + 5O_2 \rightarrow 3CO_2 + 4H_2O \qquad \text{(Reaction 1)}$$

However, in a fuel cell this reaction happens through two so-called half-cell reactions. On the catalytic anode surface propane is oxidized to carbon dioxide, producing electrons (which flow through the external circuit) and protons, which are conducted through the electrolyte from the anode to the cathode of the fuel cell (Bockris, 1969):

$$C_3H_8 + 6H_2O \rightarrow 3CO_2 + 20H^+ + 20e^- \qquad \text{(Reaction 2)}$$

On the catalytic cathode surface oxygen is reduced to water by electrochemically combining with the conducted protons and electrons flowing through the external circuit from the propane anode (Bockris, 1969):

$$5O_2 + 20H^+ + 20e^- \rightarrow 10H_2O \qquad \text{(Reaction 3)}$$

In fuel cell systems, several units are connected together side by side to form a stack, with the anode of one unit in electrical contact with the cathode of the adjacent unit. Different ways are used to connect the unit cells; monopolar and bipolar designs are discussed by Carrette et al (2001). Details of stack designs are not discussed here because the model concentrates on a unit cell. The physical structure of unit cells has been described in the literature (Hirschenhofer *et al*, 1998, Appleby and Foulkes, 1989, Carrette *et al*, 2001). A modern unit cell consists of several physically distinct layers. The most common design for a liquid electrolyte unit cell for gaseous fuels is shown in **Figure 1.1**. The common multi-layer design is also similar for membrane-electrolyte fuel cells, where an ion-exchange membrane forms the electrolyte layer between the electrodes (Ralph and Hogarth, 2002).

On the two sides of the fuel unit cell, the fuel in the anode and the oxidant in the cathode flow in gas channels (also called flow channels) in a parallel direction to the electrodes' outer surfaces. The gas channel gases also contain the products of the electrochemical reactions, such as carbon dioxide for a hydrocarbon fuel cell, and water vapour. The channels are usually machined into a solid graphite plate (also called a flow field plate). Different designs for flow-field plates, in

which the etched channels follow complex geometric patterns, have been described in the literature (Carrette *et al*, 2001).

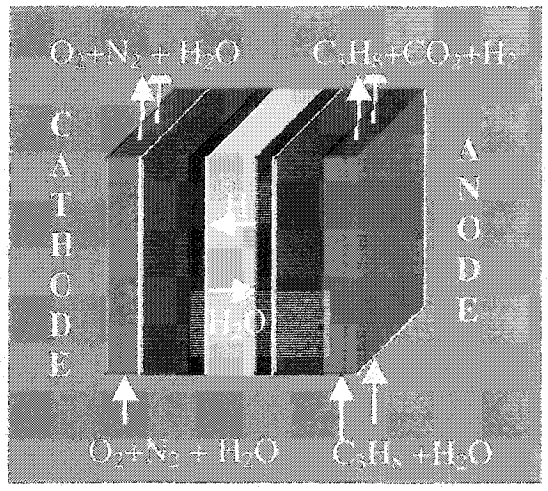

Figure 1.1: Propane fuel cell unit constituent layers (Gas channels = grey, gas diffusion layers = red, reaction layers = black, electrolyte layer = blue)

The fuel in the anode and the oxidant in the cathode are transported to the catalytic zone through a porous structure that contains no catalyst and is called the gas diffusion layer or gas diffuser. The purpose of the gas diffusers is to provide mechanical stability because the solid layers in which the reactions are happening in fuel cells (the catalyst layers) are extremely thin. Another advantage of using gas diffusers is that they help in distributing the reactant gases more evenly to the catalytic sites. Gas diffusers in modern fuel cell electrodes are usually made of porous carbon cloth or carbon paper.

The next layer of each electrode (anode and cathode), proceeding inwards, is the reaction (or catalyst) layer. It is a thin porous solid structure, on whose pore walls the electrocatalyst is dispersed. The solid is usually carbon because it is a good electrical conductor, has good catalyst support properties (such as high pore surface area per unit mass) and is chemically resistant to the electrolyte. In the case of liquid electrolytes, some of the pores of the catalyst layer are filled with gas while others are filled with liquid electrolyte. Smaller pores are penetrated by liquid because of capillary forces, while larger ones provide gas channels for the reactants and products. The presence of hydrophobic PTFE particles also inhibits the flooding of larger pores. The catalyst layer is a complex three-phase structure (it contains solid, liquid and gas), inside which the reactant gases dissolve in the liquid electrolyte and travel short diffusion paths towards the catalytic sites.

The innermost layer of a unit cell is the electrolyte. In fact, fuel cells are usually categorized according to the electrolyte used, which can be liquid or solid. The five most common types of fuel cells are the phosphoric acid fuel cell (commonly abbreviated PAFC), the alkaline fuel cell (AFC), the molten carbonate fuel cell (MCFC), the polymer electrolyte membrane fuel cell (PEM) and the solid oxide fuel cell (SOFC), all of which are named according to the type of electrolyte that is used to transport the ionic current. In phosphoric acid fuel cells, on which this model is based, concentrated solutions are usually used. The phosphoric acid is contained in a highly porous silicon carbide (SiC) matrix (Carrette *et al*, 2001, Appleby and Foulkes, 1989, Hirschenhofer *et al*, 1998).

1.3 Incentive for research on direct hydrocarbon fuel cells

Hydrocarbon fuels can be used either directly or indirectly in fuel cells. The term 'direct' hydrocarbon fuel cell is used for a cell in which the hydrocarbon is oxidized directly on the catalyst surface in the anode compartment of the cell and is used to distinguish it from the 'indirect' hydrocarbon fuel cell. In the latter type of fuel cells, the fuel is first converted to hydrogen in a separate reformer before entering the fuel cell and the resulting fuel that is oxidized is the hydrogen. Reforming of hydrocarbons is also the principal method for production of hydrogen. When this is a separate process and not an integral part of the fuel cell system the term 'hydrogen fuel cell' is used.

As mentioned above, large-scale hydrogen production, including hydrogen for fuel cells, is currently done by reforming hydrocarbons (Cameron, 2002). The primary sources of hydrogen include natural gas, petroleum products (e.g. naptha), and coal liquids and gases (Hirschenhofer *et al*, 1998). In indirect hydrocarbon fuel cells, hydrogen is produced from a hydrocarbon in a fuel cell system. Consequently, if hydrocarbons fed directly into a cell exhibited comparable performance with hydrogen fuel, the need for the reforming process would be eliminated. This would lower the cost of the overall process. In indirect hydrocarbon fuel cells, the reformer adds to the cost, size, weight and efficiency losses of the fuel cell system. In comparison to direct use of hydrogen, several disadvantages associated with fuel storage and transportation would be avoided by employing hydrocarbon fuel cells. Several common hydrocarbons can be stored in liquid form and the infrastructure for their transportation and storage already exists.

With respect to environmental issues, carbon dioxide, which is a greenhouse gas, is emitted by a direct hydrocarbon fuel cell. Unreacted fuel and trace amounts of other species that are present in the fuel will also be emitted. In comparison to conventional power production technology, the environmental advantages of fuel cells are well-known. Hydrogen fuel cells produce seemingly no pollutants. However, it is critical to note that carbon dioxide is emitted in the reforming process to generate hydrogen. When hydrogen is produced, every atom of carbon in the hydrocarbon is emitted as a carbon dioxide molecule. If hydrocarbons are oxidized directly in the anode of a direct hydrocarbon fuel cell, each carbon atom will also be emitted as a carbon dioxide molecule. The efficiency can be used to compare the oxidation of hydrogen with the oxidation of hydrocarbons. The process that is more efficient will emit less carbon dioxide. This means that the efficiency of the reforming process to produce hydrogen should be taken into account when hydrogen oxidation is compared to hydrocarbon oxidation in a fuel cell.

However, the oxidation of hydrogen in fuel cells produces larger current densities than the oxidation of hydrocarbons on common fuel cell catalysts, such as platinum. Greater operating power levels can be achieved by using hydrogen instead of hydrocarbons because hydrogen oxidation is electrochemically simpler. However, the increased performance of hydrogen fuel cells can be attributed partly to the continuous and ongoing world-wide research effort on this system for several decades. On the other hand, direct hydrocarbon fuel cells have not been given much attention by the scientific community in the last three decades.

In general, fuel cells can be used for a wide variety of applications, the most important of which are as a power source for vehicles, as a stationary power source (for example for large-scale power generation, power generation in the home or small power plants for larger industrial or residential sites) and as a power source for portable devices (for example laptops, cameras, mobile phones, for replacement of batteries etc.).In principle, hydrocarbon fuel cells could be candidates for all these categories, especially the first two. Natural gas and propane are attractive for stationary applications since they are low-cost fuels and the infrastructure for their transportation already exists. For mobile applications, higher hydrocarbons that can be stored as liquids could become the fuel of choice. The heat generated in a fuel cell developed for these applications may be also useful (for example, for heating requirements in a building). In this way the overall efficiency of the fuel cell is improved.

1.4 Improving the performance of direct hydrocarbon fuel cells

There are three major aspects related to improving the performance of direct hydrocarbon fuel cells. The first is the electrocatalysis aspect related to the oxygen reduction reaction in the cathode of the fuel cell. This reaction is quite slow (irreversible) on all electrocatalysts that have been examined and suffers from the fact that the open-circuit voltage for the cathode in a fuel cell is much lower than the thermodynamic equilibrium potential for oxygen reduction. As a consequence, the overpotential contributed by the oxygen reduction reaction is the major source of power loss in the hydrogen fuel cell. However, the electrocatalytic aspects of this reaction continue to be actively investigated because the cathodic reaction is similar in practically all fuel cells and several catalysts are being tested and developed. The most common catalyst for the reaction for intermediate temperature fuel cells is platinum or platinum alloys supported on carbon (Appleby and Foulkes, 1989, Hirschenhofer *et al*, 1998).

The second aspect is the electrocatalyst for the hydrocarbon oxidation reaction in the anode. Earlier research had shown that the reaction can only proceed on platinum at appreciable rates (Cairns, 1971).Very little research has been done since that time. Alloys of platinum and other catalysts have not been thoroughly tested. Much less experimental work has been done for the electrocatalysis of hydrocarbon oxidation than for oxygen reduction.

The third aspect is optimization of the fuel cell with respect to the operating conditions (temperature, pressure and flowrate of the reactant gases), the electrode structure and design parameters (surface area and thickness of the electrode and catalyst loading) and the electrolyte parameters, such as the concentration of a liquid electrolyte. At the present time, electrodes of a wide range of properties can be prepared. Electrode manufacturers can usually prepare electrodes having properties in accordance to the needs of optimized performance. For this reason, mathematical modeling, the subject of the present thesis, has become a significant part of fuel cell research.

Numerical simulations for the prediction of the performance and optimization of hydrogen or methanol fuel cells for different fuel cell types (membrane, solid oxide or acid electrolyte) appear frequently in the current scientific literature. However, to the best of the author's knowledge, the present work is the first numerical simulation of the performance of a direct hydrocarbon fuel cell that has ever been attempted.

1.5 Scope and limitations of research

Because various fuel cell systems (with respect to electrolyte, fuel and catalyst) behave differently, it was necessary to make specific choices on the exact fuel cell system on which this mathematical model would be based. The model developed in the present work attempts to describe the performance of a unit cell that utilizes propane as the fuel, phosphoric acid as the electrolyte, oxygen or air as the oxidant and platinum supported on carbon as the electrocatalyst.

Propane is a common gaseous fuel which can be stored in liquid form in pressure vessels and is especially advantageous for distributed power applications. Moreover, research has shown that it can be more efficiently oxidised than all other saturated hydrocarbons. In his review article for direct hydrocarbon fuel cells, Cairns (1971) presents plots of relative current densities at constant potential (an indication of performance) for n-alkanes in the range C1-C8. Regardless of the electrolyte, the performance is maximised in these plots at the data points corresponding to propane. Pure oxygen or oxygen in air is the obvious choice for the oxidant. The phosphoric acid electrolyte fuel cell is the most well developed of all different types of cells and it is also the first type, operating with hydrogen, which became commercially available. Cairns (1971) notes that the most promising practical results in hydrocarbon fuel cells have been achieved using strong acid electrolytes (H_3PO4, HF, H_2SO_4 and $HClO_4$).

Platinum is the most reactive catalyst for the oxidation of hydrocarbons. Cairns (1971) notes that no other element has shown activity superior to that of platinum for the direct oxidation of hydrocarbons. His statement is supported by presentation of experimental data on the performance of several catalysts for hydrocarbon oxidation. Platinum is the most active catalyst in many fuel cell reactions, including the anode and cathode reactions in the hydrogen fuel cell (Hirschenhofer *et al*, 1998). In modern fuel cells, the metal catalyst is dispersed inside the pores of a carbon support, in order to increase the accessible surface area per unit mass of catalyst and thereby to reduce the actual amount of catalyst required in the electrode to achieve a given performance.

The model developed in this work is a one-dimensional steady-state model. The direction along which the model was developed is that of the z-coordinate shown in **Figure 1.2**, separately for the two electrodes. The z-direction is normal to the electrode's face area. Dimension y is the direction

of gas flow in the gas channels and is also important. As the gases in the anode gas channel of the fuel cell flow upwards in direction y, the concentrations of the gases (partial pressures) change with position: the concentration of propane is reduced while the concentration of carbon dioxide is increased. Similarly, the concentration of oxygen in the cathode gas channel is reduced as the gas flows upwards in direction y. Because the electrochemical reaction rate depends on the reactants' concentrations, the rate of reaction and therefore the power produced in the fuel cell are decreased with position along the coordinate y. For the one-dimensional model, the concentration (or mole fraction and total pressure) of the gases in the gas channels has to be given as input data in the model.

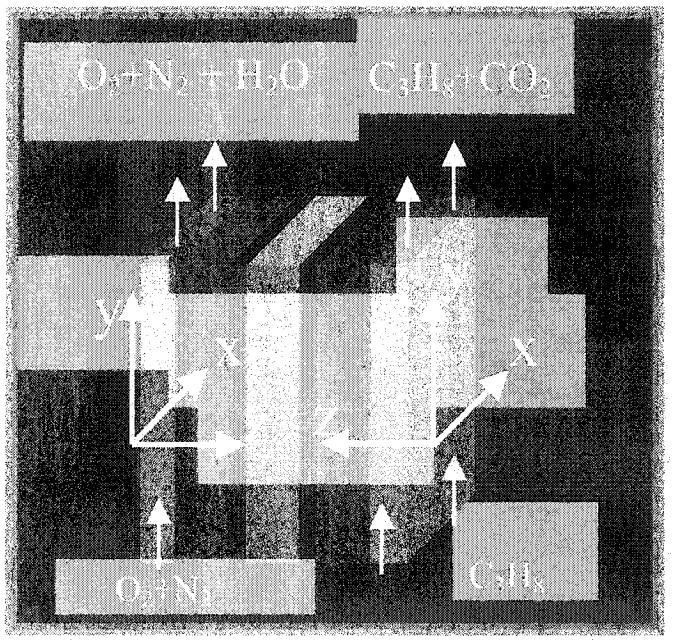

Figure 1.2: Unit cell coordinate system

The one-dimensional model is capable of calculating the current density and power density produced and other important parameters at a certain y-position where the concentration of the gases in the gas channel is known. In other words, the one dimensional model cannot account for the height Y of the fuel cell required for the concentrations of the gases in the gas channels' exit to have a certain concentration (conversion). However, it is capable of evaluating the local current density produced at any position y, where the local degree of conversion has been specified. Considering the complexity of the whole system, it was decided that a one-dimensional model is a good starting point for describing the phenomena of the direct propane fuel cell.

The model described in this work also assumes that there exist no temperature gradients across the fuel cell. In reality, small temperature gradients may develop across the fuel cell unit because

the reaction rates are different at different positions in the fuel cell (in the z-direction for the one-dimensional model) and the electrochemical reactions normally produce heat in addition to electricity. These temperature gradients are not expected to be large in a single cell mainly because of the fact that a unit cell is an extremely thin structure. The effects of spatial temperature differences and temperature changes with time are certainly more significant in fuel cell stacks, where the issue of cooling of the fuel cell has to be taken into account.

The model described in this work is a steady-state model. For this reason, start-up effects, the time required for steady-state to be achieved and the response of the system to any dynamic changes in operating conditions cannot be analyzed by this model.

The initial scope of this work was to simulate the performance of a direct hydrocarbon fuel cell. However, the model that was developed can also be used advantageously to simulate the performance of each of the electrodes (anode and cathode) separately. It was then decided to also use the model in order to simulate the performance of a phosphoric acid fuel cell cathode separately. This electrode has been studied extensively in conjunction with research for hydrogen fuel cells. However, several important refinements over other existing models and contributions were possible from this work. These are clearly stated in Chapter 7.

1.6 Objectives

The general objectives of this work were: 1) To develop and solve a mathematical model that describes the performance of the propane fuel cell system described in the previous section. 2) To develop a mathematical model that describes the performance of an oxygen cathode fuel cell electrode. 3) To compare the results of the two models (propane cell and oxygen cathode) with experimental data that have been published in the literature. 4) To use the models in order to predict the effect of the variables that influence the performance of the propane cell and the cathode electrode separately. These include the electrode characteristics (electrode thickness, catalyst loading and catalyst composition), the operating conditions (temperature, pressure of reactant gases) and the electrolyte concentration. 5) To use the models in order to predict the relative effect of the physical phenomena that cause performance losses in a phosphoric acid hydrocarbon fuel cell and a phosphoric acid fuel cell cathode electrode. These phenomena include reactant gas diffusion in gas-filled electrode pores, dissolved reactant gas diffusion in liquid-filled electrode pores, ionic conduction in the electrolyte and the surface reactions (propane oxidation

and oxygen reaction) on the catalyst. The importance of this task is that it provides insight into which phenomena are more important thus leading to directions in which possible improvements of fuel cell performance can be achieved.

1.7 Review of direct hydrocarbon fuel cell literature – major findings

As mentioned before, the present work is the first simulation study of a direct hydrocarbon fuel cell. The literature on direct hydrocarbon fuel cells is largely based on experimental studies but very little work has been done recently. Most of the studies were performed during the 1960's and much of the work on the direct hydrocarbon fuel cell with aqueous electrolytes was reviewed by Liebhafksy and Cairns (1968), by Bockris and Srinivasan (1969) and by Cairns (1971).

Adsorption of the hydrocarbon on the surface is the required first-step in order for oxidation to occur. Detailed study of the adsorption behaviour of hydrocarbons on the catalyst metal is required because this process is not always facile. The adsorption process is potential-dependent and the fractional coverage versus potential curve usually follows a parabolic path (Bockris, 1969).

Cairns (1971) discussed experimental studies on the kinetics and mechanism of adsorption and electrochemical oxidation of hydrocarbons on platinum catalyst. On the basis of these studies it was concluded that alkanes adsorb dissociatively (losing H) on the surface and react readily with water to form single-carbon partially oxygenated (Pt-CHO) species, which is then oxidised to CO_2. This author suggested that, for steady-state oxidation, this last step is most possibly the rate-determining step. The adsorbed alkane species can also form carbonaceous deposits which may or may not be oxidised, depending on the electrical potential. A general reaction scheme was proposed, from which it was concluded that, at any time, several different types of species are adsorbed on the surface. The rates of adsorption, desorption and electrochemical oxidation of the various species were described by kinetic expressions. The resulting overall expression for the current density versus potential relationship had the form of the Tafel equation which will be introduced in Chapter 2. However, these kinetic expressions cannot be used to obtain quantitative results because the information in the literature is insufficient to determine the various rate constants that are required. This was clearly stated by the author. For this reason, in the present work, the Tafel equation was used to describe the kinetics, the kinetic parameters for which (exchange current density and Tafel slope) were obtained from existing experimental data.

In the same work by Cairns (1971), experimental research that had been performed until that time on the performance of direct hydrocarbon fuel cells was summarized. It was noted that the overall rate of hydrocarbon oxidation in acid electrolyte increases with temperature with an activation energy of 14-20 kcal/mole, depending on the electrolyte. The maximum permissible temperature of operation is, in most cases, determined by the boiling point of the electrolyte. The advantage of using phosphoric acid, as compared to other acids, is that in its highly concentrated form, it does not boil until the temperature rises to approximately 200°C.

In the same work, it was noted that pressurized operation of the hydrocarbon fuel cells had not been considered and that there had been no experimental work on the effect of hydrocarbon partial pressure. It was stated that, for alkanes, the reaction rate is expected to increase proportionally to the hydrocarbon partial pressure. For this reason, the effect of pressure was determined using the present model. As evidenced from the fact that state-of-the-art hydrogen fuel cells often operate at higher than atmospheric pressures (Appleby and Foulkes, 1989), the technological problems and complexities associated with pressurized operation have been resolved.

Another section in the work by Cairns (1971) was devoted to the significance of increasing the specific activity of platinum in the electrodes, because platinum was the only catalyst that showed significant activity towards hydrocarbon oxidation. The author noted that there exist two alternatives in the search for achieving this goal; research can be oriented either towards higher surface-area platinum blacks or towards supporting high surface-area platinum on corrosion-resistant, electronically conducting materials such as high surface-area graphite or carbon blacks. It should be noted that, subsequent to Cairn's work, very significant progress has been achieved and electrodes having platinum well dispersed on large surface-area carbons are now available. These advances came as a consequence of research for the hydrogen fuel cell and not the hydrocarbon fuel cell. Another objective of the present research is to simulate the performance of these modern electrodes in hydrocarbon cells.

Liebhafsky and Cairns (1968) presented a thermodynamic treatment of the C-H-O system for the purpose of calculating equilibrium compositions and phase boundaries. As mentioned by the authors, the calculated triangular phase diagrams are useful in understanding the conditions at which carbon deposition can be avoided. However, one of the conclusions is that the complexity

of the hydrocarbon anode makes the predictions drawn from equilibrium diagrams uncertain. The most important limitation of the analysis is that an operating fuel cell is not at equilibrium and only at steady-state for short periods. Another reason for the limited usefulness of equilibrium diagrams is that they tell nothing about the rate of the various processes happening in the fuel cell anode. The rest of the work is similar to that of Cairns, described previously. It discusses the major findings regarding the hydrocarbon adsorption and oxidation reaction mechanisms, the status of the hydrocarbon fuel cell at that time, the effects of different electrolytes and the issues associated with the use of platinum catalysts.

Bockris and Srinivasan (1969) devoted a chapter of their book to the electrochemical combustion of organic substances. They presented a more comprehensive account of the general criteria used to compare different fuels for fuel cells and the economic considerations for their use. In comparing the relative costs of using organic fuels directly in a fuel cell, they concluded that the projected cost per kWh associated with using propane was much less than that for any other hydrocarbon. The authors also discussed the direct versus indirect use of hydrocarbons in fuel cells, and compared efficiencies and costs of the various methods of generating electricity using hydrocarbons. The rest of the work by Bockris and Srinivasan (1969) discussed issues concerning the solubility of hydrocarbons in liquid electrolytes and the mechanism of adsorption and oxidation of hydrocarbons on metals. The discussion extended over a variety of fuels, including saturated and unsaturated hydrocarbons. The complexity of the reaction is apparent from the 15 possible reaction schemes that were proposed for the oxidation of propane. Some reported experimentally derived kinetic parameters were also useful in the present work (including the Tafel slope and reaction order with respect to propane partial pressure). All three reviews, discussed so far, summarize a very large amount of research and provide comprehensive lists of original references.

In the past thirty years, very little research on direct hydrocarbon fuel cells has appeared in the literature because the results of previously mentioned experiments were not very promising. However, the following work should be noted. Savadogo and Rodriguez (2001) presented the first experimental data on a low-temperature direct propane fuel cell utilizing membrane electrolytes. The operating temperature for these electrodes was in the neighbourhood of 100°C, which is considerably lower than the normal operating temperature of a PAFC (~200°C). Polarization curves for performance of different membrane types and different anode catalysts (Pt, Pt/CrO_3 and Pt/Ru) were reported. The $Pt\text{-}CrO_3$ electrocatalyst exhibited better performance

than the rest. A maximum power density of 46 mW /cm^2 was achieved. The authors stressed the need for optimization of cell components in order to achieve better performance.

In another work by Hahn and Melendres (2001), the mechanism of anodic oxidation of methane at noble metal electrodes at room temperature was studied using spectroscopic techniques. The results were in agreement with previous indications that methane adsorbs dissociatively on the Pt surface and that a C1 oxygenated species (Pt-CHO) is subsequently formed. Although additional studies are still needed, this work provided a better understanding of the mechanism of oxidation of hydrocarbons on platinum.

1.8 Review of literature related to phosphoric acid fuel cell cathode modeling

Several mathematical models for the PAFC oxygen cathode have been described in the literature. Similar concepts have been used to describe the performance of other electrodes, such as the hydrogen phosphoric acid fuel cell anode. The model that was developed in this work is described in detail in Chapter 2 and is essentially a modification of other models that have appeared in the literature. Furthermore, the same concepts were used to describe the performance of the propane anode electrode. In this section, an overview of existing models for the PAFC cathode is provided.

Homogeneous models of electrodes are conceptually simple. Vogel *et al* (1972) considered the electrode to be a planar sheet structure in which the electrolyte and catalyst were distributed homogeneously. Iliev *et al* (1975) proposed that the catalytic zone of the electrode planar sheet has two components; a zone of cylinders perpendicular to the edge of the electrode that is composed of a supposed homogeneous mixture of catalyst and electrolyte, and a wet-proofed non-catalytic zone surrounding the cylinders that is used to distribute the reactant gas. More recently, Maja *et al* (2001) extended Vogel's approach and included both oxygen diffusion in the gas phase and ohmic drop in the liquid phase.

Non-homogeneous models of the catalyst layer structure, which are more realistic, have progressively become more comprehensive. Early models (Newman and Tobias, 1962) considered the main location of the electrochemical reaction to be a three-phase interface of contact between the solid electrode, the electrolyte and the gaseous reactant. Another electrode

modeling concept, the simple pore model, in which unimodal cylindrical pores are flooded with electrolyte, was described by Brown and Rockett (1966) and by Srinivasan *et al* (1967). In another model using porous electrode theory, described by Newman and Tiedemann (1975), the reactant gas diffuses through gas-filled pores, dissolves in the electrolyte at the gas-electrolyte interface, and then the dissolved gas diffuses in the liquid phase to catalytic sites on the solid electrode. According to the thin-film model, described by Will (1963), unimodal cylindrical pores are largely gas-filled and covered with a thin electrolyte film on the pore walls. Electrodes with bimodal pore sizes have been modeled in two ways; (i) with all pores flooded with electrolyte, regardless of their dimensions (Austin and Lerner, 1964) and (ii) with only the small pores filled with electrolyte and the larger pores filled with gas (Burshtein *et al*, 1964, Grens, 1966). The thin-film model and the simple-pore model were compared by Austin *et al* (1965). They preferred the thin film model because its prediction of the limiting current being proportional to the square-root of the gas pressure was consistent with experimental observations.

The flooded agglomerate model of the catalyst layer, proposed by Giner and Hunter (1969), assumes a more complex electrode geometry than the above cylindrical pore models. In this model, porous catalyst particles are bonded together with poly-tetra-fluoro-ethylene (PTFE) particles to form agglomerates. The catalyst particles are electrically conductive and contain small pores that are flooded with electrolyte. The PTFE particles cause the spaces between the agglomerates to be hydrophobic, thereby creating gas channels in the form of larger pores. The reactant gas is assumed to diffuse through the hydrophobic larger pores, dissolves in the electrolyte contained in the small pores in the agglomerates and diffuses through it towards the catalytic sites on the surface of the catalyst particles.

The flooded agglomerate model has been used by several researchers to model phosphoric acid fuel cell cathodes. Some of the models can be solved analytically. Cutlip (1975) included the following processes in the electrode: (i) the diffusion of oxygen in the gas-filled pores (ii) the diffusion of dissolved oxygen across a thin film of electrolyte on the exterior of the agglomerates (iii) the combined diffusion and reaction of the dissolved oxygen in electrolyte-filled agglomerate pores. Maggio (1999) used a similar model and found that it compared favourably with experimental data (Kunz and Gruver, 1975) that was not available when Cutlip's work was performed. It successfully predicted the effects of oxygen partial pressure, thickness of the catalyst layer, platinum loading in the catalyst layer and percent of acid-occupied pore volume in the catalyst layer.

The more complex models require numerical solutions. Iczkowski and Cutlip (1980) developed a comprehensive model that included: (a) Stefan-Maxwell molecular diffusion in the gas diffusion layer, (b) a combination of Stefan-Maxwell diffusion and Knudsen diffusion in the larger gas-filled pores of the agglomerate in the catalyst layer, (c) equilibrium between the oxygen partial pressure in the larger agglomerate pores and the dissolved oxygen in the outermost liquid film surrounding the agglomerates, (d) diffusion of dissolved oxygen according to Fick's law through the electrolyte contained within the small agglomerate pores, (e) reaction at catalytic sites on the pore walls, (f) hydrogen ion migration according to Ohm's law through the electrolyte and (g) electron conduction through the catalyst layer according to Ohm's law.

Bjornbom (1987) developed a simpler model that did not include (a), (f) or (g). Only two parameters were adjusted to match the results of the model to experimental data. Yang *et al* (1989) modified the analytical model of Cutlip (1975) to include multi-component gas transport in the gas-diffusion layer as well as in the catalyst layer. In a subsequent paper (Yang *et al*, 1990)), they developed a model that combined the work of Iczkowski and Cutlip (1980) with an optimization procedure that required six parameters to be obtained from experimental data. Perry *et al* (1998) modified the model of Iczkowski and Cutlip (1980) to include both migration and diffusion of ions in solution. Their model did not include either (a) or (b). Their model indicated that the experimental data obtained by Maoka (1988) exhibited double Tafel slope caused by ionic mass transport, whereas Maoka had attributed the phenomenon to gas transport limitations. Yang (2000) developed a model that did not consider the effect of gas-transport in the electrode but did describe ionic conduction. The model explained changes in performance that were caused by changes in PTFE content. Very recently, Choudhury *et al* (2002) developed a two-dimensional model of a phosphoric acid fuel cell. Essentially, it was an extension of the approach of Perry *et al* (1998) from one to two dimensions.

CHAPTER 2: MATHEMATICAL MODEL DEVELOPMENT

2.1 The structure of the catalyst layer: description and model assumptions

The most important attributes of the physical structure of the catalyst layer of a phosphoric acid fuel cell have been described by various researchers (Giordano et al, 1991, Giner and Hunter, 1969, Appleby and Foulkes, 1989, Hirschenhofer *et al*, 1998). The catalyst layer of modern gas-diffusion electrodes used in phosphoric acid fuel cells is a very thin structure painted or pressed onto one side of the carbon paper or carbon cloth that serves as the gas diffuser. In the case of platinum electrodes, the electrocatalyst in the catalyst layer is dispersed in the pores of a carbon support. The carbon support particles are bonded together by particles of polytetrafluoroethylene (PTFE or Teflon). The solid structure of the catalyst layer contains three different solids: platinum, carbon and PTFE. PTFE is used because it is hydrophobic, so that a fraction of the pores in the catalyst layer is available for the distribution of the reactant gases throughout the layer and the removal of gaseous species produced by the reaction. The catalyst layer contains interior pores formed within the carbon structure and larger pores that are formed between the spaces at the exterior of the carbon agglomerates and between the PTFE particles. The interior pores are more easily wetted by the electrolyte by capillary forces. Some authors (Giordano *et al*, 1991) use the terms micropores and macropores to differentiate between the smaller (interior to the agglomerates) and larger (exterior to the agglomerates) pores in the catalyst layer of a PTFE-bonded fuel cell electrode. Giordano *et al* (1991) report a minimum of 0.4μm in the bimodal pore-size distribution of the electrocatalyst layer, obtained by porosimetric techniques.

The carbon particles within the catalyst layer stick together to form larger aggregates or agglomerates. These agglomerates are variable in size and shape within the electrode's catalyst layer. However, in order to describe the phenomena in the catalyst layer mathematically, an ordered physical structure can be assumed. In this model, the agglomerates are represented by spheres of equal radii. The agglomerates are assumed to contain all of the carbon particles present in the electrode and, consequently, all of the interior pores and dispersed platinum in the electrode. In the model, an agglomerate can be either completely filled with electrolyte or else dry. The existence of dry agglomerates is presumably because of their close proximity to particles of PTFE. Agglomerates that are not filled with electrolyte are not utilized because platinum particles that are not in contact with the electrolyte do not participate in the electrochemical reaction. These assumptions were also made by Giordano *et al* (1991). In the present model, the

agglomerates that are filled with electrolyte are assumed to be surrounded by a very thin liquid film. The space in the catalyst layer that is between the liquid film is assumed to be filled with the Teflon particles and the gas-filled macropores.

The assumed physical structure of the catalyst layer is shown in **Figure 2.1**. The platinum crystallites, dispersed on the carbon support, are illustrated by black dots and the brown-colored grains represent the agglomerated carbon particles. It should be emphasized that the assumed physical structure represents the true physical structure of the catalyst layer only in an approximate way but is capable of accounting for the most important of the physical phenomena that take place in it: the diffusion of gases in gas-filled pores, the dissolution of gases in the gas-electrolyte interphases, the diffusion of gases through thin liquid films, the diffusion of gases through micropores and simultaneous electrochemical reaction on the surface of the dispersed catalyst.

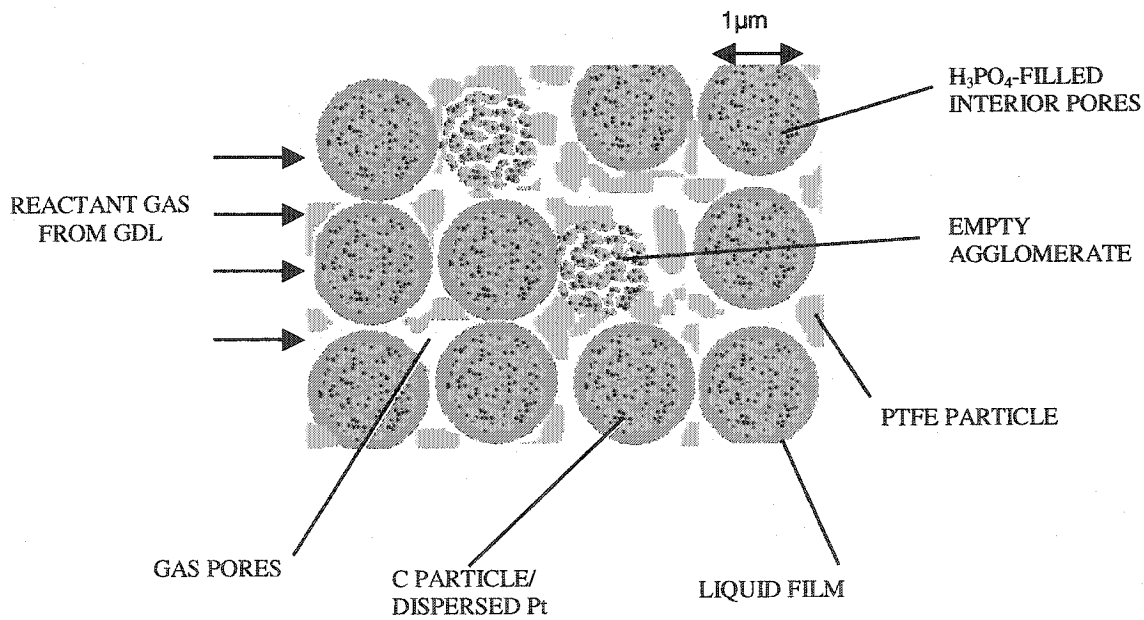

Figure 2.1: Modeled physical structure of the catalyst layer

2.2 Estimation of some model-specific catalyst layer properties

The complete characterization of the assumed catalyst layer structure requires the estimation of several properties, including the volume fractions of the solids, gas-filled pores and liquid electrolyte present, the number density of agglomerates and thickness of the surrounding liquid film as well as the fraction of agglomerates that are filled with electrolyte and therefore utilised in the catalyst layer. These properties were estimated and used in conjunction with reaction-rate equations to describe the performance of each electrode. The estimation of these properties is based on the following set of input parameters that are known or can be experimentally determined for a given electrode (all symbols used in this thesis are explained in the Nomenclature section):

L: The thickness of the catalyst layer (cm)

W_{Pt}: Weight fraction of platinum in catalyst (= mass of Pt / mass of (Pt+C))

M_{Pt}: Platinum loading per unit electrode surface area (g Pt / cm^2 electrode face surface area)

F_A: Fraction of acid occupation (= volume of liquid in pores / pore volume of catalyst layer)

W_T: Weight fraction of Teflon in catalyst layer (= mass of PTFE / mass of (Pt+C+PTFE))

f: The fraction of total pore volume that is interior pores in catalyst layer

S: The surface area per unit mass of platinum (cm^2 Pt / g Pt)

The term fraction (or percentage) of acid occupation (F_A) is consistent with usual terminology in the fuel cell literature. The platinum loading is referred to unit area of the electrode's face surface, in conjunction with usual fuel cell terminology. This means that the total amount of catalyst in the catalyst layer per unit electrode catalyst layer volume is given by the M_{Pt}/L. For a particular electrode, the fraction of total pore volume that is interior to the agglomerates f, and the fraction of pores that are wetted by electrolyte F_A, can be independently measured by experimental methods (Giordano *et al*, 1991). These parameters are dependent on the weight fractions of the solids (platinum, PTFE and carbon) in the catalyst layer, and are also dependent on the method and particular conditions (for example, sintering temperature) of preparation of the electrode (Giordano et al, 1991). In simulating the characteristics of the electrodes, consistent values should be used for the above parameters. From porosimetric data reported by Giordano *et al* (1991), for four different electrodes of $W_T = 0.40$ and $W_{Pt} = 0.10$ sintered at 340°C, the measured values for f were between 0.60 and 0.65, and the measured values for F_A were between 0.35 and 0.40.

Estimation of the volume fraction of the solids in the catalyst layer requires knowledge of the true density of platinum, carbon and PTFE. The following values were used by Giordano *et al* (1991):

ρ_{Pt}: The density of solid platinum = 21.4 g/cm^3

ρ_C: The density of solid carbon = 2 g/cm^3

ρ_T: The density of solid PTFE = 2.2 g/cm^3

The radii of the agglomerates can not be determined experimentally with a high degree of confidence. Furthermore, it is apparent that the agglomerates' size will be variable through the thickness of a given electrode and can be affected by many factors such as the Teflon content of the electrode and electrode ageing, because the agglomeration process can continue indefinitely during fuel cell operation for long periods of time. For these reasons, the agglomerate's radius in some agglomerate models that appear in the literature for the oxygen cathode is taken in such a way as to fit the experimental data or as an estimate obtained from micrographs of a specific electrode. The order of magnitude value for the agglomerate is taken to be 1μm (Fuller *et al*, 1995, Choudhury *et al*, 2002).

Another assumption that is made in this model is that the percentage of utilised agglomerates is linearly related to the percentage of acid occupation. At a certain F_A, denoted as $F_{A,MAX}$, all of the agglomerates are utilised. The percentage of micropores being filled with electrolyte is equal to the agglomerates' utilization because all micropores are within agglomerates. Justification for this assumption is given by Giordano *et al* (1991), where it is also shown that $F_{A,MAX}$ is approximately equal to 0.7. The agglomerate's radius R_A and the value of $F_{A,MAX}$ are used as specified values in this model. The resulting set of input parameters is sufficient to estimate all other relevant variables required for the assumed structure of the catalyst layer, including the characteristic thickness of the liquid film surrounding the agglomerate. The following set of equations was derived from mass and volume balances in the catalyst layer. The various symbols are explained in the nomenclature section. A similar analysis, based on volume and mass balances, is presented by Giordano *et al* (1991), who, however, neglected the presence of a liquid film. A similar analysis to the one given here was presented by Yang (2000), who considered the electrocatalyst utilization as an input parameter in the model. However, the utilization of the catalyst is a variable that cannot be measured. The assumptions made above do not require the value of catalyst utilization to be prescribed in advance.

The volume fraction of platinum in the catalyst layer is given by:

$$V_{Pt} = \frac{M_{Pt}}{L \rho_{Pt}} \tag{2.1}$$

The mass of carbon per unit electrode area (M_C) can be calculated by:

$$W_{Pt} = \frac{M_{Pt}}{M_C + M_{Pt}}$$

By rearranging:

$$M_C = \frac{M_{Pt}(1 - W_{Pt})}{W_{Pt}} \tag{2.2}$$

The volume fraction of carbon in the catalyst layer is given by:

$$V_C = \frac{M_C}{L \rho_C} \tag{2.3}$$

The mass fraction of PTFE per unit electrode area (M_T) can by calculated by:

$$W_T = \frac{M_T}{M_T + M_C + M_{Pt}}$$

By rearranging:

$$M_T = \frac{W_T(M_{Pt} + M_C)}{(1 - W_T)} \tag{2.4}$$

The volume fraction of PTFE in the catalyst layer is given by:

$$V_T = \frac{M_T}{L \rho_T} \tag{2.5}$$

The volume fraction of solid in the catalyst layer is given by:

$$V_S = V_{Pt} + V_C + V_T \tag{2.6}$$

The volume fraction of pores in the catalyst layer is given by:

$$V_P = 1 - V_S \tag{2.7}$$

The volume fraction of liquid in the catalyst layer (V_L) can be calculated by:

$$F_A = \frac{V_L}{V_P}$$

$$\Rightarrow V_L = F_A V_P$$

Therefore:

$$V_L = F_A (1 - V_S) \tag{2.8}$$

The volume fraction of gas in the catalyst layer:

$$V_G = 1 - V_S - V_L$$

$$V_G = (1 - F_A)(1 - V_S) \tag{2.9}$$

The volume fraction of agglomerates in the catalyst layer is given by:

$$V_A = V_{Pt} + V_C + V_m = V_{Pt} + V_C + fV_P$$

Thus:

$$V_A = (V_{Pt} + V_C) + f(1 - V_S) \tag{2.10}$$

The agglomerates' porosity is given by:

$$V_{mA} = \frac{V_m}{V_A} = \frac{f V_P}{V_A}$$

$$\Rightarrow V_{mA} = \frac{f(1-V_S)}{V_A} \tag{2.11}$$

The agglomerates' density (number of agglomerates per unit volume in the catalyst layer = volume fraction of agglomerates / volume occupied by one agglomerate) is given by:

$$N_A = \frac{V_A}{\left(4/3\right)\pi R_A^{\,3}} \tag{2.12}$$

The fraction of agglomerates that is utilised (= fraction of micropores' volume that is utilised) is given by:

$$\begin{aligned} u &= \frac{F_A}{F_{A,MAX}} \quad \text{if} \quad F_A < F_{A,MAX} \\ u &= 1 \quad \text{if} \quad F_A > F_{A,MAX} \end{aligned} \tag{2.13}$$

Equation 2.13 suggests that if the volume of electrolyte in the catalyst layer is greater than F_A, then all agglomerates are utilised and the rest of the electrolyte increases the thickness of the liquid film. Based on the assumed physical structure of the catalyst layer, the non-utilization of a fraction of the catalyst is attributed to the fact that some of the carbon-platinum agglomerates are dry. The situation of non-utilization of part of the catalyst because it is not in contact with electrolyte has not been well described in the literature. However, Giordano *et al* (1991) have verified experimentally the linear correlation between catalyst utilization and volume fraction of micropores wetted by electrolyte.

The utilised agglomerates density is given by:

$$N_{uA} = uN_A \tag{2.14}$$

The utilised agglomerates' volume-fraction in the catalyst layer is given by:

$$V_{uA} = uV_A \tag{2.15}$$

The volume-fraction of liquid film in the catalyst layer (V_F) can be found from the following volume balance:

(Volume-fraction of liquid films) = (Total liquid volume-fraction) – (Volume-fraction of liquid that is within agglomerates). Therefore:

$$V_F = V_L - (V_{uA})(V_{mA}) = F_A(1-V_S) - (u\,V_A)\left(\frac{f(1-V_S)}{V_A}\right)$$

$$\Rightarrow V_F = (1-V_S)(F_A - uf) \tag{2.16}$$

The thickness of the liquid film can be found from the following volume balance:

(Volume-fraction of liquid films) = (volume-fraction of utilised agglomerates) · (volume of film/volume of agglomerate)

$$V_F = (V_{uA})\left(\frac{(4/3)\pi\left((R_A + L_F)^3 - R_A{}^3\right)}{(4/3)\pi R_A{}^3}\right) = (V_{uA})\left(\left(\frac{R_A + L_F}{R_A}\right)^3 - 1\right)$$

From which:

$$L_F = R_A\left(\left(\frac{V_F}{V_{uA}} + 1\right)^{1/3} - 1\right) \tag{2.17}$$

The total surface area of platinum per cm^2 electrode face area in catalyst layer is given by:

$$S_T = (M_{Pt})(S) \tag{2.18}$$

The surface area of platinum per unit volume in the catalyst layer is given by:

$$S_V = \frac{(M_{Pt})(S)}{L} \tag{2.19}$$

The surface area of platinum per unit volume of agglomerate is given by:

$$S_A = \frac{(M_{Pt})(S)}{(L)(V_A)} \tag{2.20}$$

2.3 Derivation of reaction-rate equations

In this section, the equations that are used to describe the volumetric reaction rate in the catalyst layer are derived. Because this analysis is applicable to both the anode and cathode electrodes, the general case is considered and the derived equations are then applied to the electrode under consideration.

The analysis proceeds by considering reaction and diffusion equations inside the agglomerate to derive the reaction rate per agglomerate as a function of the reactant gas partial pressure (or molar concentration) in the gas pores surrounding the agglomerate's liquid film. The reactant gas partial pressure in the gas pores in the electrode is variable across the catalyst layer thickness and the coupling between gas-phase diffusion and simultaneous reaction will be considered in the next section. The analysis is based on considering a double distribution of reactant gas in the catalyst layer: in the *axial* direction across the electrode's thickness (z-direction) in the gas pores, and in the *radial* direction inside the spherical agglomerates. The latter one is the subject of this section.

Under the assumption that the thin liquid film surrounding the agglomerate is a spherical shell that contains only liquid, diffusion of the reactant gas in the liquid film is characterized by the diffusion coefficient of the dissolved gas in the electrolyte. However, diffusion of the gas inside the agglomerate is characterized by an effective diffusion coefficient that takes into account the porosity of the agglomerate and the tortuosity of the micropores within it. The natural coordinate system is spherical. The following boundary conditions were considered in order to solve the equations: at the center of the spherical agglomerate, the reactant gas flux must be zero by symmetry. At the external surface of the liquid film, the dissolved gas is considered to be in equilibrium with the surrounding gas-filled pores, so that its concentration can be given by Henry's law. Because the analysis requires separate equations to be written for the agglomerate and the liquid film surrounding it, the resulting concentration distributions should result in a common concentration at the interphase between the liquid film and the agglomerate. **Figure 2.2**

presents the agglomerate, liquid film, coordinate direction and the location of boundary conditions. The symbols in the equations are given in the Nomenclature section.

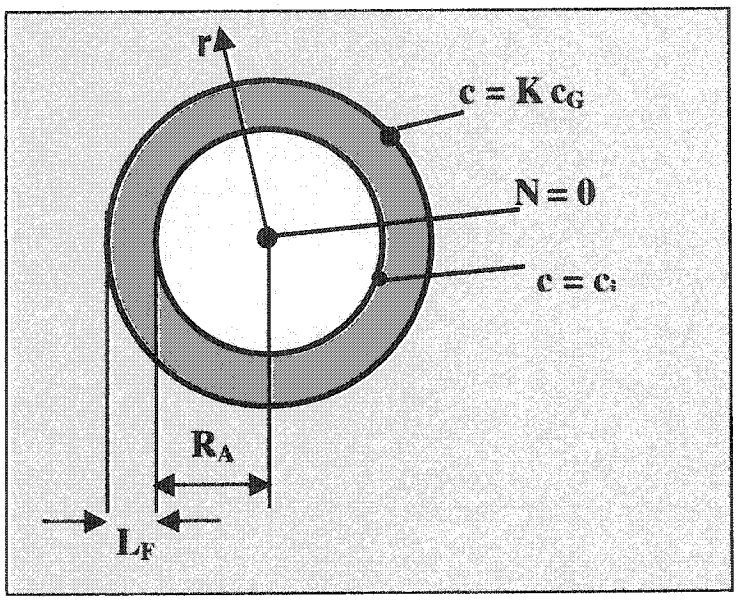

Figure 2.2: Schematic representation of agglomerate and liquid film showing the boundary conditions

The reaction-diffusion equation for the catalyst layer is derived by a mass balance for a differential spherical shell at position r in the agglomerate. The molar flux of reactant gas in the radial direction in the agglomerate is given by Fick's law. If the positive direction for the molar flux of reactant gas is defined as that in the negative radial direction in the agglomerate, then the mass balance can be written as:

$$N|_{(r+dr)}[4\pi(r+dr)^2] = N|_r\,(4\pi r^2) + (R_{VA})[(4/3)\pi((r+dr)^3 - r^3)]$$

$$\Rightarrow D_e\left(\left.\frac{dc}{dr}\right|_{(r+dr)}\right)(r+dr)^2 - D_e\left(\left.\frac{dc}{dr}\right|_r\right)(r^2) = \left(\frac{R_{VA}}{3}\right)\left((r+dr)^3 - r^3\right)$$

$$\Rightarrow D_e \frac{d}{dr}\left(r^2 \frac{dc}{dr}\right) = (R_{VA}) r^2$$

$$\Rightarrow \frac{1}{r^2} \frac{d}{dr}\left(r^2 \frac{dc}{dr}\right) = \frac{R_{VA}}{D_e} \tag{2.21}$$

The volumetric reaction rate inside the agglomerate is given by applying the Butler-Volmer equation. The current density per unit surface area of platinum is given by (Bockris, 1969, Newman, 1973):

$$i = -i_o\left[\exp\left(\frac{a_a F\eta}{RT}\right) - \exp\left(-\frac{a_c F\eta}{RT}\right)\right] \tag{2.22}$$

where:

$$\eta = \Phi_S - \Phi_E - E_{EQ} \tag{2.23}$$

The exchange current density, i_o, is the current transferred per unit surface area of platinum for the forward or reverse direction of the reaction at equilibrium and it is customary to refer to the case when the electrolyte is saturated with the gas. The overpotential, η, represents the deviation of the electrical potential difference across the metal-solution interface from its equilibrium value. At thermodynamic equilibrium $\eta = 0$ and no current is transferred across the interface. Equivalently, the rate of charge transfer for the forward direction of the electrochemical reaction is equal to that for the reverse direction of the reaction). When a potential difference across the metal-solution interface is established, $\eta \neq 0$, and a charge transfer reaction proceeds at a finite rate. When the overpotential is sufficiently high (greater than ~100 mv), the second exponential term of the Butler-Volmer equation (2.22),which represents the contribution of the reverse direction of the reaction to the net reaction rate, can be neglected, because its magnitude becomes negligible compared to the first exponential term. In this case, the equation reduces to the Tafel equation, which one of the most fundamental equations in electrochemistry:

$$i = -i_o\left[\exp\left(\frac{aF\eta}{RT}\right)\right] \tag{2.22b}$$

The exchange current-density, i_o, and the transfer coefficient, a, are also called the Tafel parameters for the reaction. The Tafel slope is the slope of the η versus log i curve. The Tafel parameters determine the kinetics of an electrochemical reaction, sufficiently away from equilibrium.

The oxygen reduction reaction is regarded as first-order with respect to dissolved oxygen concentration (Appleby, 1974). The propane oxidation reaction is also regarded as first-order with respect to dissolved propane concentration (Bockris and Srinivasan, 1969). If the solubility of the gas in the electrolyte is c*, then for a first-order reaction, such as oxygen reduction, the current-density for dissolved gas concentrations different from the saturation solubility value is given as:

$$i = -i_o\left(\frac{c}{c^*}\right)\left[\exp\left(\frac{a_a F\eta}{RT}\right) - \exp\left(-\frac{a_c F\eta}{RT}\right)\right] \tag{2.24a}$$

For the propane oxidation reaction, the reaction rate was also assumed to be first order to the activity of water in solution because water is a reactant in the anode. For the propane oxidation reaction, equation 2.24 then takes the form:

$$i = -i_o\left(\frac{c}{c^*}\right)(a_W)\left[\exp\left(\frac{a_a F\eta}{RT}\right) - \exp\left(-\frac{a_c F\eta}{RT}\right)\right] \tag{2.24b}$$

In what follows, equation 2.24a will be used and the water activity factor will be added in the final expression for the propane oxidation reaction.

The exchange current-density is taken to vary with temperature according to an Arrhenius-type expression (Damjanovic and Sepa, 1989, Bockris, 1969):

$$i_o = i_o^* \exp\left[\frac{\Delta G^{\neq}}{R}\left(\frac{1}{T^*} - \frac{1}{T}\right)\right] \tag{2.25}$$

where i_o^* is the exchange current-density at a reference temperature T^* for the oxygen reduction or the propane oxidation reaction on platinum in phosphoric acid, and $\Delta G^{\neq}$ denotes the activation energy for the exchange current.

The current transferred across the metal-solution interface per unit volume inside the agglomerate is given by the current density multiplied by the surface area of platinum per unit volume in the agglomerate S_A.

$$i_{VA} = -\left(\frac{S_A i_o c}{c^*}\right)\left[\exp\left(\frac{a_a F\eta}{RT}\right) - \exp\left(-\frac{a_c F\eta}{RT}\right)\right] \tag{2.26}$$

Subsequently, Faraday's law can be used to relate the current to the reaction rate (in moles of reactant consumed per unit volume per unit time) inside the agglomerate:

$$R_{VA} = -\left(\frac{S_A i_o c}{nFc^*}\right)\left[\exp\left(\frac{a_a F\eta}{RT}\right) - \exp\left(-\frac{a_c F\eta}{RT}\right)\right] \tag{2.27}$$

Equation 2.27 can be substituted into equation 2.21 to obtain the differential equation that describes the reactant gas concentration distribution inside the agglomerate:

$$\frac{1}{r^2}\frac{d}{dr}\left(r^2 \frac{dc}{dr}\right) = -\left(\frac{S_A i_o c}{nFc^* D_e}\right)\left[\exp\left(\frac{a_a F\eta}{RT}\right) - \exp\left(-\frac{a_c F\eta}{RT}\right)\right] \tag{2.28}$$

The above equation is subject to the boundary conditions:

$$\text{At } r = R_A,\ c = c_i$$
$$\text{At } r = 0,\ dc/dr = 0$$

Equation 2.28 subject to these boundary conditions can be solved analytically (proof is given in **Appendix A**). The solution is:

$$c = c_i \frac{R_A}{r}\frac{\sinh(\sqrt{\Psi}\, r)}{\sinh(\sqrt{\Psi} R_A)} \tag{2.29}$$

where:

$$\Psi = -\left(\frac{S_A i_o}{nFc^* D_e}\right)\left[\exp\left(\frac{a_a F\eta}{RT}\right) - \exp\left(-\frac{a_c F\eta}{RT}\right)\right] \tag{2.30}$$

The reaction rate per individual agglomerate can be given by the molar input of oxygen at the interface between the agglomerate and the liquid film, which is given by the flux multiplied by the spherical surface area at $r = R_A$:

$$R_{AG} = (N|_{r=R_A})(4\pi {R_A}^2)$$

$$= D_e c_i R_A \left\{ \frac{r\sqrt{\Phi}\cosh(\sqrt{\Psi}r) - \sinh(\sqrt{\Psi}r)}{r^2 \sinh(\sqrt{\Psi}R_A)} \right\}\Bigg|_{r=R_A} \times \left(4\pi {R_A}^2\right)$$

$$\Rightarrow R_{AG} = 4\pi D_e c_i R_A (\sqrt{\Psi}R_A \coth(\sqrt{\Psi}R_A) - 1) \qquad (2.31)$$

The last result was also given by Perry *et al* (1991).

The interfacial concentration, c_i, in equation 2.31 will be eliminated after consideration of gas diffusion through the liquid film. A mass balance for a differential control volume for spherical shell at position r in the liquid film is the starting point to obtain the concentration distribution through the film:

$$N|_{(r+dr)}[4\pi(r+dr)^2] = N|_r (4\pi r^2)$$

$$\Rightarrow D\left(\frac{dc}{dr}\Big|_{r+dr}\right)(r+dr)^2 = D\left(\frac{dc}{dr}\Big|_r\right)(r^2)$$

$$\Rightarrow \frac{d}{dr}\left(r^2 \frac{dc}{dr}\right) = 0$$

$$\Rightarrow r^2 \frac{dc}{dr} = C_1$$

$$\frac{dc}{dr} = \frac{C_1}{r^2} \Rightarrow \qquad (2.32)$$

$$\Rightarrow c = -\frac{C_1}{r} + C_2$$

where C_1 and C_2 are constants that can be evaluated by the boundary conditions (only C1 is useful):

$$\text{At } r = R_A,\ c = c_i$$

$$\text{At } r = R_A + L_f,\ c = Kc_G$$

Using the boundary conditions:

$$Kc_G - c_i = \frac{C_1}{R_A + L_F} + \frac{C_1}{R_A}$$

$$\Rightarrow C_1 = \frac{R_A(R_A + L_F)(Kc_G - c_i)}{L_F} \tag{2.33}$$

The reaction rate per agglomerate is equal to the input flux of reactant gas at the external surface of the liquid film multiplied by the surface area at $R_A + L_F$. The concentration gradient in the radial direction in the agglomerate is given by substituting equation 2.33 into equation 2.32:

$$\frac{dc}{dr} = \frac{R_A(R_A + L_F)(Kc_G - c_i)}{L_F r^2}$$

$$\Rightarrow N_{(R_A + L_F)} = D\left(\frac{dc}{dr}\Big|_{(R_A + L_F)}\right) = \frac{DR_A(R_A + L_F)(Kc_G - c_i)}{L_F(R_A + L_F)^2} = \frac{DR_A(Kc_G - c_i)}{L_F(R_A + L_F)}$$

$$\Rightarrow R_{AG} = (N_{(R_A + L_F)})(4\pi(R_A + L_F)^2)$$

$$\Rightarrow R_{AG} = \frac{4\pi DR_A(R_A + L_F)(Kc_G - c_i)}{L_F} \tag{2.34}$$

Elimination of the boundary concentration c_i can be achieved by equating the two independent expressions for the reaction rate, equations 2.31 and 2.34:

$$\frac{4\pi D R_A (R_A + L_F)(Kc_G - c_i)}{L_F} = 4\pi D_e c_i R_A (\sqrt{\Psi} R_A \coth(\sqrt{\Psi} R_A) - 1)$$

$$\Rightarrow D(R_A + L_F)Kc_G - D(R_A + L_F)c_i = L_F D_e c_i (\sqrt{\Psi} R_A \coth(\sqrt{\Psi} R_A) - 1)$$

$$\Rightarrow c_i = \frac{D(R_A + L_F)Kc_G}{D(R_A + L_F) + L_F D_e (\sqrt{\Psi} R_A \coth(\sqrt{\Psi} R_A) - 1)} \tag{2.35}$$

(As a check: As $L_f \rightarrow 0$, ci $\rightarrow Kc_G$, as expected)

Therefore the reaction rate per agglomerate is given by substituting equation 2.35 into equation 2.31:

$$R_{AG} = 4\pi D_e \frac{D(R_A + L_F)Kc_G}{D(R_A + L_F) + L_F D_e (\sqrt{\Psi} R_A \coth(\sqrt{\Psi} R_A) - 1)} R_A (\sqrt{\Psi} R_A \coth(\sqrt{\Psi} R_A) - 1)$$

$$\Rightarrow R_{AG} = \frac{4\pi D_e D(R_A + L_F)Kc_G R_A (\sqrt{\Psi} R_A \coth(\sqrt{\Psi} R_A) - 1)}{D(R_A + L_F) + L_F D_e (\sqrt{\Psi} R_A \coth(\sqrt{\Psi} R_A) - 1)}. \tag{2.36}$$

The above is the reaction rate per agglomerate. Therefore, for the reaction rate per unit volume in the catalyst layer, it has to be multiplied by the density of utilised agglomerates. Thus,

$$R_V = N_{uA} \frac{4\pi D_e D(R_A + L_F)Kc_G R_A (\sqrt{\Psi} R_A \coth(\sqrt{\Psi} R_A) - 1)}{D(R_A + L_F) + L_F D_e (\sqrt{\Psi} R_A \coth(\sqrt{\Psi} R_A) - 1)} \tag{2.37}$$

where, for the cathode:

$$\Psi = -\left(\frac{S_A i_o}{4Fc^* D_e}\right)\left[\exp\left(\frac{a_a F\eta}{RT}\right) - \exp\left(-\frac{a_c F\eta}{RT}\right)\right] \tag{2.38a}$$

and for the anode:

$$\Psi = -\left(\frac{S_A i_o a_W}{4Fc^* D_e}\right)\left[\exp\left(\frac{a_a F\eta}{RT}\right) - \exp\left(-\frac{a_c F\eta}{RT}\right)\right] \tag{2.38b}$$

Equations 2.37, 2.38a and 2.38b are the final expressions derived for the volumetric reaction rate in the catalyst layer as a function of the molar concentration of reactant gas in the gas-filled pores and the overpotential at a certain location in the catalyst layer. Both these quantities are variable through the catalyst layer and their variation is considered in the direction z in this model. The developed equations are different from those reported in the literature because other researchers (Cutlip, 1991) usually consider planar (and not spherical) diffusion for the liquid film because of its small thickness and the assumption is made that the effective diffusivities of the reactant in the liquid film and the agglomerate are the same. These assumptions were relaxed in the present model. Some researchers (Perry *et al*, 1998) do not consider the presence of the liquid film. In this case, the equations derived here agree with those given in the literature in the limit $L_F = 0$.

However, the reaction rate in fuel cells is expressed as the current-density delivered from the fuel cell per unit area of electrode face area. The reaction rate in equation 2.37 is expressed in moles of reactant consumed per unit volume per unit time. The conversion to the current produced (or transferred) per unit volume requires the use of Faraday's law. The current produced per unit electrode face area is obtained by integrating the current produced per unit volume across the thickness of the catalyst layer.

$$I = nF\int_{z_1}^{z_2} R_V\, dz \tag{2.39}$$

where z_1 and z_2 are z-coordinates of the catalyst layer-gas diffusion layer boundary and catalyst layer- electrolyte layer boundary, respectively.

2.4 Transport of gas-phase species

The flow of gases inside the porous gas-diffusion layer and the porous catalyst layer, in the z-direction, is considered to be due to molecular and Knudsen diffusion. Molecular diffusion is the transport mechanism in which the molecules of the gas exchange momentum by colliding with each other. In a porous medium, the molecules are also colliding with the walls of the pores, which gives rise to the Knudsen diffusion mechanism. If the mean free-path traveled by a molecule between two molecule-molecule collisions is much smaller than the mean-free path between two molecule-wall collisions, then molecular diffusion predominates. However, if the size of the pores is small, the frequency of molecule-pore wall collision can be quite high. Furthermore, at low pressures the frequency of molecular collisions will be low. Therefore, under certain circumstances (small pores, low pressure), Knudsen diffusion can contribute much to the total gas diffusion rate.

The gas-filled pores in the anode and cathode electrodes during fuel cell operation contain ternary gas systems. In the anode, the pores are filled with propane reactant gas, carbon dioxide produced by the reaction and water vapour. In the cathode, the exterior pores are filled with the air mixture consisting of oxygen and nitrogen, and water vapour. If pure oxygen is supplied to the cathode, there is no nitrogen and the diffusion equations are simplified. The water vapour present in the pores may be supplied to the electrode, if humidified reactants are used. However, even in the cases when the reactant gases are not humidified, there will be water vapour in the pores caused by evaporation of the liquid electrolyte. In this model, the water partial pressure in the gas-filled pores is assumed to be the equilibrium partial water vapour pressure of the electrolyte and depends on the temperature and the electrolyte concentration.

The equations that are used to describe multi-component gas diffusion in the gas phase are the Stefan-Maxwell equations (Geankoplis, 1972). These equations reduce to Fick's law of diffusion when a binary gas system is considered. In the case of multi-component gas diffusion, Fick's law is not used because the available diffusion coefficients refer to binary gas mixtures. By using the Stefan-Maxwell equations, we assume that there is no bulk motion by convection in the z-direction. However, there are two modes of diffusion in these layers: multi-component molecular diffusion and Knudsen diffusion. In the transition regime, the concentration gradients resulting from the two modes of diffusion are additive (Geankoplis, 1972, Rothfeld, 1963).The appropriate

formulation of the Stefan-Maxwell equations, which takes into account both of the above mechanisms, is also used by various researchers to describe gas diffusion in the electrodes (Cutlip *et al*, 1989, Iczkowski and Cutlip, 1980, Kulikovsky *et al*, 2000):

$$\frac{\overrightarrow{N_k}}{D^K_{k,e}} + \sum_{m,m\neq k} \frac{x_m\overrightarrow{N_k} - x_k\overrightarrow{N_m}}{D_{km,e}} = -c_T \frac{dx_k}{dz} \tag{2.40}$$

According to the Stefan – Maxwell equation in the form written here, the concentration gradient of a component k in the multi-component mixture is the superposition of a Knudsen diffusion term (the first term in equation 2.40) and a molecular diffusion term (the second term). The concentration gradient of any component in the system required for molecular diffusion depends on the molar fluxes of all other components. The binary diffusion coefficients used in this equation are the binary diffusion coefficients that are used in application of Fick's law for binary diffusion of gases. When this equation is applied to a porous medium, the Knudsen diffusion coefficients and binary diffusion coefficients require correction for the porosity (because only a fraction of the total volume is available for diffusion) and the tortuosity (increased diffusion path due to tortuous shape of the pores) of the medium. The subscript e is used to denote the effective value of the diffusion coefficients.

Equation 2.40 can be written in the following equivalent form (using $x_k = c_k / c_t$), where molar concentrations of the gases are used instead of mole fractions:

$$\frac{\overrightarrow{N_k}}{D^K_{k,e}} + \sum_{m,m\neq k} \frac{c_m\overrightarrow{N_k} - c_k\overrightarrow{N_m}}{c_T D_{km,e}} = -\frac{dc_k}{dz} \tag{2.41}$$

Equation 3.41 will be applied to the porous gas-diffusion layer and catalyst layer of the fuel cell. With a positive flux defined in the positive z-direction as in Figure 1.2, equation 2.41 can be written in scalar form instead of vectorial form:

$$\frac{N_k}{D^K_{k,e}} + \sum_{m,m\neq k} \frac{c_m N_k - c_k N_m}{c_T D_{km,e}} = -\frac{dc_k}{dz} \tag{2.42}$$

In this formulation, the vector fluxes that are pointing in the negative z-direction are negative scalar fluxes.

In applying equation 2.42 to the anode and cathode electrodes, some terms can be simplified. The concentration of water vapour in the pores has been assumed to be constant and equal to the equilibrium vapour pressure of the electrolyte. The molar flux of nitrogen in the cathode is zero because nitrogen is neither produced nor consumed by the electrochemical reaction. Similarly, the molar flux of water vapour in the anode electrode is zero because it has been assumed that the product water required to be removed from the cell for steady – state is removed from the cathode of the cell. Taking these into account, the concentration gradients for propane and carbon dioxide in the anode are given by:

$$-\frac{dc_P}{dz} = \frac{N_P}{D^K_{P,e}} + \frac{c_{CO2}N_P - c_P N_{CO2}}{c_T D_{P/CO2,e}} + \frac{c_W N_P}{c_T D_{P/W,e}} \tag{2.43}$$

$$-\frac{dc_{CO2}}{dz} = \frac{N_{CO2}}{D^K_{CO2,e}} + \frac{c_P N_{CO2} - c_{CO2} N_P}{c_T D_{P/CO2,e}} + \frac{c_W N_{CO2}}{c_T D_{CO2/W,e}} \tag{2.44}$$

where

$$c_T = c_P + c_{CO2} + c_W \tag{2.45}$$

The fluxes of propane and carbon dioxide in the gas phase are related by the reaction's stoichiometry:

$$N_{CO2} = -3N_P \tag{2.46}$$

Similarly, the concentration gradients for oxygen and nitrogen in the cathode are given by:

$$-\frac{dc_{O2}}{dz} = \frac{N_{O2}}{D^K_{O2,e}} + \frac{c_W N_{O2} - c_{O2} N_W}{c_T D_{O2/W,e}} + \frac{c_{N2} N_{O2}}{c_T D_{O2/N2,e}} \tag{2.47}$$

$$\frac{dc_{N2}}{dz} = \frac{c_{N2}N_{O2}}{c_T D_{O2/N2,e}} + \frac{c_{N2}N_W}{c_T D_{N2/W,e}} \tag{2.48}$$

where:

$$c_T = c_{O2} + c_{N2} + c_W \tag{2.49}$$

The oxygen and water vapour flux in the cathode are related by the reaction's stoichiometry:

$$N_W = -2N_{O2} \tag{2.50}$$

Because the effect of Knudsen diffusion depends on the pore radius, it is expected that Knudsen diffusion will not contribute much to the total diffusion in the gas-diffusion layers, where the pores are larger than in the catalyst layers. Cutlip *et al* (1991) report that for pores greater than $\sim 10^{-4}$cm diffusion would be completely molecular. Pores in the gas-diffusion layer are larger (Hirschenhofer, 1998). Nevertheless, this can be taken into account by the above equations by using different Knudsen diffusion coefficients for the catalyst and diffusion layers.

The molar fluxes of propane in the anode and of oxygen in the cathode of the fuel cell are related to their volumetric rates of consumption (reaction rates) by the following relations accounting for mass-balance between the reactant gas molar-flux and consumption rate:

$$\frac{dN_P}{dz} = -R_{V,AN} \tag{2.51}$$

$$\frac{dN_{O2}}{dz} = -R_{V,CAT} \tag{2.52}$$

The reaction-rate equation, diffusion equation and mass-balance equation in the catalyst layers are coupled. For example, in the anode, the propane concentration gradient is related to the propane flux by equation 2.43. The propane flux gradient is related to the reaction rate by equation 2.51. The reaction rate is related to the propane concentration by equation 2.37. Therefore these equations have to be solved simultaneously.

The rates of consumption of propane and oxygen in the gas-diffusion layers are zero (no reaction) and therefore, for the gas-diffusion layers, the reactant gas flux is constant:

$$\frac{dN_P}{dz} = 0 \tag{2.53}$$

$$\frac{dN_{O2}}{dz} = 0 \tag{2.54}$$

2.5 Ionic conduction

Electrical conduction of ions is considered the main mechanism of transfer of positive charge within the liquid electrolyte phase from the anode to the cathode of the cell. In the phosphoric acid electrolyte, the principal charge-carrying species is the proton. However, other ionic species, such as anions, also contribute to the electrical current in the electrolyte, determined by their transport numbers. In this model, the net ionic flux is only considered, referring to the moles of protons transferred per unit area perpendicular to the z-direction per unit time. Ionic conduction can be described by Ohm's law (Cutlip *et al*, 1991, Iczkowski and Cutlip, 1980), which states that the net ionic current density (N_+ (amp/cm^2)) is proportional to the electrical potential gradient in the electrolyte:

$$N_+ = -k_e \frac{d\Phi_E}{dz} \tag{2.54}$$

The proportionality constant is the effective specific conductivity in the relevant layer. Ohm's law is applicable to the layers of the fuel cells where there is electrolyte: the catalyst layers and the electrolyte compartment (layer) of the cell. The electrolyte layer is very porous and is completely filled with electrolyte. The effective specific conductivity can be considered to be the same as the specific conductivity of the electrolyte. However, in the catalyst layer, only a fraction of the pores are filled with liquid. Furthermore, the ions have to conduct through the tortuous path of the connected network of liquid-filled micropores. Thus, the specific conductivity of the electrolyte in the catalyst layers requires correction for the porosity and tortuosity of the layer.

The rate of production of protons in the anode and the rate of consumption of protons in the cathode are related to the reaction rate by the reaction stoichiometry.
Thus, in the anode, the reaction is:

$$C_3H_8 + 6H_2O \rightarrow 3CO_2 + 20H^+ + 20e^- \qquad \text{(Reaction 2)}$$

The volumetric rate of production of ionic charge (R_+) is related to the rate of propane consumption (reaction rate) by:

$$R_{+,AN} = 20\, FR_{V,AN} \qquad (2.55)$$

The ionic current-density is related to the rate of proton production by the mass balance equation:

$$\frac{dN_{+,AN}}{dz} = R_{+,AN} \qquad (2.56)$$

From the reaction stoichiometry for the cathode reaction,

$$5O_2 + 20H^+ + 20e^- \rightarrow 10H_2O \qquad \text{(Reaction 3)}$$

the rate of ionic charge consumed is related to the rate of oxygen consumption (reaction rate) by:

$$R_{+,CAT} = 4\, FR_{V,CAT} \qquad (2.57)$$

The ionic current-density is related to the rate of proton consumption by the mass balance equation:

$$\frac{dN_{+,CAT}}{dz} = -R_{+,CAT} \qquad (2.58)$$

In the electrolyte layer, there is no production or consumption of protons. The gradient of the net ionic current density must be zero:

$$\frac{dN_{+,CAT}}{dz} = 0 \qquad (2.59)$$

Moreover, the reaction rates in the anode and cathode catalyst layers depend on the distribution of electrical potential in the electrolyte-filled pores across the catalyst layer, because the latter has an effect on the local overpotential. Thus the equations describing the reaction rate and ionic conduction are coupled. The interconnection between the equations that describe gas diffusion, electrochemical reaction and ionic conduction will become apparent in **Chapter 3**.

CHAPTER 3: DESCRIPTION OF COMPUTATIONAL METHOD

In this chapter, a summary of the main model equations is first presented in order to pose the problem mathematically. The coupling between the variables of the differential equations is shown and the boundary conditions that have to be satisfied are listed. The solution procedure is outlined, and the technique used to predict the polarization curves of the cathode and the whole propane fuel cell are presented.

3.1 Summary of model equations

The equations that are relevant in the anode gas-diffusion layer are:

$$\frac{dN_P}{dz} = 0 \tag{3.1}$$

$$-\frac{dc_P}{dz} = \frac{N_P}{D^K_{P,e}} + \frac{c_{CO2}N_P - c_P N_{CO2}}{c_T D_{P/CO2,e}} + \frac{c_W N_P}{c_T D_{P/W,e}} \tag{3.2}$$

$$-\frac{dc_{CO2}}{dz} = \frac{N_{CO2}}{D^K_{CO2,e}} + \frac{c_P N_{CO2} - c_{CO2} N_P}{c_T D_{P/CO2,e}} + \frac{c_W N_{CO2}}{c_T D_{CO2/W,e}} \tag{3.3}$$

$$c_T = c_P + c_{CO2} + c_W \tag{3.4}$$

$$N_{CO2} = -3N_P \tag{3.5}$$

The equations that are relevant in the anode catalyst layer are:

$$\frac{dN_P}{dz} = -R_{V,AN} \tag{3.6}$$

$$-\frac{dc_P}{dz} = \frac{N_P}{D^K_{P,e}} + \frac{c_{CO2}N_P - c_P N_{CO2}}{c_T D_{P/CO2,e}} + \frac{c_W N_P}{c_T D_{P/W,e}} \tag{3.7}$$

$$-\frac{dc_{CO2}}{dz}=\frac{N_{CO2}}{D^{K}_{CO2,e}}+\frac{c_P N_{CO2}-c_{CO2}N_P}{c_T D_{P/CO2,e}}+\frac{c_W N_{CO2}}{c_T D_{CO2/W,e}} \tag{3.8}$$

$$c_T = c_P + c_{CO2} + c_W \tag{3.9}$$

$$N_{CO2} = -3N_P \tag{3.10}$$

$$R_{V,AN} = N_{uA}\frac{4\pi D_{P,e} D_P (R_A + L_F) K_P c_P R_A (\sqrt{\Psi} R_A \coth(\sqrt{\Psi} R_A) - 1)}{D_P (R_A + L_f) + L_F D_{P,e} (\sqrt{\Psi} R_A \coth(\sqrt{\Psi} R_A) - 1)} \tag{3.11}$$

$$\Psi = -\left(\frac{S_A i_o}{4F c_P^{*} D_{P,e}}\right)\left[\exp\left(\frac{a_{a,AN} F\eta}{RT}\right) - \exp\left(-\frac{a_{c,AN} F\eta}{RT}\right)\right] \tag{3.12}$$

$$\eta = \Phi_S - \Phi_E - E_{EQ,AN} \tag{3.13}$$

$$\frac{d\Phi_E}{dz} = -\frac{N_{+,AN}}{k_e} \tag{3.14}$$

$$\frac{dN_{+,AN}}{dz} = R_{+,AN} \tag{3.15}$$

$$R_{+,AN} = 20 F R_{V,AN} \tag{3.16}$$

The equations that apply to the cathode gas-diffusion layer are:

$$\frac{dN_{O2}}{dz} = 0 \tag{3.17}$$

$$-\frac{dc_{O2}}{dz}=\frac{N_{O2}}{D^{K}_{O2,,e}}+\frac{c_W N_{O2}-c_{O2}N_W}{c_T D_{O2/W,e}}+\frac{c_{N2} N_{O2}}{c_T D_{O2/N2,e}} \tag{3.18}$$

$$\frac{dc_{N2}}{dz} = \frac{c_{N2}N_{O2}}{c_T D_{O2/N2,e}} + \frac{c_{N2}N_W}{c_T D_{N2/W,e}} \tag{3.19}$$

$$c_T = c_{O2} + c_{N2} + c_W \tag{3.20}$$

$$N_W = -2N_{O2} \tag{3.21}$$

The equations that apply to the cathode catalyst layer are:

$$\frac{dN_{O2}}{dz} = -R_{V,CAT} \tag{3.22}$$

$$-\frac{dc_{O2}}{dz} = \frac{N_{O2}}{D^K_{O2,e}} + \frac{c_W N_{O2} - c_{O2}N_W}{c_T D_{O2/W,e}} + \frac{c_{N2}N_{O2}}{c_T D_{O2/N2,e}} \tag{3.23}$$

$$\frac{dc_{N2}}{dz} = \frac{c_{N2}N_{O2}}{c_T D_{O2/N2,e}} + \frac{c_{N2}N_W}{c_T D_{N2/W,e}} \tag{3.24}$$

$$c_T = c_{O2} + c_{N2} + c_W \tag{3.25}$$

$$N_W = -2N_{O2} \tag{3.26}$$

$$R_{V,CAT} = N_{uA} \frac{4\pi D_{O2,e} D_{O2} (R_A + L_F) K_{O2} c_{O2} R_A (\sqrt{\Psi} R_A \coth(\sqrt{\Psi} R_A) - 1)}{D_{O2}(R_A + L_F) + L_F D_{O2,e} (\sqrt{\Psi} R_A \coth(\sqrt{\Psi} R_A) - 1)} \tag{3.27}$$

$$\Psi = \left(\frac{S_A i_o}{4F c^*_{O2} D_{O2,e}} \right) \left[\exp\left(\frac{a_{c,CAT} F\eta}{RT} \right) - \exp\left(-\frac{a_{a,CAT} F\eta}{RT} \right) \right] \tag{3.28}$$

$$\eta = \Phi_S - \Phi_E - E_{EQ,CAT} \tag{3.29}$$

$$\frac{d\Phi_E}{dz} = -\frac{N_{+,CAT}}{k_e} \tag{3.30}$$

$$\frac{dN_{+,CAT}}{dz} = -R_{+,CAT} \tag{3.31}$$

$$R_{+,CAT} = 4FR_{V,CAT} \tag{3.32}$$

3.2 Boundary conditions

The coupling of the equations listed in the previous section will be described here, followed by the set of boundary conditions applying to the differential equations. For example, in the system that describes the catalyst layer in the anode (equations 3.6-3.16), the differential equations describe the variation of the following variables: N_P, c_P, c_{CO2}, Φ_E and N_+. The interrelation between these variables can be seen by considering the functional dependencies between them:

$$\frac{dN_P}{dz} = f_1(c_P, \Phi_E) \qquad \text{from (3.6, 3.11, 3.12 and 3.13)}$$

$$\frac{dc_P}{dz} = f_2(N_P, c_P, c_{CO2}) \qquad \text{from (3.7)}$$

$$\frac{dc_{CO2}}{dz} = f_3(N_P, c_P, c_{CO2}) \qquad \text{from (3.8)}$$

$$\frac{d\Phi_E}{dz} = f_4(N_{+,CAT}) \qquad \text{from (3.14)}$$

$$\frac{dN_{+,CAT}}{dz} = f_5(c_P, \Phi_E) \qquad \text{from (3.15, 3.16, 3.11, 3.12 and 3.13)}$$

For the anode gas-diffusion layer:

$$\frac{dN_P}{dz} = 0 \qquad \text{from (3.1)}$$

$$\frac{dc_P}{dz} = f_6(N_P, c_P, c_{CO2}) \qquad \text{from (3.2)}$$

$$\frac{dc_{CO2}}{dz} = f_7(N_P, c_P, c_{CO2}) \qquad \text{from (3.3)}$$

Therefore, in order to solve the system of equations for the anode electrode, three boundary conditions are required for the gas-diffusion layer and five boundary conditions are required for the catalyst layer. **Figure 3.1** shows the nomenclature for specifying the boundary conditions and the coordinate system. The – and + superscripts denote the left and right side of the boundary between two successive layers.

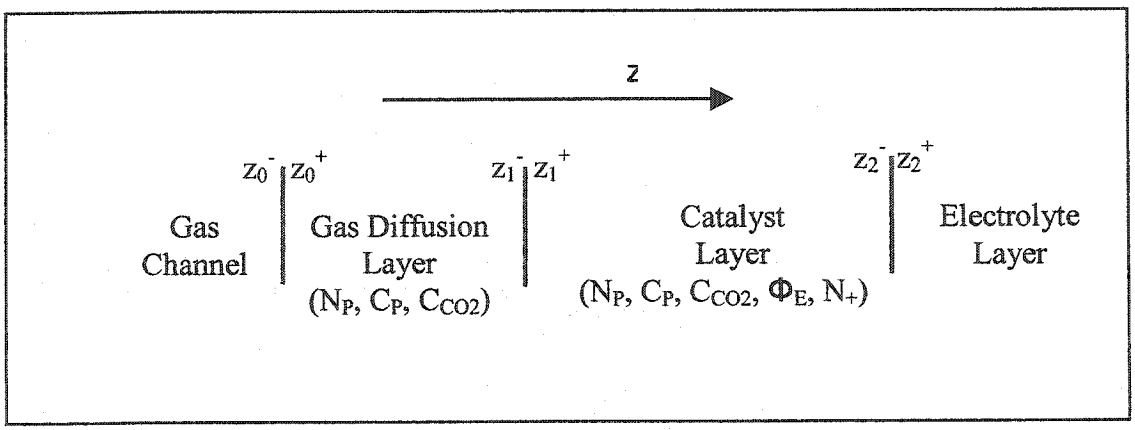

Figure 3.1: Boundaries nomenclature and system variables (anode)

The electrical potential in the electrolyte can be specified arbitrarily at a certain position in the catalyst layer because it is a relative quantity. We can then specify:

$$\Phi_E(z_1^+) = 0 \qquad \text{(BC1)}$$

The concentrations of the gases in the gas channel are calculated for this one-dimensional model by specifying the total gas pressure and composition (mole fractions) in the gas channel. Therefore:

$$c_P(z_0^-) = c_{P(GC)} \tag{3.33}$$

$$c_{CO2}(z_0^-) = c_{CO2(GC)} \tag{3.34}$$

Furthermore, at the boundaries z_1 and z_2, the gas concentrations and fluxes are required to be continuous. Therefore:

$$c_P(z_0^+) = c_{P(GC)} \tag{BC2}$$

$$c_{CO2}(z_0^+) = c_{CO2(GC)} \tag{BC3}$$

$$c_P(z_1^+) = c_P(z_2^-) \tag{BC4}$$

$$c_{CO2}(z_1^+) = c_{CO2}(z_1^-) \tag{BC5}$$

$$N_P(z_1^+) = N_P(z_1^-) \tag{BC6}$$

Also, at the boundary between the catalyst layer and the gas-diffusion layer, the ionic flux must be zero because liquid pores terminate at this position:

$$N_{+,AN}(z_1^+) = 0 \tag{BC7}$$

At the boundary between the catalyst layer and the electrolyte layer the propane flux in the gas pores is required to be zero, because gas pores terminate at this boundary:

$$N_P(z_2^-) = 0 \tag{BC8}$$

The right number of boundary conditions has been specified to properly define the solution of the system of differential equations, but special care is needed to solve the system numerically as some boundary conditions are given at the right boundary, while some are given are the left, so that the system is not a standard initial value problem. The subject will be discussed in detail in section 3.5.

The system of differential equations describing the processes in the cathode is completely analogous. The functional dependencies between the variables are:

$$\frac{dN_{O2}}{dz} = g_1(c_{O2}, \Phi_E) \qquad \text{from (3.22, 3.27, 3.28 and 3.29)}$$

$$\frac{dc_{O2}}{dz} = g_2(N_{O2}, c_{O2}, c_{N2}) \qquad \text{from (3.23)}$$

$$\frac{dc_{N2}}{dz} = g_3(N_{O2}, c_{O2}, c_{N2}) \qquad \text{from (3.24)}$$

$$\frac{d\Phi_E}{dz} = g_4(N_{+,CAT}) \qquad \text{from (3.30)}$$

$$\frac{dN_{+,CAT}}{dz} = g_5(c_{O2}, \Phi_E) \qquad \text{from (3.31, 3.32, 3.27, 3.28 and 3.29)}$$

With the coordinate system specified in the direction from the gas channel towards the electrolyte layer, **Figure 3.2** shows the nomenclature for specification of boundary conditions and the relevant variables in the differential equations.

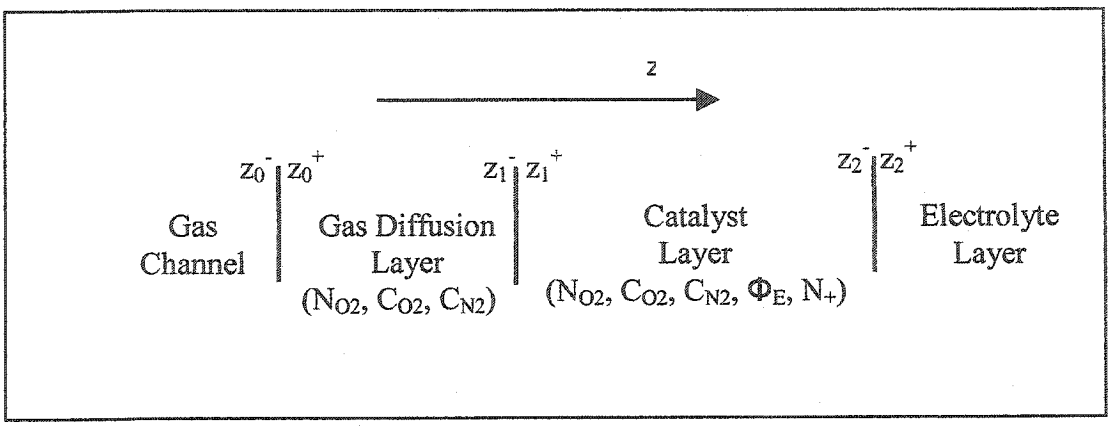

Figure 3.2: Boundaries nomenclature and system variables (cathode)

The boundary conditions are listed below:

$$c_{O2}(z_0^+) = c_{O2(GC)} \tag{BC9}$$

$$c_{N2}(z_0^+) = c_{N2(GC)} \tag{BC10}$$

$$\Phi_E(z_1^+) = 0 \tag{BC11}$$

$$c_{O2}(z_1^+) = c_{O2}(z_2^-) \tag{BC12}$$

$$c_{N2}(z_1^+) = c_{N2}(z_1^-) \tag{BC13}$$

$$N_{O2}(z_1^+) = N_{O2}(z_1^-) \tag{BC14}$$

$$N_{+,AN}(z_1^+) = 0 \tag{BC15}$$

$$N_{O2}(z_2^-) = 0 \tag{BC16}$$

3.3 Simulation of half-cell polarization curves: strategy

The differential-algebraic system of equations described in the previous section can be solved numerically under the specified boundary conditions. In this model, the two systems of equations describing the anode and the cathode of the cell are solved separately to obtain the half-cell potential versus current density (polarization) curves for the anode and the cathode electrodes. Simulation of the cell polarization curve can be obtained from these two curves as will be shown in the next section.

In the polarization curve describing the performance of a single electrode, the measured half-cell potential (experimental) corresponds to the difference between the solid phase potential Φ_S, measured at a convenient location in the electrode (usually at $z = z_0$ in Figures 3.1, 3.2), and the electrolyte potential Φ_E at the electrolyte side of the electrode (boundary $z = z_2$ in Figures 3.1 and 3.2). This definition of electrode potential is also used by other researchers in simulating half cell electrodes (Maja *et al*, 2001, Cutlip *et al*, 2001). In this model it has been assumed that the electronic conduction in the solid is infinitely fast (much faster than ionic conduction). Therefore, the potential in the solid will be the same throughout the catalyst layer. The electrical potential difference Φ_S-Φ_E at the catalyst layer–electrolyte layer boundary (z_2) coincides with the measurable electrode potential of a half-cell, shown as the y-axis of the polarization curve. The x-axis of the polarization curve is the current-density per unit electrode face area. This quantity can be found by numerically integrating the current produced in the catalyst layer with respect to the coordinate z, from z_1 to z_2. Thus, the simulated polarization curve is the following:

$$E = \left[\Phi_S - \left(\Phi_E\Big|_{z=z_2}\right)\right] \quad \text{versus} \quad I = nF\int_{z_1}^{z_2} R_V dz \qquad \text{(Definition of half-cell polarization curve)}$$

In order to simulate one point in the polarization curve for one electrode, one can start by specifying the electrode potential and solve the system of differential equations described in the previous section. Because the electrolyte potential has been specified as a boundary condition, the solid potential has to be specified at the start of the simulation. In order to simulate the whole polarization curve the following approach is followed: The solid potential (Φ_S) is first set to a value close to the equilibrium potential (E_{EQ}) of the half-cell reaction and the equation system describing the electrode is solved numerically. The quantities required to obtain one point of the

polarization curve are then computed. Subsequently, the solid potential (Φ_S) is stepped up or down (depending on the electrode) to a new value and the procedure is repeated to obtain a new point in the polarization curve. The set values for Φ_S are closely spaced together in order to increase the number of simulated points. In this manner, the whole half-cell polarization curve can be simulated. The values for the various electrochemical and physico-chemical properties required by the model will be examined in Chapter 4.

3.4 Simulation of cell polarization curves: strategy

When the polarization curves for each electrode (anode and cathode) have been obtained, the polarization curve for the unit cell can be obtained as the difference between the cathode and anode half-cell potentials, diminished by the potential drop through the electrolyte layer. It is important to note that the quantity often referred to as the iR-drop (ionic conduction loss) in the cell, includes components in the electrodes themselves and the electrolyte compartment between them. However, the potential loss in the electrodes' catalyst layers, caused by ionic conduction limitations (the electrode iR-drop), is a distributed quantity and has been included into the equation systems describing each electrode. Hence, in simulating the cell polarization curve, only the potential loss across the electrolyte has to be subtracted from the potential difference between the anode and the cathode.

At any point in the polarization curve, in order for the system to maintain conservation of charge, the ionic current density at any position in the electrolyte layer must be equal to the total current produced per unit electrode surface area ($\mathbf{I}$). Therefore, for each current-density the potential loss through the electrolyte layer can be given by:

$$\Delta\Phi_{EL} = \frac{\mathbf{I}L_{EL}}{k} \tag{3.35}$$

where L_{EL} is the thickness of the electrolyte layer and $\mathbf{I}$ the produced current-density. No adjustment has been made for the electrolyte specific conductivity in the electrolyte layer for porosity and tortuosity under the assumption that the electrolyte matrix is a very porous structure.

The cell polarization curve can then be defined as the following curve:

$E_{CELL} = E_{CAT} - E_{AN} - \Delta\Phi_{EL}$ versus I (Definition of cell polarization curve)

where I is the current density per unit face surface area of either the cathode or the anode electrodes and E_{CAT}, E_{AN} are the half-cell potentials for the anode and the cathode respectively.

The subtraction between the anode and cathode half-cell potentials has to be done at the same current density I, in order to obtain one point in the cell polarization curve. When the half-cell polarization curves are simulated for the anode and the cathode, the simulated points do not necessarily correspond to the same current-densities because the current-densities can not be set prior to solution of the system (they are obtained by integrating the volumetric current production rate in the catalyst layers). Therefore to perform the subtraction at the same current-densities the simulated data for the two half-cell polarization curves must be interpolated to the same current-densities I. In this simulation, the half-cell potentials obtained from the two half-cell polarization curves were converted to data at the same current-densities by utilizing a numerical interpolation algorithm. The values for the various electrochemical and physico-chemical properties required by the model will be examined in Chapter 4.

3.5 Solution of the differential-algebraic equation system: the Shooting method

After the strategy for obtaining the anode, cathode and cell polarization curve had been set, an efficient solution procedure was required for the differential-algebraic equation systems for the anode and the cathode electrodes. The set of equations consists of equations 3.1-3.16 for the anode electrode (gas diffusion layer and catalyst layer) and 3.17-3.32 for the cathode electrode (gas diffusion layer and catalyst layer) under the boundary conditions BC1-BC8 for the anode electrode and BC9-BC16 for the cathode electrode. Separate solutions were obtained for each electrode by specifying the electrical potential in the solid phase Φ_S, appearing in equations 3.13 and 3.29, in the anode and cathode systems respectively. This results in one point of the half-cell polarization curve. The two systems of equations (anode and cathode) are completely analogous hence discussion of the solution of only one will suffice. In this section, the discussion will be referring to the cathode electrode.

There exists a numerical difficulty in solving the set of differential equations 3.17-3.32 because the boundary conditions are specified at the opposite ends of the electrode. In particular the oxygen and nitrogen gas concentrations can only be specified at the boundary between the gas

channel and the gas-diffusion layer z_o^+ (BC10 and BC11) while the oxygen gas flux must satisfy the zero flux conditions at the boundary between the catalyst layer and the electrolyte layer z_2^- (BC16). Alternatively, it can be said that Equation 3.17 comes with a final condition at $z = z_2$, while Equations 3.18 and 3.19 have an initial condition at $z = z_0$ if the differential equations are solved in the forward direction from z_0 to z_2. Solving in the backward direction, from z_2 to z_0, does not help either (two final conditions would arise in that case). This complication prohibits the numerical solution by a one-shot method proceeding in one direction through the electrode. If the system of equations is solved sequentially for the gas diffusion and catalyst layer proceeding from boundary z_o to z_2 by arbitrarily choosing a boundary value for N_{O2} at z_0^+, BC16 will not necessarily be satisfied. Also, if the system is solved in the opposite direction by arbitrarily selecting c_{O2} and c_{N2} at z_2^-, BC9 and BC10 will not be necessarily satisfied. Therefore an iterative method is required to satisfy the boundary conditions.

The iterative procedure used in this simulation to overcome this difficulty is referred to as the 'shooting' method. Application of this method can be described as follows: the missing condition at one end of the system boundary (N_{O2} at z_0^+) is used as a control variable in order to satisfy the target condition at the other end of the system boundary ($N_{O2} = 0$ at z_2^-). Initially, the control variable $N_{O2}(z_0^+)$ is set to an arbitrary value and the system of equations is solved for the gas diffusion and catalyst layers proceeding in the positive z-direction (in which case all equations have specified initial conditions). When the system is solved, the target condition $N_{O2}(z2^+) = 0$ will probably not be satisfied, i.e. $N_{O2}(z2^+) \neq 0$. In the next iteration the value of the control variable is updated according to the Newton-Raphson formula:

$$N^{i}_{O2(z_0^-)} = N^{i-1}_{O2(z_0^-)} - \frac{N^{i-1}_{O2(z_0^-)}}{\left(\frac{dN^{i-1}_{O2(z_2^+)}}{dN^{i-1}_{O2(z_0^-)}} \right)} \tag{3.36}$$

(superscript i refers to the iteration number)

The derivative $\frac{dN_{O2(z_2^+)}}{dN_{O2(z_0^-)}}$ was evaluated numerically by introducing a small perturbation $\Delta N_{O2}(z_o^-)$ to $N_{O2}(z_o^-)$ and resolving the system. A new value of $N_{O2}(z_2^+)$ is obtained and the value

$\Delta N_{O2}(z_2^+)/\Delta N_{O2}(z_o^-)$ is an approximation to the derivative $\frac{dN_{O2(z_2^+)}}{dN_{O2(z_0^-)}}$. It was found by trial and error that by taking the value for the perturbation $\Delta N_{O2}(z_o^-) = 10^{-9} N_{O2}(z_o^-)$, the convergence rate is fast. The procedure was repeated using the updated value of $N_{O2}(z_o^-)$ as the boundary condition for equation 3.17 and the system of equation was re-solved. This method resulted in satisfying the target condition $N_{O2}(z2^+) = 0$ to within the specified tolerance after very few iterations. The tolerance specified in this simulation was normalized with respect to the inlet flux at z_o^+. The condition required to be satisfied for convergence was:

$$\left|\frac{N_{O2}(z_2^+)}{N_{O2}(z_0^+)}\right| < 10^{-7} \tag{3.37}$$

Within each iteration, the sets of differential-algebraic equations in the gas diffusion and catalyst layers were solved by utilizing standard differential equation solvers provided in the software package MATLAB. The solver used is an implementation of the Runge-Kutta (2, 3) method. The code was written in MATLAB. A sample program for a cathode electrode and a sample program for an anode electrode are attached in **Appendix B** (B1 and B2, respectively). A sample program for the calculation of potential losses in the electrolyte layer is attached (Appendix B3). It should be noted that the algorithm is not computationally expensive. A program that simulates a half-cell polarization curve for a given set of conditions (for either the anode or the cathode) runs in less than 2 minutes.

After convergence, a point in the polarization was obtained, as described in the previous section. The solid potential is then stepped down by 0.01V to obtain a different point in the polarization curve, until the cathode polarization curve is simulated. The procedure is completely analogous for simulating the anode polarization curve. A few variations and extensions of the techniques described here, such as the procedure used to obtain contour plots of constant potential loss, are described in Chapter 5.

Figure 3.3 shows the various solution variables along z at convergence for the cathode electrode obtained from the shooting method, for a particular current density, particular electrode characteristics and operating conditions. The distributions are included here, not for the purpose

of showing results (which will be described in Chapters 5 and 6), but rather to illustrate the fact that the specified boundary conditions are satisfied by the solution of the model.

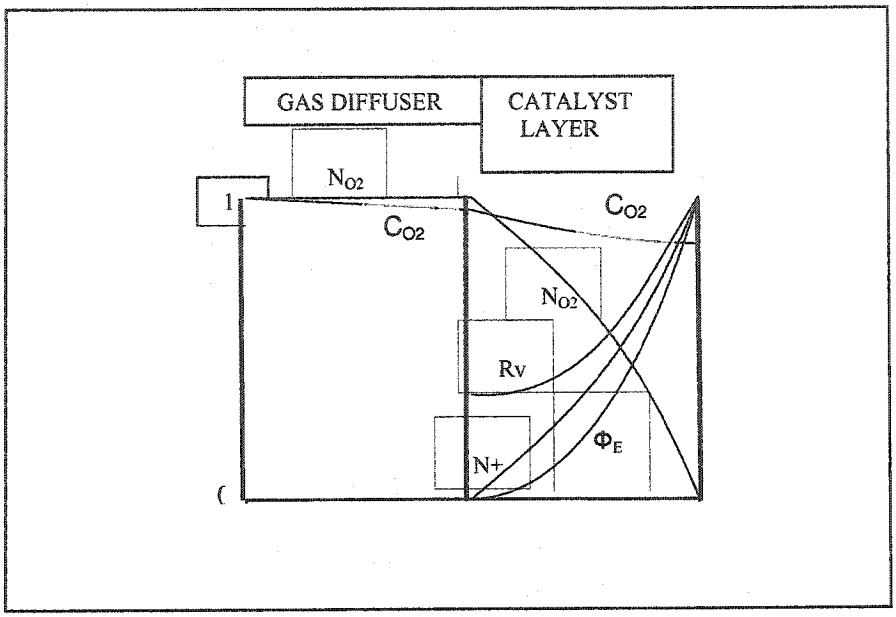

Figure 3.3: Normalised solution variables across the cathode electrode's catalyst layer and gas diffusion layer at convergence

CHAPTER 4: ELECTROCHEMICAL AND PHYSICOCHEMICAL PROPERTIES

4.1 Introduction

Application of the mathematical model that has been developed in the previous chapters requires the use of many electrochemical and physicochemical properties. Experimental data for many of these properties have been found in the literature. In some cases, experimental data are either absent in the literature searched or cannot be measured, so that estimation methods were employed. The variation of many of these properties with operating conditions, such as temperature, pressure and phosphoric acid concentration, has been considered. In most cases, the experimental data describing these dependencies were fitted into simple models, such as polynomial or exponential models. The advantage of taking this approach, instead of simply using tabulated data, is that it allows simulations with more operating / input values. In some cases, extrapolation of experimental data to values of the independent variable slightly outside of the range reported is required. In these cases, care has been taken to use model forms that do not present extreme changes in slope in the extrapolated region compared to the range in which the fitting has been done.

The quantities that were estimated in order to be used in the model include the following: the exchange current-densities, transfer coefficients and standard activation energies for the propane oxidation reaction and the oxygen reduction reaction, the effective surface area of platinum in the electrode, binary gas diffusion coefficients and Knudsen diffusion coefficients for the gases, the diffusivity and solubility of propane and oxygen in phosphoric acid, the specific conductivity of the electrolyte, porosity and tortuosity corrections for all diffusivities and conductivities, the vapour pressure and boiling point of phosphoric acid, the activity of water in phosphoric acid, the equilibrium potentials for the anode and cathode. Correlations were developed for each of the required properties that account for its variation with the operating variables that have an effect on them (temperature, pressure, phosphoric acid concentration etc.).Unless stated otherwise, the correlations were obtained using linear regression provided by the Excel program.

In estimating these parameters, it has been taken into account that the temperature range of interest in this study is 120-230°C, the acid concentration range of interest in this study is 75-110 wt % phosphoric acid and the pressure range of interest is 1-10 atm. Normally, a PAFC operates

at temperatures 150-220°C and acid concentration close to 100%H_3PO_4 (Hirschenhofer *et al*, 1998). Hirschenhofer *et al* (1998) reports the construction of PAFC's operating from 1 atm to 8.2 atm gas pressure. It should be noted that phosphoric acid concentration that exceeds 100% is common terminology in the literature. Phosphoric acids forms acid dimers by condensation (2 $H_3PO_4 = P_2O_5 + 3H_2O$). Thus, 100% H_3PO_4 contains water molecules within the liquid structure. The weight percentage of P_2O_5 in 100% phosphoric acid is 72.43%. Therefore, if more water is removed from 100% phosphoric acid, the nominal concentration of the H_3PO_4 acid exceeds 100%, whereas the P_2O_5 content remains less than 100%.

Moreover, there is some uncertainty in all of the parameters that are reported in this study. In most cases, this uncertainty cannot be easily quantified. Thus, the estimated parameters should not be considered the true values but the most plausible values according to existing information. In a later chapter, the effect of using different values for these parameters will be considered, in the form of a sensitivity analysis, to determine those that have a significant effect on the results.

The quantities that are most uncertain in this model are the electrochemical parameters pertaining to the propane oxidation reaction. The reason is twofold: the propane oxidation reaction has not been sufficiently studied in the literature. Furthermore, the quantities required in the Butler-Volmer equation are empirical quantities that can only be derived from experiments because the details of the reaction mechanism are unknown. Thus, the exchange current-density and standard activation energy for the propane oxidation reaction have been estimated on the basis of available experimental data, using the presently developed model.

4.2 Electrochemical parameters

The electrochemical parameters required in this model are the values for the exchange current-density i_o^* at some reference temperature T* for the oxygen reduction reaction and the propane oxidation reaction, the activation energy $\Delta G^{\neq}$ for the exchange current density for the two reactions and the anodic and cathodic transfer coefficients α_a and α_c, to be used in conjunction with equations 2.22 and 2.25 (reaction rate equations). The transfer coefficients that are more important are the cathodic transfer coefficient for the oxygen reduction reaction and the anodic transfer coefficient for the anodic propane oxidation reaction. This is because the two reactions are very irreversible and the exponential term in the Butler-Volmer equation (2.24) that pertains to the opposite direction of the reaction can be ignored for practically all but the extremely

smallest current densities (this means that the Tafel equation can also be used instead of the Butler- Volmer equation for both reactions). Nevertheless, both transfer coefficients are considered here.

The reaction orders with respect to the propane concentration, oxygen concentration and activity of water in solution have already been mentioned in Chapter 2 in conjunction with the development of the mathematical model. The oxygen reduction reaction was taken to be first-order with respect to the dissolved oxygen concentration (Appleby, 1974), and the propane oxidation reaction was taken to be first-order with respect to both the dissolved propane concentration (Bockris and Srinivasan, 1969) and the activity of water in phosphoric acid because water is a reactant in the anode. Also, from the reactions' stoichiometry, the number of moles of electrons (equivalents) transferred per mole of reactant consumed is n = 4 for oxygen reduction and n = 20 for propane oxidation.

The exchange current-density for the oxygen reduction reaction on platinum in phosphoric acid electrolyte is reported by Appleby (1970) to be $i_o^* = 3.8\times10^{-13}$ amp/cm^2 at $T^* = 25^oC$. The standard activation energy for the exchange current is reported by Kunz and Gruver (1978) and by Appleby (1970) to be 92 kJ/mole. Damjanovic and Sepa (1989) suggested that the Gibbs energy of activation also depends slightly on the pH of the solution. For the relatively small range of pH values considered here, this dependence can be ignored. The cathodic transfer coefficient for the oxygen reduction reaction on platinum is reported by Kunz and Gruver (1975) to be α_c =1.The transfer coefficient has been found to be independent of electrolyte concentration (Kunz and Gruver, 1978). It should be noted that other results in the literature indicate a change in the transfer coefficient at very concentrated solutions (Glass *et al*, 1989). Other researchers note the effect of possible impurities in the phosphoric acid electrolyte, such as phosphorous acid (Sugishima *et al*, 1994). In this model, it is considered that the acid concentration does not affect the transfer coefficient for the oxygen reduction reaction. The anodic transfer coefficient for the reaction, which corresponds to the transfer coefficient for the reverse reaction (the oxygen evolution reaction) is reported by Bockris and Srinivasan (1969) to be α_a =1. Fundamental aspects of the oxygen reduction reaction have been discussed by various authors (Damjanovic, 1969, Tarasevich *et al*, 1983, Markovic *et al*, 2001).

The anodic transfer coefficient for the propane oxidation reaction on platinum in acid electrolyte is reported by Bockris and Srinivasan (1969) to be α_a =1. The cathodic transfer coefficient for the

reaction is also considered here to be α_c =1.For the exchange current density i_o^* and the activation energy $\Delta G^{\neq}$, the following values were found to be consistent with the experimental data reported in Grubb and Michalske (1964): $i_o^*=10^{-8}$ amp/cm^2 at 150°C and $\Delta G^{\neq}$ = 90 kJ/mole for the temperature range 120-230 °C. The exchange current for propane oxidation and its activation energy were chosen such that the results of the model can predict the given sets of experimental data. More fundamental aspects of the reaction relate to adsorption phenomena on the catalyst surface and the reaction mechanism (which has not yet been clarified) that are not accounted for in this model. It should be noted that the value used for the activation energy for the exchange current corresponds to ~15 kcal / mole (= $-\Delta G^{\neq} + \alpha\eta F$) at anodic overpotential of 280mv, which is reported by Cairns (1971) as the activation energy for propane adsorption on platinum. Also, the values used for the exchange current-density and its activation energy result in a value of 3.5×10^{-11} amp/cm^2 at 80°C (from equation 2.25), which is of the same order of magnitude as the exchange current-density for ethylene oxidation at the same temperature on platinum metal in acid electrolyte (~10^{-10} amp/cm^2 (Bockris and Srinivasan (1969)). Therefore, the values used for these parameters are clearly realistic.

It should be noted that the exchange current-density and activation energies for electrochemical reactions such as the oxygen reduction and propane oxidation reaction, can not be regarded as physical constants. For example, platinum has been found to exhibit different intrinsic activities with respect to the oxygen reduction reaction at different electrodes or for different catalyst surface preparation conditions. Several variables, the effects of which are difficult to quantify, such as the physical state of the platinum surface or catalyst ageing effects, are responsible for the variability of electrochemical parameters on different electrodes. The values used in this model should therefore be considered as approximate.

4.3 The diffusivity of oxygen in phosphoric acid

Experimental data on the diffusivity of oxygen in 98% phosphoric acid at various temperatures in the temperature range 25 – 150 °C are reported by Scharifker *et al* (1987). The data are presented graphically in **Figure 4.1**. The equation of the fitting line is:

$$\ln(D_{O2,98\%}) = -3100\left(\frac{1}{T}\right) - 3.04 \qquad (4.1)$$

Therefore, the diffusion coefficient (cm^2/s) of oxygen in 98% H_3PO_4 depends on the temperature according to:

$$D_{O2,98\%} = 0.048 \exp(-\frac{25770}{RT}) \quad (4.2)$$

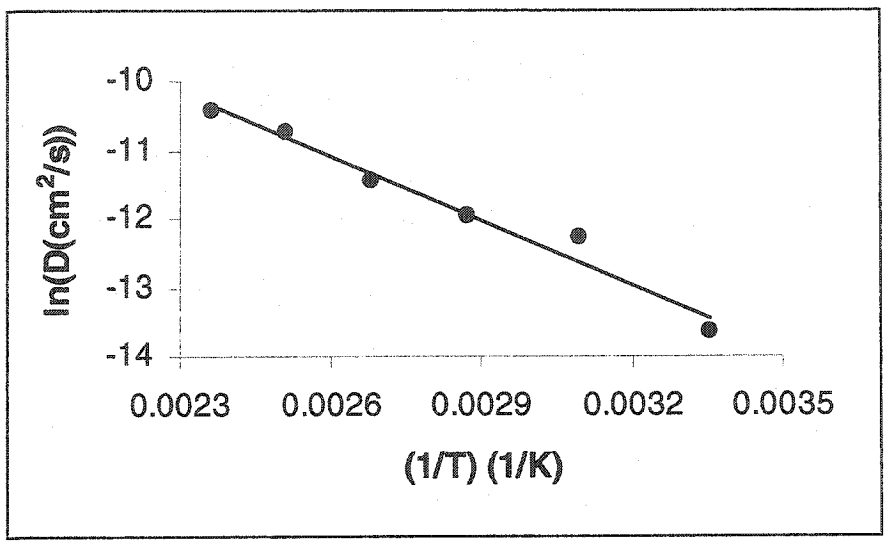

Figure 4.1: Temperature dependence of oxygen diffusivity in phosphoric acid

Experimental data on the variation of oxygen diffusivity with phosphoric acid concentration were not found in the literature. The variation can be approximated using the Stokes-Einstein relation, which states that at the same temperature the diffusivity is inversely proportional to the solution viscosity (Newman, 1973).

$$D_{O2} = D_{O2,98\%} \frac{\mu_{98\%}}{\mu} \quad (4.3)$$

Data for the viscosity of phosphoric acid solutions at 140°C were found in the literature (Gard, 1991) and are presented graphically in **Figure 4.2**. The equation of the best-fit line is:

$$\mu = 0.182 \exp(0.034\ W) \quad (4.4)$$

Therefore, from equations 4.3 and 4.4:

$$D_{O2} = D_{O2,98\%} \exp[0.034\ (98 - W)] \quad (4.5)$$

and from equations 4.5 and 4.2:

$$D_{O2} = 0.048 \exp\left[-\frac{25770}{RT} + 0.034(98 - W)\right] \tag{4.6}$$

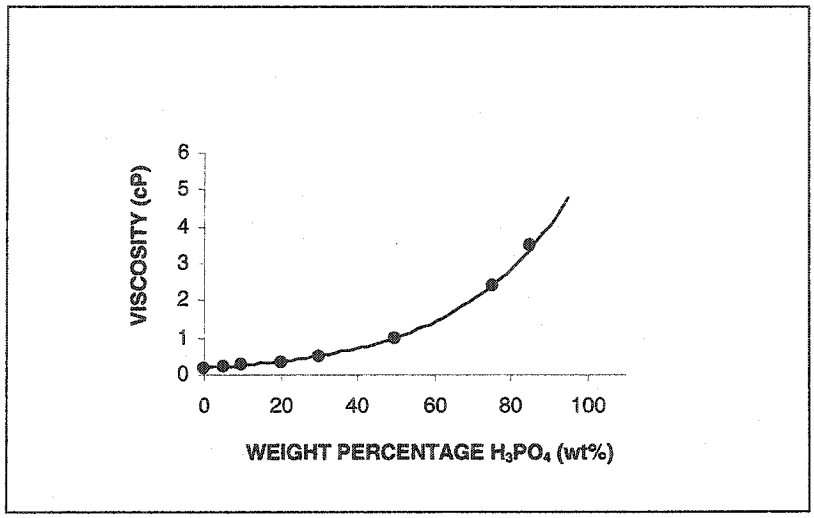

Figure 4.2: Viscosity of phosphoric acid as a function of concentration

4.4 The solubility of oxygen in phosphoric acid

The solubility of oxygen in the phosphoric acid medium is of considerable importance as it determines the cathode reagent concentration in the relevant reaction rate equation. Experimental data on the solubility of oxygen in 98% phosphoric acid for the temperature range 25-150 ^{0}C at 1 atm oxygen partial pressure were reported by Scharifker *et al* (1987) and are presented in **Figure 4.3**. For temperatures greater than 100°C, that are of interest in this study, the solubility of oxygen in the electrolyte remains approximately constant. In this study, the solubility of oxygen in phosphoric acid for temperatures greater than 100°C is taken to be constant and equal to that at 100 °C, which is $c^*_{O2} = 10^{-7}$ moles / cm^{3}atm.

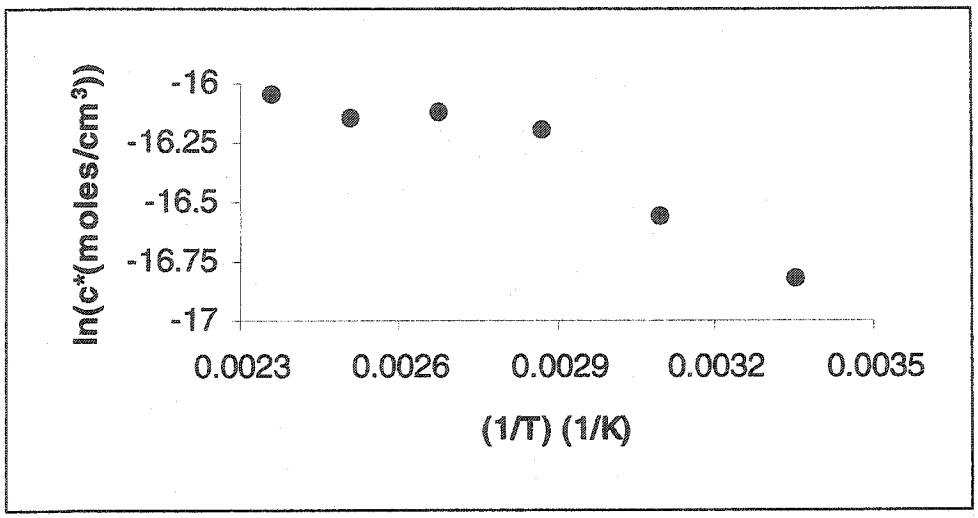

Figure 4.3: Temperature dependence of oxygen solubility in phosphoric acid

Experimental data on the variation of the solubility of oxygen with phosphoric acid concentration are reported by Gubbins and Walker (1965) and presented in **Figure 4.4.**

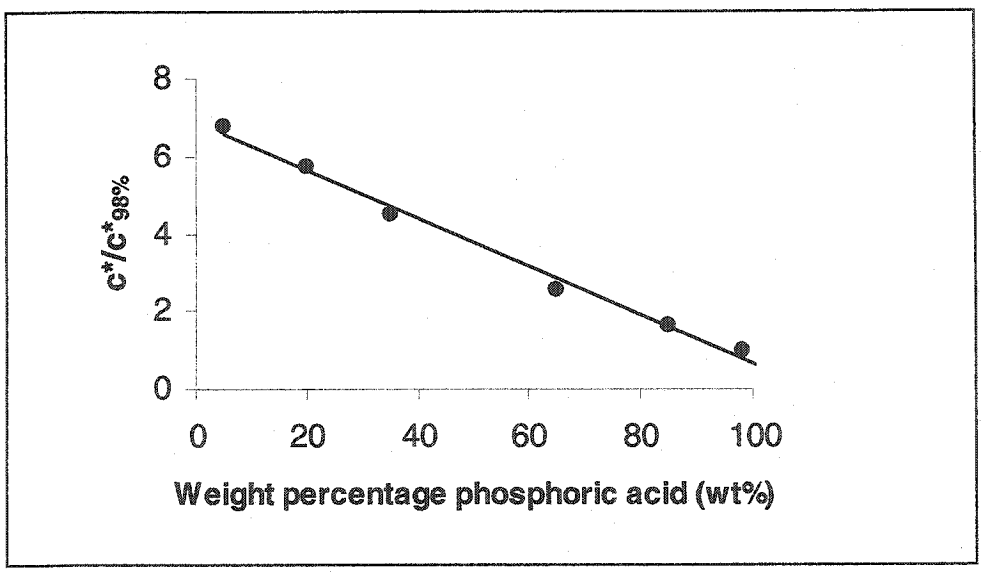

Figure 4.4: Solubility of oxygen in phosphoric acid as a function of concentration

From the equation of the linear best-fit line:

$$\frac{c^*_{O2}}{c^*_{O2,98\%}} = 6.87 - 0.062W \tag{4.7}$$

Therefore, the solubility of oxygen (moles / cm^3atm) in W wt% H_3PO_4 can be given by:

$$c^*_{O2} = 10^{-7}(6.87 - 0.062W) \tag{4.8}$$

4.5 The diffusivity and solubility of propane in phosphoric acid

The solubility of propane in phosphoric acid determines the concentration of the anode reagent in the reaction rate expression. On the basis of data reported by Bockris and Srinivasan (1969), the solubility of propane in concentrated phosphoric acid is virtually independent of temperature and electrolyte concentration for temperatures higher than 100°C in the concentration range 70-110 wt% H_3PO_4, which is of interest in this study. The solubility reported is $c^* \approx 0.175$ mmoles/l atm (Bockris and Srinivasan, 1969), which is equal to $c^* = 1.75 \times 10^{-7}$ moles / cm^3atm.

The diffusivity of propane in the electrolyte has not been determined but was estimated using the Wilke-Chang correlation (Poling *et al*, 2001). According to the correlation, the ratio of diffusion coefficients for two different dissolved gases, D_1 and D_2, in the same solvent at a given temperature, is related to the molar volumes of the gases as:

$$\frac{D_1}{D_2} = \left(\frac{\bar{V}_2}{\bar{V}_1}\right)^{0.6} \tag{4.9}$$

On the basis of molar volumes reported by the same authors, the diffusivities of propane and oxygen in the same electrolyte are related by: $D_P \approx 0.38 D_{O2}$, which was used to estimate the diffusivity of propane for different concentrations of phosphoric acid and temperatures using equation 4.6:

$$D_P = 0.38 \times 0.048 \exp\left[-\frac{25770}{RT} + 0.034(98 - W)\right] \tag{4.10}$$

4.6 Binary gas diffusion coefficients

The following relation, known as Fuller's correlation, can be used for predicting binary diffusivities of gases at various temperatures and pressures (Poling *et al*, 2001). For two gaseous species A and B:

$$D_{AB} = \frac{0.00143T^{1.75}}{PM_{AB}^{0.5}\left[(\Sigma_u)_A^{1/3} + (\Sigma_u)_B^{1/3}\right]^2} \tag{4.11}$$

where:

$$M_{AB} = 2\left[\left(\frac{1}{M_A}\right) + \left(\frac{1}{M_B}\right)\right]^{-1} \tag{4.12}$$

In equations 4.11 and 4.12, the variables represent:

D_{AB}:	The binary diffusion coefficient between A and B (cm^2 /s)
P:	Pressure (bar)
T:	Temperature (K)
M_A, M_B:	Molecular weights of A and B (g/mole)
Σ_u:	Sum of atomic diffusion volumes, a tabulated parameter.

The following molecular diffusion volumes were reported by Poling *et al* (2001):

N_2:	18.5
O_2:	16.3
CO_2:	26.9
H_2O:	13.1
C_3H_8:	(3) (15.9) + (8) (2.31) = 66.2

Using this correlation, all binary diffusion coefficients ($D_{P/CO2}$, $D_{P/W}$, $D_{W/CO2}$, $D_{O2/N2}$, $D_{O2/W}$ and $D_{N2/W}$) can be estimated as a function of the temperature and gas pressure.

4.7 Knudsen diffusion coefficients

The Knudsen diffusion coefficient of a gaseous species is related to the mean gas pore radii in the gas diffusion and catalyst layers (Geankoplis, 1972):

$$D^K = 9700\, r_P \left(\frac{T}{M}\right)^{0.5} \tag{4.13}$$

where D^K is the Knudsen diffusion coefficient (cm^2/s), r_P the mean radius of the pores (cm), T the temperature (K) and M the molecular weight of the gas (g/mole).The same equation has been used by Cutlip *et al* (1991).

For the mean gas-pore radii in the gas-diffusion and catalyst layers the following values are used by Fuller *et al* (1995):

$r_P = 5 \times 10^{-4}$ cm for the gas-diffusion layer

$r_P = 5 \times 10^{-5}$ cm for the catalyst layer

4.8 The available specific surface area of platinum

The available active surface area of platinum is reduced as the platinum loading on a carbon support increases because the platinum particles grow thicker (agglomerate). This phenomenon is called sintering and has the effect of reducing the specific activity of the catalyst (Stonehart, 1972, Watanabe *et al*, 1989, Honji *et al*, 1988).The data in **Table 4.1** are provided by an electrode manufacturer (E-TEK corporation, 2003), for Pt on Vulcan XC-72. For a different type of electrode, different values are also reported in the literature (Ralph and Hogarth, 2002).

Table 4.1: Platinum surface area for different platinum / carbon catalyst concentrations (Data provided by E-TEK Corporation)

W_{Pt}	S (m^2/g)
0.1	140
0.2	112
0.3	88
0.4	72
0.6	32

The data are presented graphically in **Figure 4.5**:

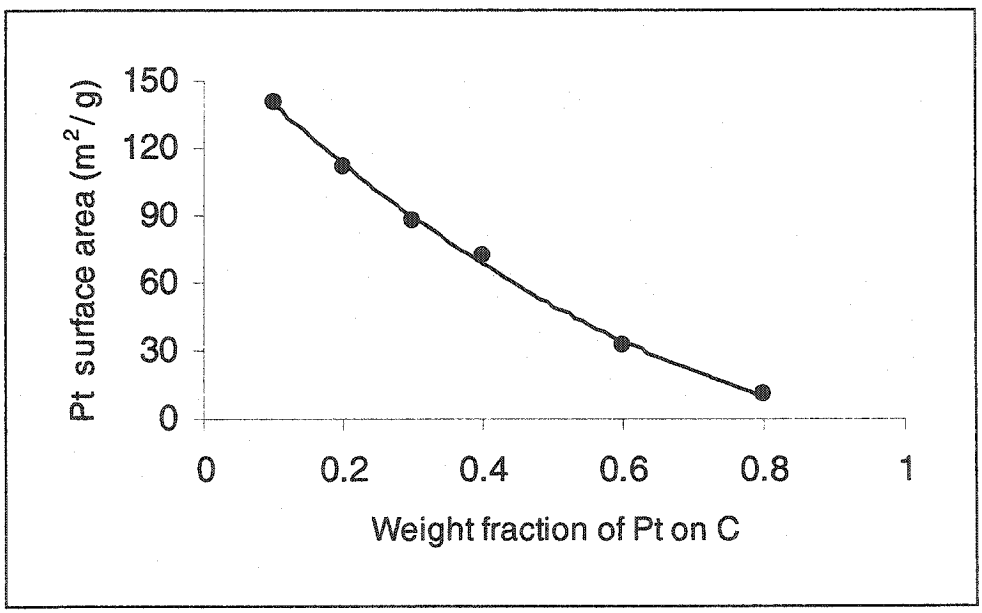

Figure 4.5: Platinum surface area as a function of the weight fraction of platinum in Pt/C catalyst

The data have been plotted and fitted to a linear model. The equation for the best-fit line is:

$$S(m^2/g) = 131 \times W_{Pt}{}^2 - 302.2 \times W_{Pt} + 168.3 \qquad (4.14)$$

Therefore, the surface area of Pt in cm^2/g is given by:

$$S = 10^4 \times (131 \times W_{Pt}^2 - 302.2 \times W_{Pt} + 168.3) \quad (4.15)$$

4.9 The activity of water in phosphoric acid

The activity of water for different molalities and wt% concentrations of up to 85% phosphoric acid is reported by Gordon and Ford (1970). Data in the concentration range 65 – 85 wt% phosphoric acid are of interest in this study (values for higher concentrations are not reported). **Table 4.2** presents the available data:

Table 4.2: Molality, mole fraction and activity of water in phosphoric acid of different concentrations

wt % H_3PO_4	Molality of solution	Mole fraction of H_2O	Activity of H_2O
65	18.95	0.746	0.443
70	23.8	0.700	0.344
75	30.6	0.644	0.246
80	40.8	0.577	0.16
85	57.9	0.490	0.095

The data in the above table show that the activity of water in the solution is much lower than the mole fraction of water, because much of the water molecules in solution are bound by interaction with phosphoric acid species and are not available to participate in the electrochemical reactions.

It was found that the variables can be correlated using simple exponential relations if the molality of the solution is first expressed as a function of the wt % and subsequently, the water activity is expressed as a function of the molality. Also, extrapolation of the data is required to obtain the water activities in more concentrated solutions. **Figures 4.6 and 4.7** present the data and the best-fit exponential model lines for these variables:

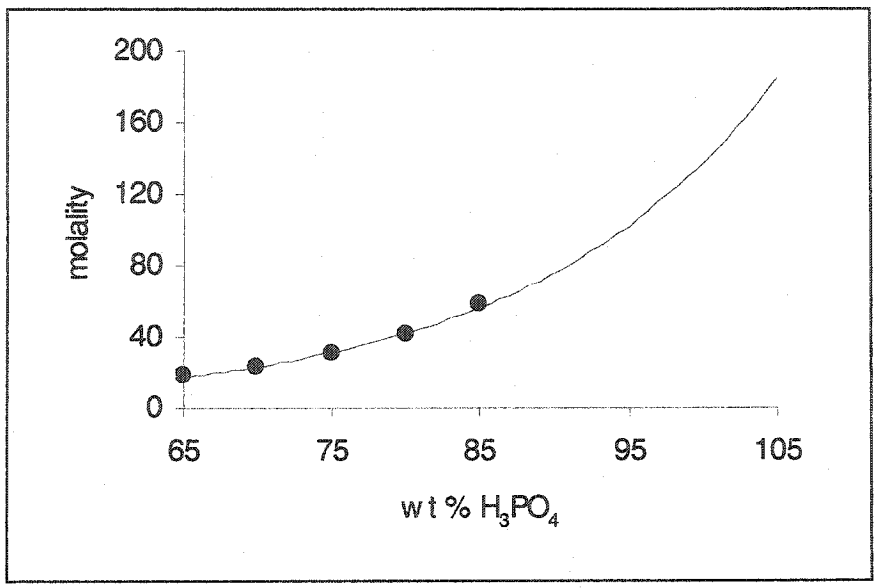

Figure 4.6: Molality of phosphoric acid solutions as a function of weight percentage

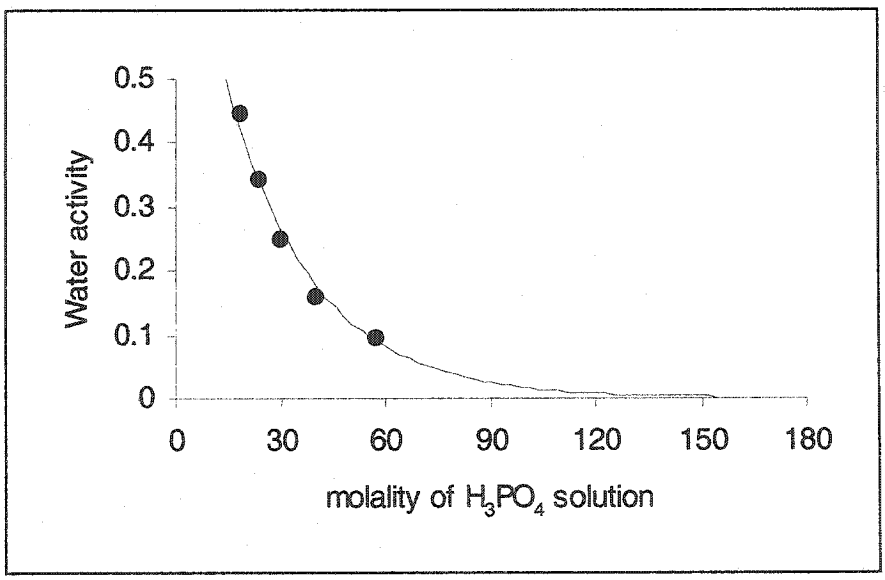

Figure 4.7: Activity of water in phosphoric acid as a function of solution molality

The equations of the fitting lines are:

$$m = 0.371 \exp(0.059\, W) \tag{4.16}$$

$$a_W = 0.870 \exp(-0.039\, m) \tag{4.17}$$

The activity of water in the phosphoric acid solution as a function of the weight percentage H_3PO_4 can be obtained using equations 4.16 and 4.17.

4.10 The specific conductivity of phosphoric acid

The specific conductivity of phosphoric acid is a function of its concentration and the temperature. Data on the specific conductivity of phosphoric acid at 298K and its temperature coefficient are reported by Dobos (1975). **Figure 4.8** summarizes the experimental data in the concentration range 70-95 wt% H_3PO_4.

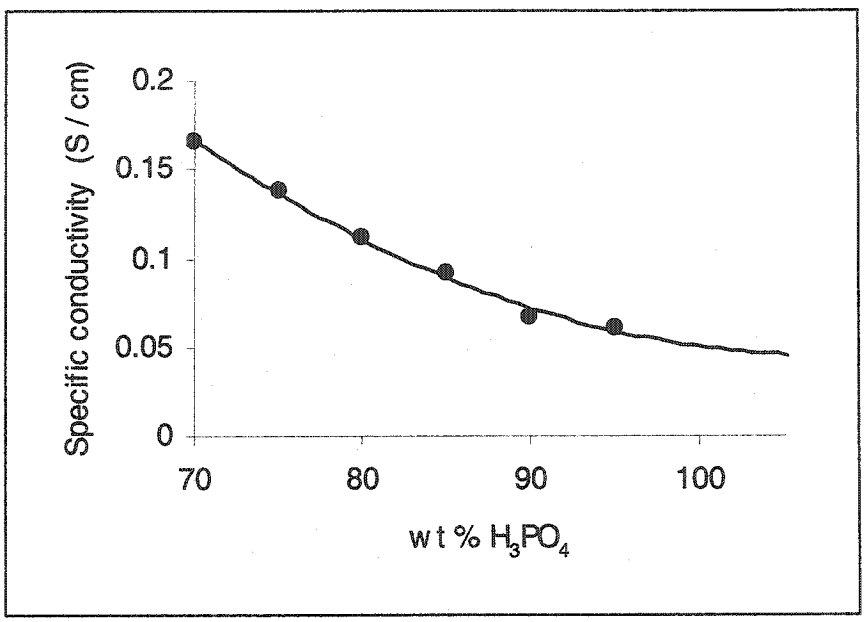

Figure 4.8: Specific conductivity of phosphoric acid as a function of concentration

The data in this concentration range have been fitted with a 2nd-order polynomial. The equation of the best-fit line is:

$$k = 8.53\times10^{-5}W^2 - 0.0184W + 1.034 \qquad (4.18)$$

The temperature variation of the specific conductivity of phosphoric acid has been described with a temperature coefficient, defined as:

$$\alpha_T = \frac{\left(\frac{k - k_{298}}{k_{298}}\right)}{T - 298} \qquad (4.19)$$

For the temperature coefficient of conductivity, data are reported by Dobos (1975) and are presented in **Figure 4.9**:

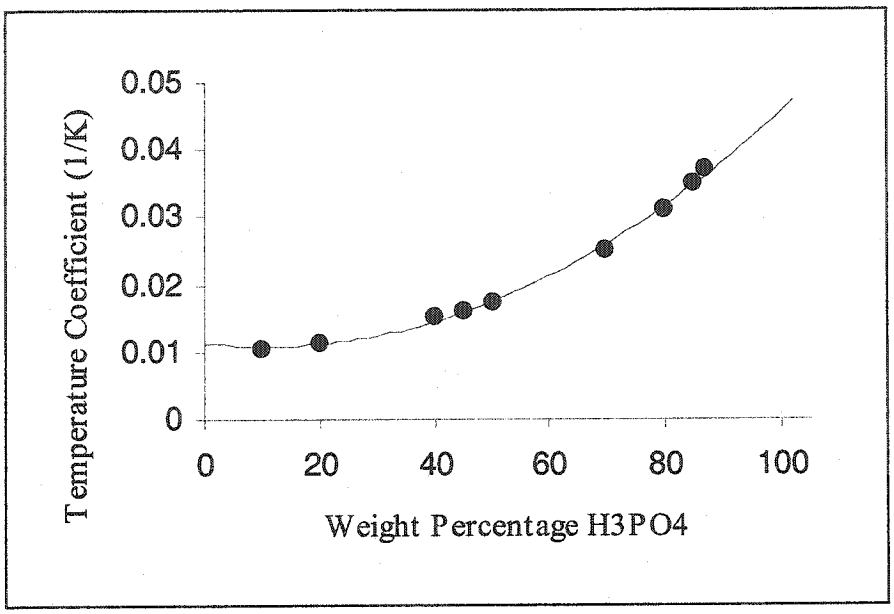

Figure 4.9: Temperature coefficient of conductivity of phosphoric acid as a function of concentration

The equation of the fitting polynomial is:

$$\alpha_T = 4.44\times10^{-6}W^2 - 1.01\times10^{-4}W + 0.0114 \qquad (4.20)$$

Then, the conductivity of phosphoric acid, from equations 4.18-4.20, can be given by:

$$k = (8.53\times10^{-5}W^2 - 0.0184W + 1.034)\times\left[1 + (4.44\times10^{-6}W^2 - 1.01\times10^{-4}W + 0.0114)(T - 298)\right] \qquad (4.21)$$

4.11 Porosity/ tortuosity corrections for the diffusivities and electrolyte conductivity

The binary gas-diffusion coefficients, Knudsen diffusion coefficients and dissolved gas-diffusion coefficients in the electrolyte, as well as the conductivity of phosphoric acid in the catalyst layer, must be corrected by taking into account the porous nature of the electrodes. The correction is done by using effective values for the porosity and tortuosity factor in the catalyst layer and the gas diffusion layer. A correlation (Bird *et al*, 1960) has been used by other researchers in modeling fuel cell layers (Kulikovsky, 1999, Yang, 2000, Yamashita and Taniguchi. 1998): the effective value of the diffusivity or conductivity in a porous fuel cell layer is assumed to be dependent to the 1.5 power of the volume fraction of the pores. Thus all diffusivities and conductivities must be multiplied by the relevant pore volume. For the conductivity, the appropriate volume fraction is the volume fraction of liquid in the catalyst layer:

$$k_e = (V_L)^{1.5} k \tag{4.22}$$

For the propane and oxygen diffusivities in the liquid, the appropriate volume fraction is the volume fraction of liquid in the agglomerates:

$$D_{O2,e} = (V_{mA})^{1.5} D_{O2} \tag{4.23}$$

$$D_{P,e} = (V_{mA})^{1.5} D_P \tag{4.24}$$

For the binary gas diffusion coefficients and the Knudsen diffusion coefficients, the appropriate volume fraction is the volume fraction of gas in the catalyst layer and the gas-diffusion layer:

$$D_{O2/W,e} = (V_G)^{1.5} D_{O2/W} \tag{4.25}$$

$$D_{O2/N2,e} = (V_G)^{1.5} D_{O2/N2} \tag{4.26}$$

$$D_{N2/W,e} = (V_G)^{1.5} D_{N2/W} \tag{4.27}$$

$$D_{P/CO2,e} = (V_G)^{1.5} D_{P/CO2} \tag{4.28}$$

$$D_{P/W,e} = (V_G)^{1.5} D_{P/W} \tag{4.29}$$

$$D_{CO2/W,e} = (V_G)^{1.5} D_{CO2/W} \tag{4.30}$$

$$D^K_{O2,e} = (V_G)^{1.5} D^K_{O2} \tag{4.31}$$

$$D^K_{P,e} = (V_G)^{1.5} D^K_P \tag{4.32}$$

4.12 Vapour pressure and boiling point of phosphoric acid

Data on the vapour pressure of phosphoric acid as a function of temperature and phosphoric acid concentration are reported by Gard (1991).The data were fitted into a linear model that accounts for correlation between the temperature and concentration effect on the vapour pressure. **Table 4.3** presents the data on which the correlation is based. As mentioned before, for H_3PO_4 concentration greater than 100%, there is still water in the solution so that there is a water pressure. A simple linear regression program was written in MATLAB to estimate the parameters. The second-order model that best fits the data, given as the mole fraction of water above the solution, is:

$$x_W = \left(\frac{1}{760}\right) \times \left(-30219.6 + 790.8\,W + 129.2T - 5.075W^2 + 0.527T^2 - 4.195TW + 0.0301TW^2 - 0.00527T^2W\right) \tag{4.33}$$

Figure 4.10 compares the model estimates with the experimental data for the conditions given in Table 4.3. The results are satisfactory. The graph does not intend to show the variation of water

vapour pressure with temperature because the data correspond to different acid concentrations. It intends to show the agreement between the calculated and experimental values.

Table 4.3: Data of equilibrium water vapour pressure of phosphoric acid for different temperatures and acid concentrations

Weight Percentage H_3PO_4	Temperature °C	Water vapor pressure mmHg
75	60	47
75	80	111
75	100	240
75	135	760
85	80	48.8
85	100	111
85	158	760
105	325	760
102.53	200	86
102.18	250	563
108.52	250	135.5

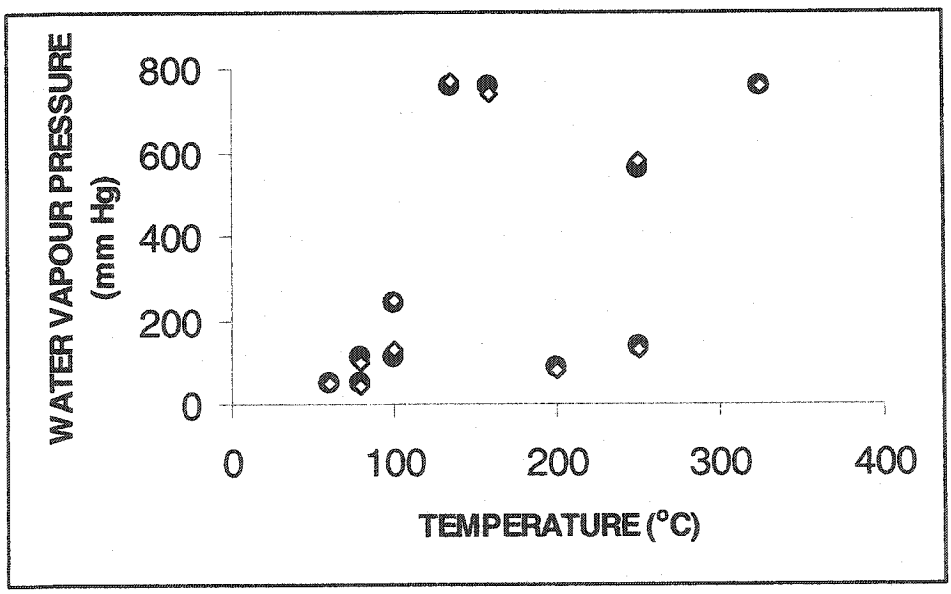

Figure 4.10: Water vapour pressure values corresponding to conditions of Table 4.3; ●: experimental; ◊: calculated using 4.33

The boiling point of phosphoric acid is also important because it determines the maximum operating temperature in the phosphoric acid fuel cell. The following data are reported by Gard (1991) (from the same set of data as for the vapour pressure, corresponding to 760 mmHg):

Table 4.4: Boiling point of phosphoric acid for different solution concentrations

Weight Percentage H_3PO_4	Boiling Point °C
30	101.8
50	108
75	135
85	158
105	325

The data have been fitted with a 3rd-order polynomial:

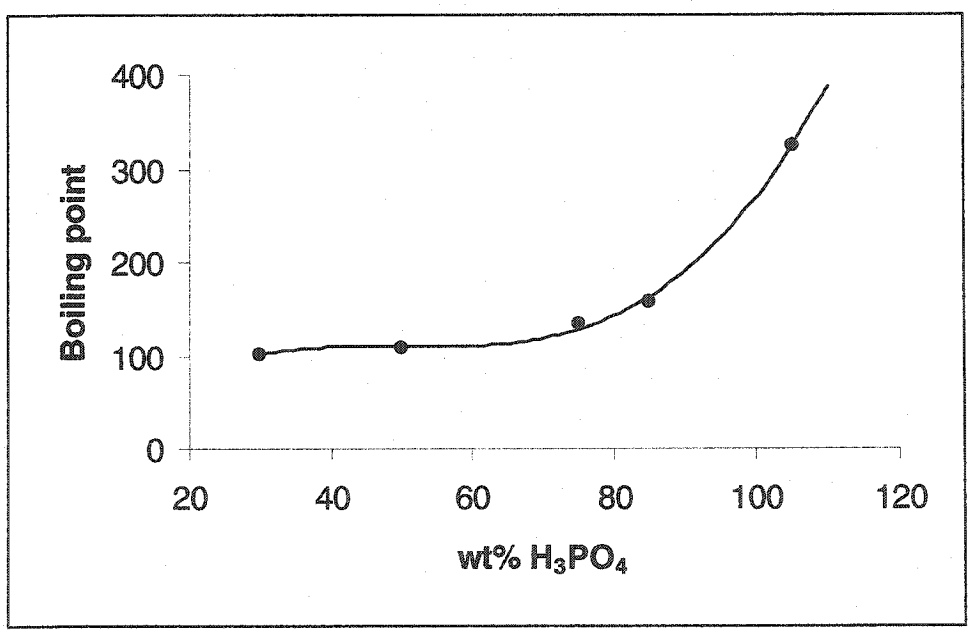

Figure 4.11: Boiling point of phosphoric acid as a function of concentration

The equation of the best-fit line is:

$$T_B = 1.316\times10^{-3}W^3 - 0.1977W^2 + 9.815W - 50.845 \qquad (4.34)$$

4.13 Equilibrium potentials for the reactions

The equilibrium potentials for the anode, cathode and overall reaction are taken to be a function of temperature. The equilibrium potential for the oxygen reduction reaction as a function of temperature was calculated from thermodynamic properties by Scharifker *et al* (1987) as:

$$E_{EQ,CAT} = \frac{-4.184(-70650 - 8T\ln(T) + 92.84T)}{2F} \tag{4.35}$$

The equilibrium potential for the overall reaction at 150°C is reported by Bockris and Srinivasan (1969) to be 1.083 volts and varies only slightly with temperature. The equilibrium potential for the anodic reaction can then be obtained by:

$$E_{EQ,AN} = E_{EQ,CAT} - E_{EQ} \tag{4.36}$$

The effect of pressure on the equilibrium potential for the overall reaction is negligible and is not considered in the model. It is estimated that at the temperatures considered the equilibrium potential changes by 4mv per 10-fold increase in pressure. (Bockris and Srinivasan, 1969).

CHAPTER 5: APPLICATION OF THE MODEL TO A PHOSPHORIC ACID FUEL CELL CATHODE

5.1 Introduction

The mathematical model described in the previous chapters was primarily developed to analyze the performance of direct hydrocarbon fuel cells. However, the model is capable of analyzing the performance of both electrodes of the fuel cell separately. Because of the significance of the cathode phosphoric acid fuel cell electrode in fuel cells operating with other gaseous fuels, such as hydrogen, it was decided to apply this model in order to evaluate its performance separately. Experimentally, it is possible to evaluate the performance of a single electrode in a half-cell apparatus, and several experimental studies have been performed for oxygen and air cathodes. Different sets of data were found in the literature for the performance in air and pure oxygen of two well-characterized electrodes with different properties. These operating conditions and electrode properties were used as input in the cathode mathematical model and the half-cell polarization curves were predicted as described in chapter 3. Two of the model parameters (the exchange current-density and the size of the agglomerates) required to be adjusted in order to fit the experimental data.

Subsequently, several "numerical experiments" were performed in order to gain insight into the operation of the electrode and to quantify the contributions of the various processes that cause voltage losses during operation of the electrode. These processes include the reduction reaction of oxygen on the catalyst, the diffusion of oxygen in the gas phase in the gas diffusion layer and the catalyst layer, the diffusion of oxygen in the liquid films surrounding the agglomerates, the diffusion of oxygen in the micropores in the agglomerates and the ionic conduction through the thickness of the electrode. All of these processes (resistances) have the effect of reducing the electrode potential from its equilibrium value and the potential loss (polarization) is a function of the current density produced in the electrode. The potential loss contributed by polarization of the surface reaction is often referred to as activation overpotential or simply overpotential. The combined effect of all diffusion processes, in this case of oxygen in the gas and liquid phase, is called the concentration polarization. The potential loss caused by ionic conduction is also called the iR-loss or iR-drop.

Another issue of interest in this study was the effect of oxygen conversion in the potential losses. As mentioned before, as air flows in the gas channel of a fuel cell, it is progressively depleted in oxygen. At any position in the gas channel, oxygen will consequently have a different partial pressure or concentration in the cathode gas mixture, corresponding to a different extent of conversion. The one-dimensional model is capable of predicting the effect of the local value of oxygen conversion in the gas channel on the polarization curves and on the potential losses caused by the various processes.

Finally, the model was used to assess the effect of the operating conditions and electrode design parameters on the performance of the electrode. The effects of temperature, phosphoric acid concentration, electrode thickness and platinum loading on the performance of the electrode were considered. Similarly, the effect of some uncertain model parameters on the predictions was assessed. These include the Tafel parameters (exchange current-density and transfer coefficient), the agglomerate size and the liquid-film thickness.

5.2 Comparison of model results with experimental data

The predictions of the mathematical model were compared with experimental data from two different Teflon-bonded gas-diffusion electrodes used as cathodes, published in the open literature. The first set of data (electrode A) is reported by Kunz and Gruver (1975) and the second set of data (electrode B) is reported by Maoka (1988). The electrode properties and operating conditions for the experimental runs that are used for comparison with the model predictions are listed in **Table 5.1**. It is important to note that electrode B contains more platinum but it is thicker than electrode A. The properties shown in the table were used as input variables in the cathode model. The code written for the simulation of electrode B is given in Appendix B1.

The model-predicted and experimental polarization curves for electrodes A and B are shown in **Figures 5.1** and **5.2** respectively. The value for the agglomerates' radii used in the simulation for electrode A was 1 μm and the input for the exchange current at 25°C was 5×10^{-13} amp/cm^2 (with activation energy 92 kJ / mole). The thickness of the liquid films estimated for electrode A by the model was 44 nm. The value for the agglomerates' radii used in the simulation for electrode B was 4 μm and the input for the exchange current at 25°C was 10^{-13} amp/cm^2 (with activation energy 92 kJ/mole). The small difference in the values used for these two parameters for electrodes A and B is physically possible. The values for these two parameters were adjusted in

order to fit the experimental data. The thickness of the liquid film estimated for electrode B by the model was 98 nm. It is interesting to note that Yang (2000) used the values 50 nm and 60 nm for the electrolyte film thickness in simulating two different cathode electrodes. The values calculated here are of the same order of magnitude.

Table 5.1: Electrode properties and operating conditions for electrodes A and B reported in the literature

	Electrode A	Electrode B
Platinum loading	0.25 mg Pt / cm^2	0.63 mg Pt / cm^2
wt% platinum in Pt/C catalyst	15 wt %	5 wt %
wt% PTFE	50 wt %	50 wt %
Catalyst layer thickness	75 μm	200 μm
Gas diffusion layer thickness	200 μm	600 μm
Temperature	160°C	190 °C
H_3PO_4 concentration	96 wt%	105 wt%

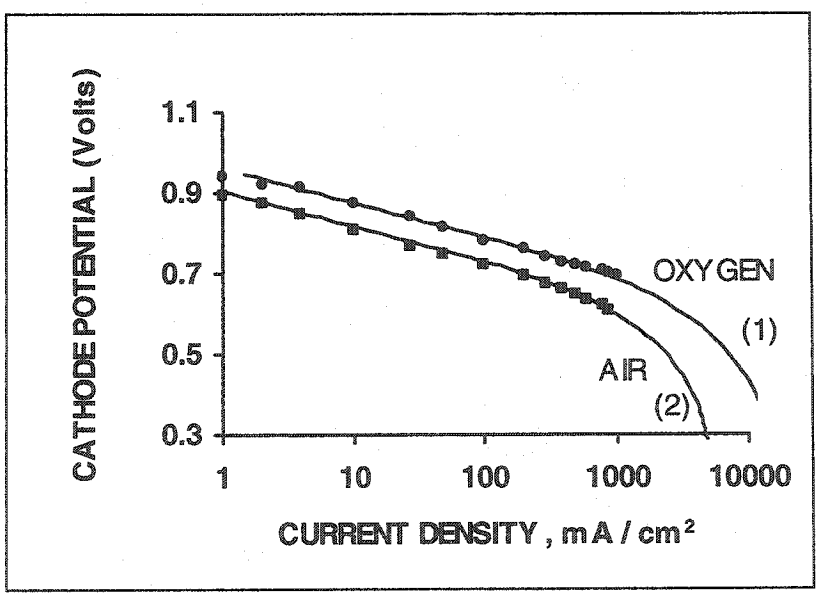

Figure 5.1: Performance curves for electrode A, reported by Kunz and Gruver (1975) and model predictions: ● oxygen, experimental; ■ air, experimental; — (1) oxygen, model; — (2) air, model

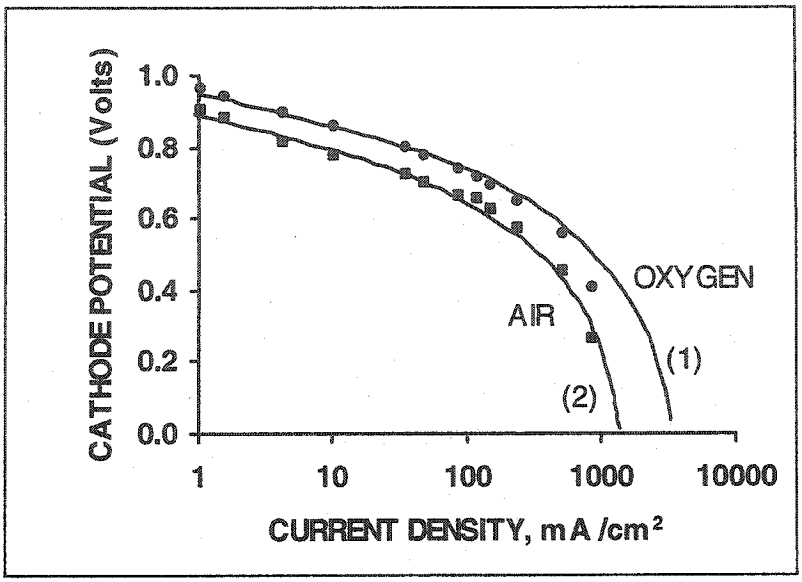

Figure 5.2: Performance curves for electrode B, reported by Maoka (1988) and model predictions: • oxygen, experimental; ■ air, experimental; — (1) oxygen, model; — (2) air, model

The modeling results obtained by using the values for the parameters listed above for both electrodes are in reasonably good agreement with the experimental data for operation in both oxygen and air. The two sets of data correspond to two electrodes of different properties and different performance and therefore the model can capture well the performance-controlling factors for the cathodes. The model can also predict reasonably well the behaviour of the curves for close to current-limiting (high current-density) conditions. Moreover, it is evident from both the experimental data and modeling results that electrode A is performing better over the whole range of currents and exhibits a higher limiting current, although it contains significantly less platinum per cm^2 than electrode B.

5.3 The magnitude of potential-loss contributing processes

The deviation of the cathode potential from its reversible (ideal) value for oxygen reduction is the consequence of several physical processes (resistances) that contribute potential losses at the electrode. These processes are the surface reaction, the various diffusion processes in the electrode and ionic conduction. The present model takes into account the following processes: 1) surface reaction, 2) diffusion of oxygen in the liquid film surrounding each of the agglomerates, 3) diffusion of oxygen in the micropores in the agglomerates, 4) oxygen diffusion in the gas-filled

macropores and 5) ionic (proton) conduction. Using the developed mathematical model it is possible to quantify the effect of each of these processes in order to assess their relative significance in the performance of the cathode. This was done by means of a simulation experiment by forcing the relevant parameters in the model to extremely high values (10^{10}).

In order to predict how the electrode (A or B) would perform if there were no ionic conduction losses, the specific conductivity of the electrolyte was multiplied in the program by a factor of 10^{10}. This eliminated the potential gradient in the electrolyte in the catalyst layer, so that a new polarization curve showing better performance was obtained. Subsequently, in order to predict how the electrode would perform if there were no oxygen diffusion losses in the agglomerates, the effective diffusivity of oxygen in the electrolyte in the agglomerate was multiplied by a factor of 10^{10}. This eliminated the oxygen concentration gradients in the agglomerates, resulting in a polarization curve showing better performance. Subsequently, the effect of diffusion losses in the liquid films was assessed by forcing the oxygen diffusivity in the liquid film to an extremely high value so that the concentration gradient in the liquid film was eliminated. Finally, the effect of oxygen diffusion losses in the gas-pores was assessed by forcing the molecular diffusivities and Knudsen diffusion coefficients to extremely high values so that the concentration gradient in the gas pores disappeared.

In the implementation of this procedure, each of the resistances was progressively eliminated, so that each new polarization curve represents shows the improvement over the previous one, caused by eliminating the effect of one of the processes, in addition to the ones eliminated to obtain the previous line. **Figures 5.3** and **5.4** show the results of this simulation experiment for air performance for electrodes A and B respectively. Line (1) corresponds to the polarization curve predicted with all resistances included. Line (2) was obtained after eliminating the effect of ionic conduction. Line (3) was obtained after eliminating the effects of ionic conduction and oxygen diffusivity inside the agglomerates. Line (4) was obtained after, in addition to the above, the effect of oxygen diffusivity in the liquid films was eliminated. Line (5) was obtained after additional elimination of gas-phase reactant diffusion. A horizontal line through the equilibrium potential for the reaction at the specified temperature corresponds to the ideal reversible potential. An analogous plot was prepared by Bernardi and Verbrugge (1992) for a polymer-electrolyte fuel cell.

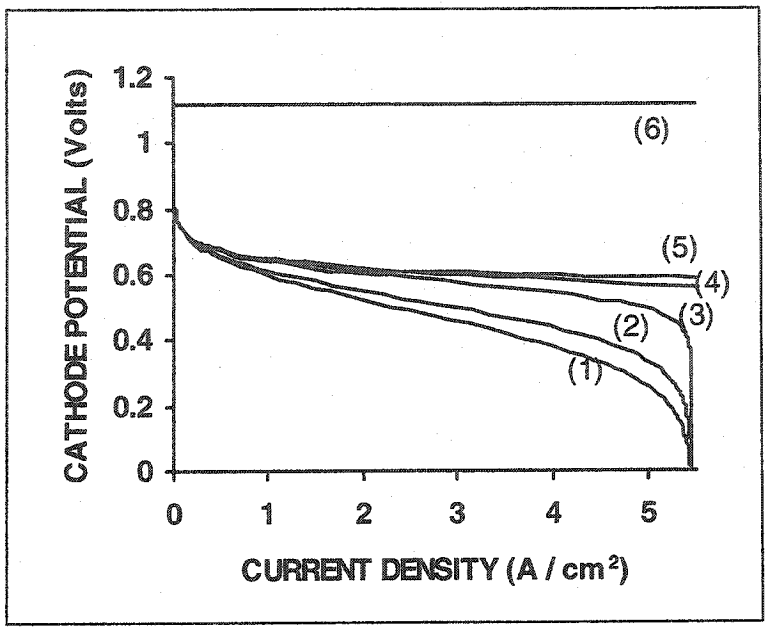

Figure 5.3: Predicted performance curves for electrode A after successive elimination of various resistances: (1) all resistances included; (2) no ionic conduction loss; (3) no diffusion loss in agglomerates; (4) no diffusion loss in liquid films; (5) no diffusion loss in gas phase; (6) equilibrium (ideal) potential

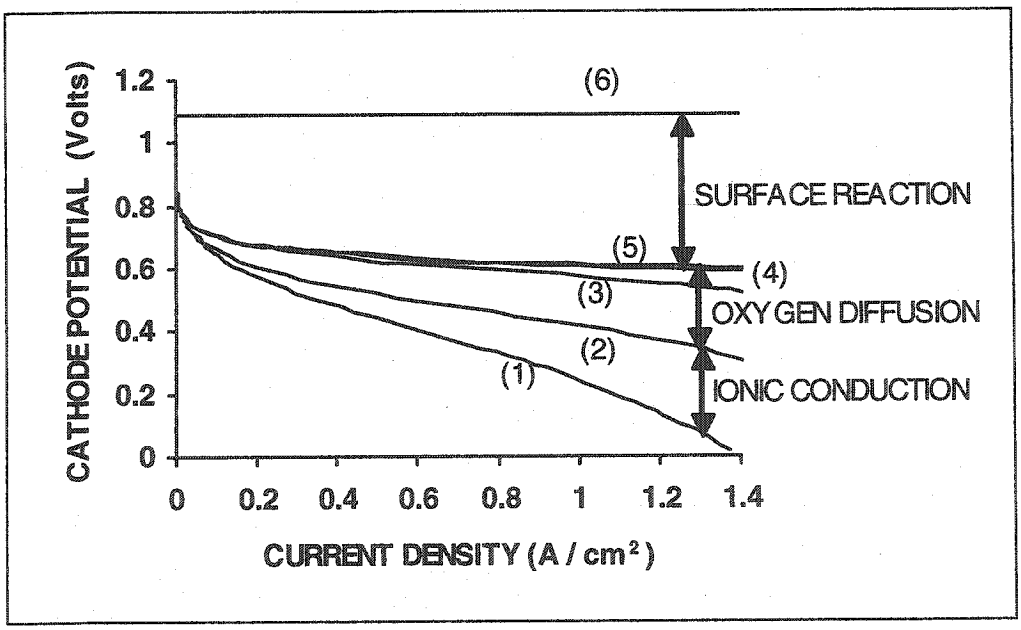

Figure 5.4: Predicted performance curves for electrode B after successive elimination of various resistances: (1) all resistances included; (2) no ionic conduction loss; (3) no diffusion loss in agglomerates; (4) no diffusion loss in liquid films; (5) no diffusion loss in gas phase; (6) equilibrium (ideal) potential

Figures 5.3 and 5.4 convey much information on the effects of the voltage-loss contributions and current-limiting factors for the two electrodes. The vertical distance between any two consecutive lines corresponds to the potential loss contributed by the process eliminated to obtain the upper line. For example, the distance between lines (3) and (4) corresponds to the voltage loss caused by oxygen diffusion through the liquid films surrounding the catalyst agglomerates. The potential loss caused by the major processes is also shown by the arrows in Figure 5.4. As the current density increases, the voltage losses caused by ionic conduction and oxygen diffusion in the liquid are increased, until a point is reached at which the electrode potential drops to zero (at the limiting current). On the basis of the present model, it was also predicted that for both electrodes the potential loss resulting from oxygen diffusion in the gas pores is insignificant.

One of the conclusions that can be derived from the prediction of the small potential loss contributed by the gas diffusion process in the gas-phase is that there is no need to describe this process with the Stefan-Maxwell equations. Due to the complicated form of these equations, considerable numerical difficulty is introduced without any benefit from the improved accuracy of the predictions. The use of the simpler Fick's law with approximate diffusion coefficients would have been sufficient. However, this could not have been assumed prior to the simulation. It could, however, serve as a suggestion for future simulations of the gas diffusion process in fuel cells.

The increase in ionic conduction losses at higher current-densities can be qualitatively explained. As the current-density increases, the reaction rate increases. Since protons are consumed in the oxygen reduction reaction, the rate of proton consumption also increases and, correspondingly, the rate at which protons are supplied from the bulk electrolyte towards the reaction sites inside the catalyst layer also increases. The increase of the ionic current-density requires a larger potential gradient in the electrolyte in the catalyst layer. This means that at increased current-densities, the electrolyte potential at the gas side of the electrode's catalyst layer will be lower (with respect to the electrolyte potential at the bulk electrolyte side) so that the electrode potential drops. Two electrolyte potential distributions across the thickness of the catalyst layer, at different current-densities, produced by the mathematical model, are shown in **Figure 5.5** for operation of electrode B in air, in order to illustrate this point.

It is also evident from **Figure 5.5** that thicker catalyst layers will exhibit larger electrolyte potential distributions, so that the different effect of ionic conduction for electrodes A and B is due to their different thickness. Electrode A is thinner and exhibits a smaller ionic conduction loss.

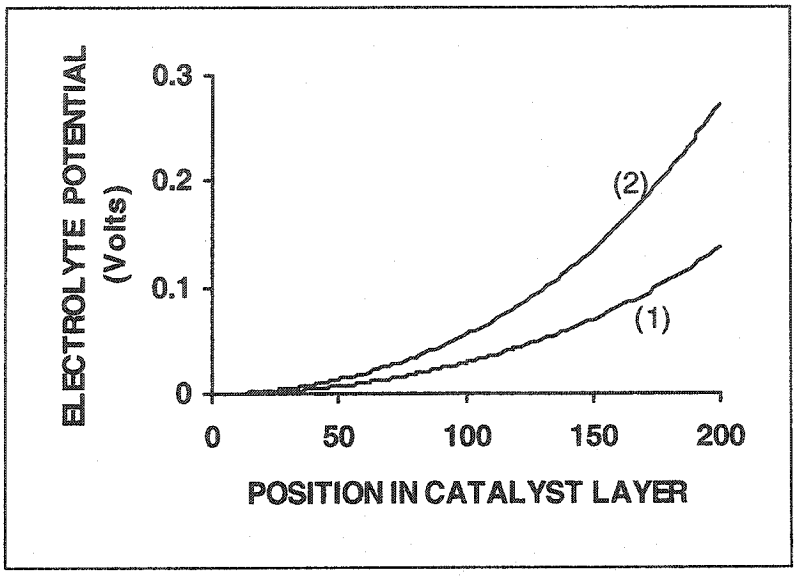

Figure 5.5: Electrical potential distributions in the electrolyte in the catalyst layer for electrode B (position measured from gas diffusion layer boundary); (1) at 0.5 A/cm^2; (2) at 1 A/cm^2

The increase in the potential losses resulting from oxygen diffusion in the agglomerates and their surrounding liquid film can be qualitatively explained. Consumption of oxygen by the reaction inside an agglomerate creates an oxygen concentration distribution in the agglomerate and the liquid film. As the current density is increased, the concentration gradient becomes sharper close to the outside surface and a greater portion of the agglomerate is not well utilized because of the low concentration of dissolved reactant gas in the liquid electrolyte. The lower the oxygen concentration, the higher the polarization (driving force) required to make the reaction proceed at a specific current-density. This is illustrated in **Figure 5.6**, which shows three dissolved oxygen concentration distributions at three different current-densities in an agglomerate positioned close the catalyst layer / bulk electrolyte boundary for electrode A and air feed, as well as in the surrounding liquid film. The distributions were obtained based on the mathematical model.

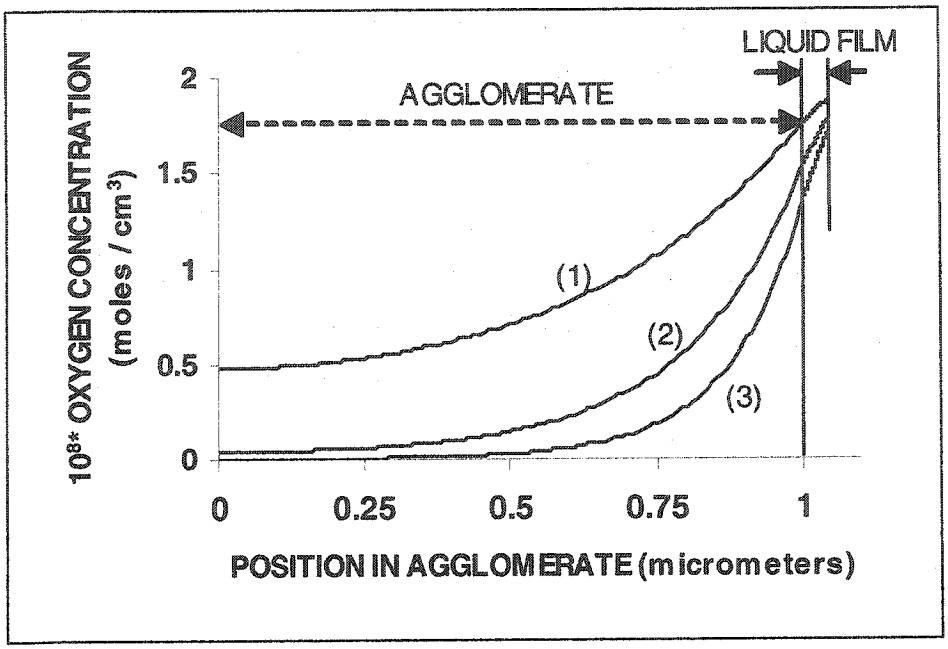

Figure 5.6: Dissolved oxygen concentration distributions in an agglomerate and the surrounding liquid film for electrode A (position measured from agglomerate center); (1) at 0.5 A / cm^2; (2) at 1 A/cm^2; (3) at 1.3 A/cm^2

The larger potential losses associated with oxygen diffusion in electrode B, as compared to electrode A can be explained by the larger values of agglomerate diameter and liquid film thickness taken for electrode B. When the diameter is large, most of the agglomerate is not utilized because the oxygen concentration is small in a large proportion of its thickness. When the liquid film thickness is large, most of the agglomerate is not utilized because of the large concentration drop in the liquid film, where no reaction is happening.

Finally, the small dissolved oxygen concentration difference for the three lines shown in Figure 5.6 at the external surface of the liquid film is the result of oxygen diffusion in the gas pores. As the current-density is increased, more oxygen is consumed, which creates a larger concentration drop in the gas-filled pores through the thickness of the electrode. The reduced dissolved oxygen in the outside surface is due to the equilibrium Henry' law relationship assumed at the boundary of the liquid film. The position of the agglomerate for which the three lines were drawn is at the boundary between the catalyst layer and the gas diffusion layer, where the oxygen concentration in the gas pores has dropped to its minimum value. Nevertheless, as can be seen from Figures 5.3 and 5.4, the potential loss caused by gas-phase oxygen diffusion in the electrode was predicted by this model to be insignificant.

5.4 The effect of the extent of oxygen conversion on the potential losses

The effect of the local oxygen conversion was also predicted using the model. Each local oxygen conversion corresponds to a specific gas phase composition at the external surface of the gas diffusion layer. For example, for air feed to the electrode, 0% conversion corresponds to 0.21 oxygen mole fraction in the bulk gas phase or the gas channel of a fuel cell cathode. Larger conversions correspond to oxygen mole fractions having values that depend on the amount of oxygen consumed and the amount of water in the vapour phase. The one-dimensional model is capable of calculating the local current-density at any cathode potential for any value of local oxygen conversion (gas-phase composition). As the conversion is increased along the gas channel of a fuel cell, the gas is progressively depleted of oxygen, so that the performance should decrease.

One way to illustrate this point is to plot the potential loss as a function of both local current density and local conversion. The potential loss (polarization) is defined as the difference between the equilibrium potential for oxygen reduction and the actual cathode potential. **Figure 5.7** presents the model-predicted contour lines of constant potential losses for electrode B with air feed, as a function of both local current density and local oxygen conversion. The numbers inside the graph show the potential loss in Volts for each contour line.

At any particular value of oxygen conversion, the potential losses increase as the current density increases due to the increasing effect of the various resistances, as discussed before for the zero conversion polarization curve (Figure 5.2 and 5.4). Also, the potential losses increase as the conversion increases for a particular current density because of the oxygen concentration (partial pressure) drop. For example, the limiting (maximum possible) current, corresponding to the line labelled Eeq in Figure 5.7 (for which all of the equilibrium electrode potential has been lost), is decreasing as the conversion increases, clearly showing the significant decrease in performance at high reactant conversions. The practical implication in a fuel cell is that a cathode electrode would be expected to perform significantly worse at locations away from the cathode gas channel inlet where much of the oxygen has been converted by the reduction reaction.

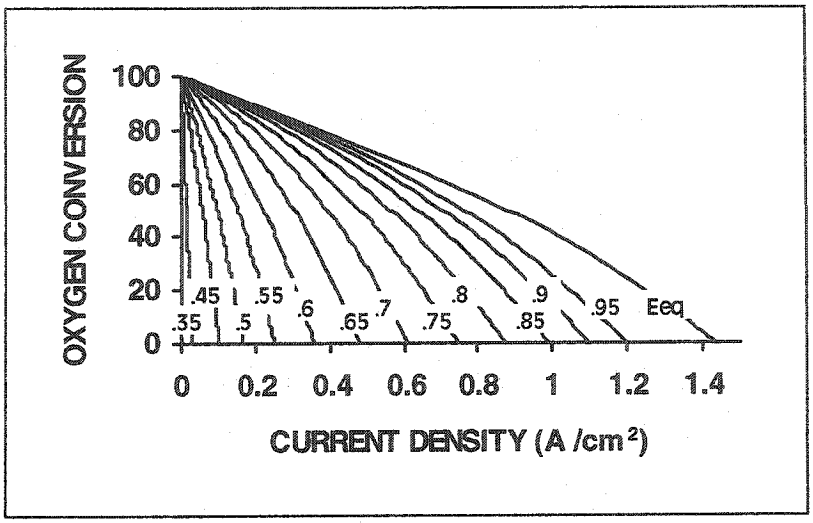

Figure 5.7: Model predictions of contour lines for constant loss of electrical potential (volts) as a function of both local oxygen conversion (%) and local current density (A/cm^2)

In a fuel cell cathode, the net current-density measured would be the integral of the local current densities from the inlet (zero conversion) to the exit of the oxygen channel. At steady-state operation, the cathode catalyst layer will be at constant electrical potential. In order to predict the net current density for a specific cathode electrode potential (or specific value of potential losses), the integration would have to be performed along one of the contour lines of Figure 5.7, from zero conversion to the conversion at the exit.

These consideration lead to the question of how the extent of oxygen conversion affects each of the various resistances that cause potential losses. For this reason we used the developed model to examine what fraction of the total potential loss was caused by each of the processes discussed in the previous section at different values of oxygen conversion and current-density. The results correspond to operation of electrode B in air.

Figure 5.8 presents contour lines of constant percentage of potential loss contributed by the electrochemical reaction (activation or surface overpotential) as a function of oxygen conversion and current density. The numbers inside the graph denote the percentage of the total loss contributed by the surface overpotential for each line. A similar contour map was made for all other resistances: the ionic conduction potential loss (**Figure 5.9**), the potential loss attributed to oxygen diffusion in the agglomerate (**Figure 5.10**), the potential loss attributed to oxygen diffusion in the liquid films (**Figure 5.11**) and the potential loss attributed to oxygen diffusion in the gas phase (**Figure 5.12**). In all cases, the number label of each contour line denotes the

percentage of the total potential loss contributed by the specific resistance described. The processes described by Figures 5.10, 5.11 and 5.12 are all different modes of the electrode's concentration polarization.

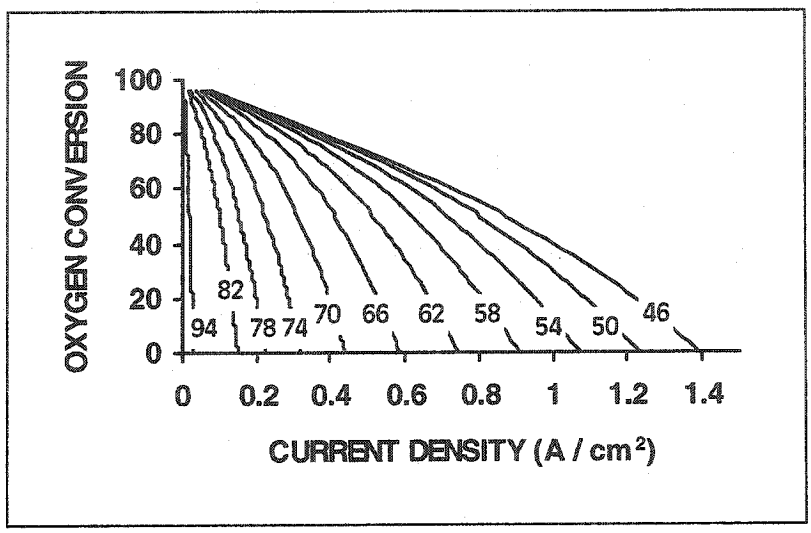

Figure 5.8: Model predictions for contour lines of constant percent of electrical potential loss caused by cathode overpotential (surface polarization) as a function of local oxygen conversion (%) and local current density (A/cm^2)

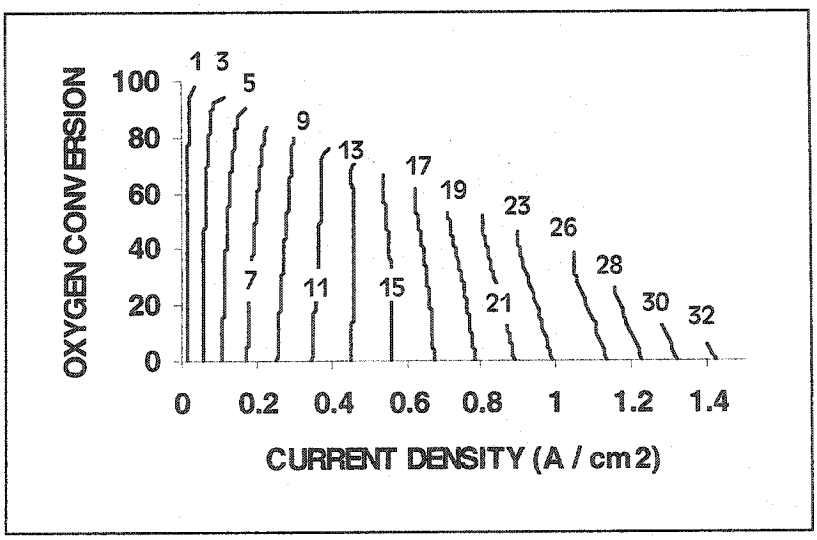

Figure 5.9: Model predictions for contour lines of constant percent of electrical potential loss caused by ionic conduction (ohmic polarization) as a function of local oxygen conversion (%) and local current density (A/cm^2)

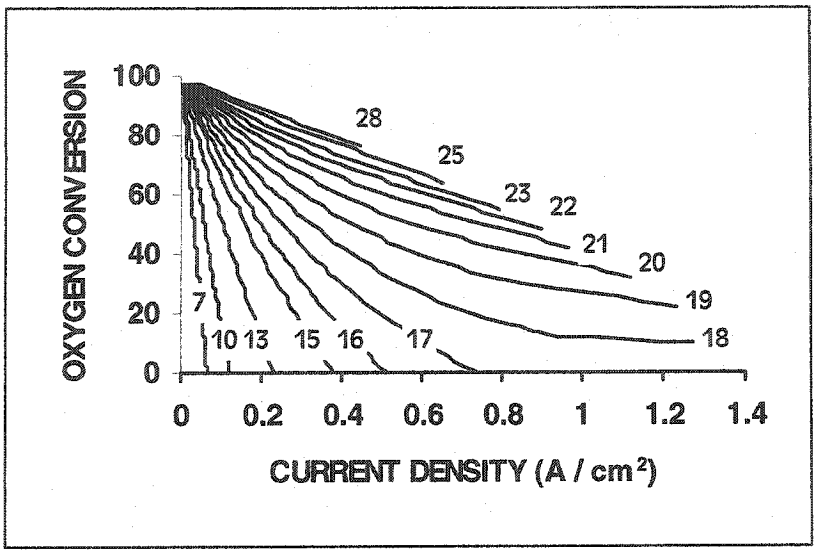

Figure 5.10: Model predictions for contour lines of constant percent of electrical potential loss caused by oxygen diffusion in the agglomerates as a function of local oxygen conversion (%) and local current density (A/cm^2)

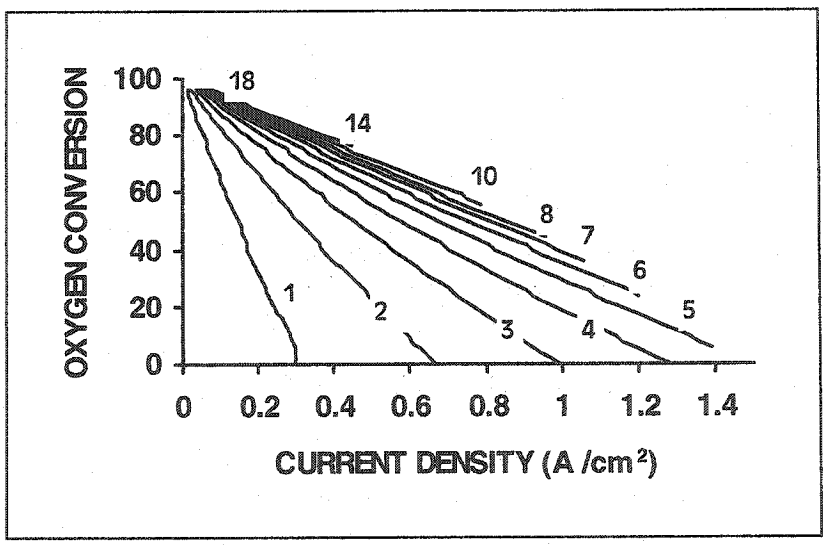

Figure 5.11: Model predictions for contour lines of constant percent of electrical potential loss caused by oxygen diffusion in the liquid film surrounding the agglomerates as a function of local oxygen conversion (%) and local current density (A/cm^2)

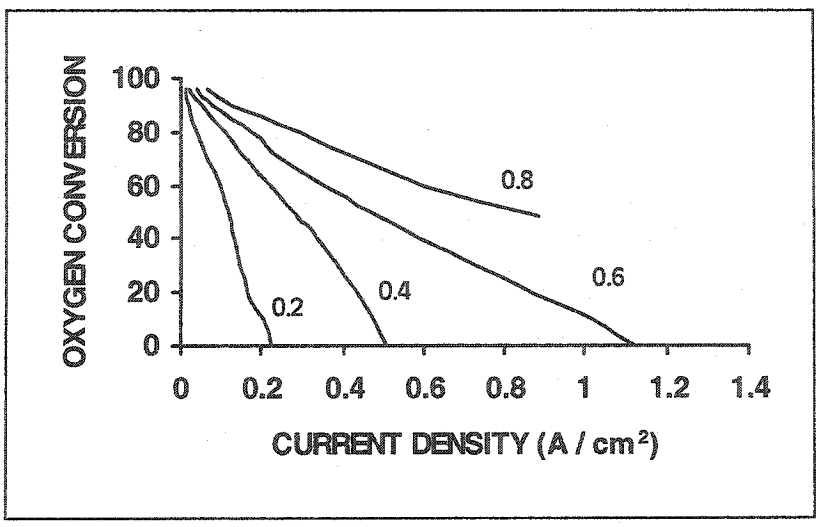

Figure 5.12: Model predictions for contour lines of constant percent of electrical potential loss caused by oxygen diffusion in the gas phase in the catalyst layer and the gas diffusion layer as a function of local oxygen conversion (%) and local current density (A/cm^2)

As shown in Figure 5.8, at low current-densities the surface reaction contributes the greatest proportion of the loss. At any particular conversion, as the current-density is increased all other processes (Figures 5.9-5.12) become increasingly important. The effect of the current-density on all the resistances was described in the precious section. The same explanations hold at any value of oxygen conversion.

The effect of the extent of oxygen conversion can be explained with similar arguments. At any particular current-density, as the oxygen conversion increases, all modes of concentration polarization increase in magnitude (Figures 5.9-5.12). As the gas entering the electrode becomes less concentrated in oxygen the polarization (potential loss) required for the reaction to proceed at any current density becomes greater and the concentration distributions in the agglomerates, the liquid film and the gas pores become increasingly significant. The percentage of the loss contributed by ionic conduction is fairly independent on conversion (Figure 5.9). The ionic conduction is an iR-drop and therefore depends strongly on the current density. The small dependence on conversion is because the current-density distribution through the thickness of the catalyst layer is also affected by conversion and the iR-drop inside the electrode is a distributed quantity because the ionic current density is variable across the thickness of the electrode. As a consequence of the increased percentage of concentration polarization losses at high oxygen conversions, the percentage of the potential loss contributed by the surface polarization is decreased with increasing the extent of conversion (Figure 5.8).

The combination of Figures 5.7 to 5.12 can be used to determine which processes are more significant at any current-density and oxygen conversion. For example, at 0.6 A/cm^2 and 40% conversion, the total potential loss is 0.77 Volts (Figure 5.7). 61% of that is attributed to the surface overpotential (Figure 5.8), 16% to ohmic polarization (Figure 5.9) and 23% to concentration polarization (Figures 5.10-5.12). These values are strongly dependent on current-density, conversion and the characteristics of the electrode (catalyst layer thickness, phosphoric acid concentration, catalyst composition, microstructure etc.). As a practical implication, the design of any cathode electrode should be optimized with respect to the operating conditions (current-density and oxygen conversion).

It should be noted that the only analysis similar to the one provided in this section to be found in the literature was provided by Yang *et al* (1990), based on a model that included the same physical phenomena as the present model. In that model (Yang *et al*, 2001), six model parameters were adjusted to fit experimental data. Their results on the relative contributions of potential losses are presented for 5 different current densities at zero oxygen conversion (i.e. half-cell) and for one current-density at two different conversions (i.e. fuel cell cathode). Their results agree qualitatively with these from the present model. The quantitative differences are attributed to the fact that different electrodes are modeled in the present work compared with the electrode modeled in the work of Yang *et al* (2001). Furthermore, the parameters obtained by optimization are not the same as those used in the present work. Nevertheless, the quantitative agreement is also good. The results of Yang *et al* also indicate that the potential loss contributions in the electrode he modeled, in order of decreasing magnitude, are the i) the surface polarization, ii) ionic conduction in the electrode and iii) oxygen diffusion in the liquid. Nevertheless, the present results provide a much more complete picture of the effects of current-density and conversion by considering the whole range of their variation, including operation at close to limiting currents. Furthermore, it can be concluded from both the present results and those of Yang *et al*, that the gas-phase oxygen diffusion contributes a very small part of the concentration overpotential (less than 2%). Both results indicate that it is justifiable to neglect gas-diffusion phenomena in the electrode's gas-filled pores, in order to simplify the mathematical treatment (for example, as in the model by Perry *et al*, 1998).

5.5 The effect of operating conditions and electrode design parameters

In this section the effect of the operating condition and electrode design parameters, as predicted by the mathematical model, is considered. These parameters include the effect of temperature, gas pressure, phosphoric acid concentration, catalyst composition (weight percentage of platinum on carbon) and catalyst layer thickness. It was chosen to simulate the effects of these parameters on the operation of electrode B in air in order to illustrate the predicted trends.

The predicted effect of the operating temperature on the performance of the electrode is illustrated in **Figure 5.13**. The value for the activation energy for the reaction used to produce this graph was reported in Section 4.1 as 92 kJ / mole. As the temperature is increased, the cathode performance is enhanced because all types of polarization are decreased. Operation at increased temperature results in larger surface reaction rate (lower surface polarization) because the exchange current-density is increased. It also results in lower concentration polarization losses because the diffusivity of oxygen is increased and in lower ohmic polarization losses because the conductivity of phosphoric acid is increased. Thus, the increase in temperature reduces all resistances. In practice, the upper temperature limit for a phosphoric acid fuel cell cathode is determined by the boiling point of the acid, which depends on its concentration. More concentrated solutions allow operation at higher temperatures.

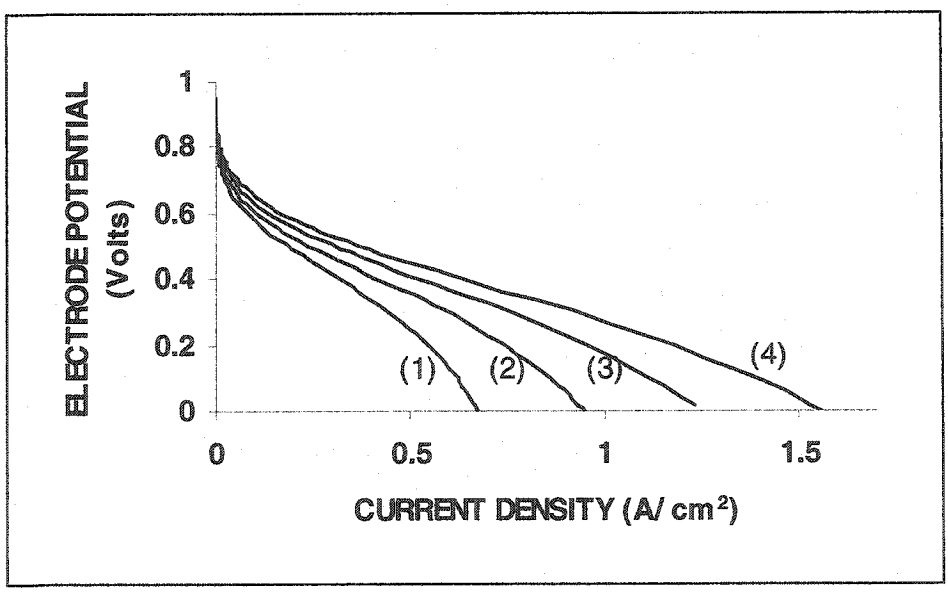

Figure 5.13: Model predictions of polarization curves at different operating temperatures for electrode B, air feed; (1) 125°C; (2) 150°C; (3) 175°C; (4) 200°C

The predicted effect of increasing the air feed pressure on electrode B is shown in **Figure 5.14**. As the air pressure is increased, the electrode performance is enhanced. The increased electrode potential is caused by the increased oxygen concentration at higher pressures, which causes an increase in the surface reaction rate and also decreases the concentration overpotential. Practically, in a fuel cell cathode, the better performance resulting from elevated gas pressures comes at the expense of pressurizing the air so that optimization becomes an important issue.

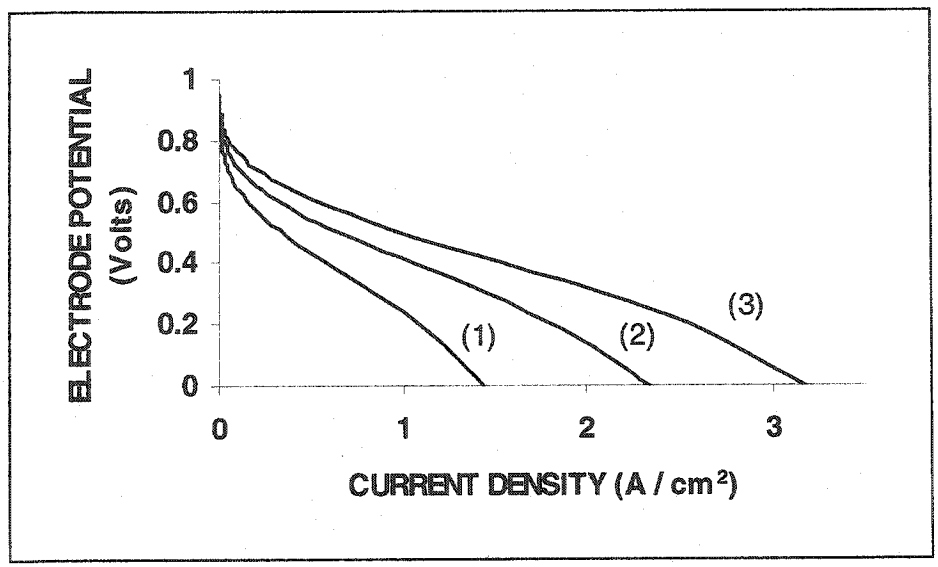

Figure 5.14: Model predictions of polarization curves at different gas pressures for electrode B, air feed; (1) 1 atm; (2) 3 atm; (3) 7 atm

The effect of the concentration of phosphoric acid on the performance of the cathode was also considered. At any phosphoric acid concentration, the maximum permissible temperature is determined by the boiling point of phosphoric acid. The operating temperature of electrode B was 190°C, which corresponds to the boiling point of ~91wt % H_3PO_4. At this temperature, any acid concentration lower than 91%, could not be used. In order to examine a slightly wider range of phosphoric acid concentrations, the model for electrode A was used. The predicted effect of phosphoric acid concentration on the performance of electrode A with air feed at a constant temperature of 160°C is shown in **Figure 5.15**. At constant temperature, the model predicted that the performance drops as the phosphoric acid concentration is increased. At higher phosphoric acid concentrations, the diffusivity of oxygen in the electrolyte is reduced and the specific conductivity of the electrolyte is also reduced, so that both the ohmic and the concentration polarization are increased. This explains the consequential decrease in performance.

However, the use of higher phosphoric acid concentrations permits operation of the electrode at higher temperatures because of the lower water vapour pressure. In order to examine the effect of changing both parameters simultaneously, polarization curves at constant water vapour pressure were produced using the model. **Figure 5.16** presents the predicted performance of electrode A with air feed at constant water vapour of 0.9 atm, resulting from different combinations of temperature and H_3PO_4 concentration. The four lines are hardly distinguishable. The model predicts that the effect of temperature almost exactly offsets the effect of phosphoric acid concentration. As the temperature is increased, the reaction rate increases, the diffusivity of oxygen in the electrolyte increases and the specific conductivity of the acid increases, so that all types of polarization are reduced.

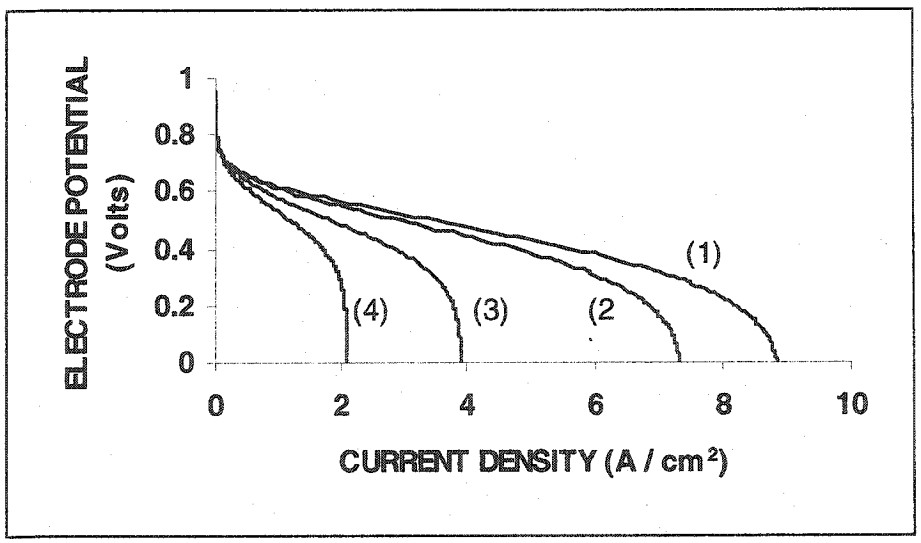

Figure 5.15: Model predictions of polarization curves for different phosphoric acid concentrations at constant operating temperature (160°C) for electrode A, air feed; (1) 85% H_3PO_4; (2) 90% H_3PO_4; (3) 100% H_3PO_4; (4) 105% H_3PO_4

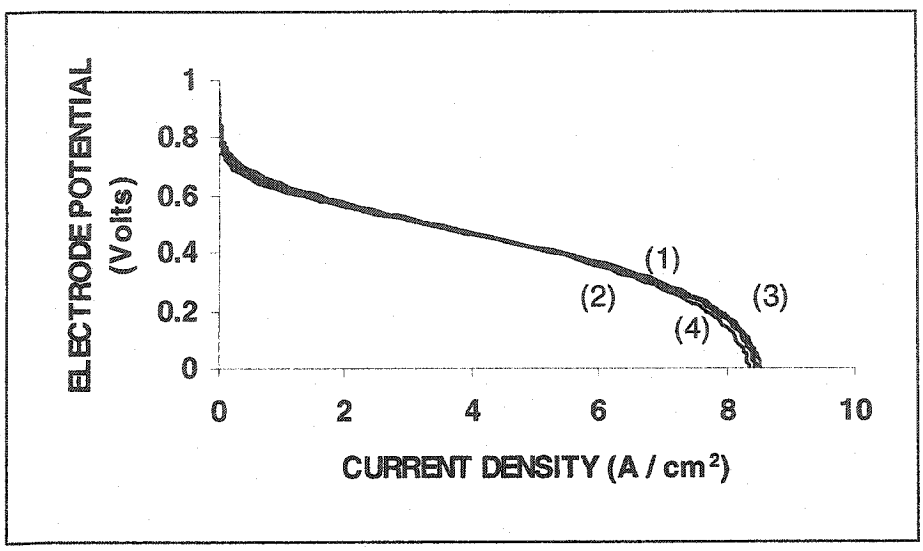

Figure 5.16: Model predictions of polarization curves for different combinations of phosphoric acid concentration and operating temperature resulting in same water vapour pressure (0.9 atm) for electrode A, air feed; (1) 85% H_3PO_4, 155°C; (2) 90% H_3PO, 176°C $_4$; (3) 100% H_3PO_4, 205°C; (4) 105% H_3PO_4, 240°C

The effect of changing the platinum loading of the electrode, produced by changing the concentration of platinum in the catalyst, was also predicted using the present model. The results are shown in **Figure 5.17** for electrodes A and B performance at a constant potential of 0.7V and 0.6V respectively, at which experimental data are available. The modeling results indicate that, for the intermediate potentials considered, the increase in performance due to increased platinum loading tends to be lower at higher platinum loadings. The experimental data indicate the same trend. As the weight percentage of platinum in the platinum/carbon catalyst is increased, the size of the platinum particles increases, the surface area of platinum that is available for reaction decreases, so that part of the performance increase associated with using more platinum is sacrificed. It is interesting to note that current PAFC's usually contain 0.5 mg Pt / cm^2 in the cathode (Hirschenhofer *et al*, 1998).

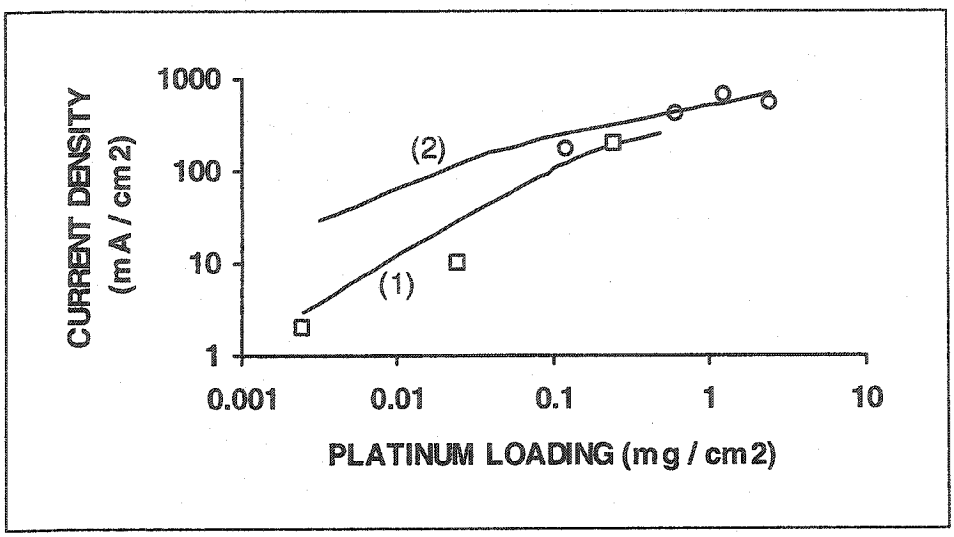

Figure 5.17: Effect of platinum loading (catalyst composition) on electrode performance: (1) electrode A, air, 0.7V, model; ف electrode A, air, 0.7V, experimental; (2) electrode B, oxygen, 0.6V, model; o electrode B, oxygen, 0.6V, experimental.

Another way of changing the platinum content of the electrode is by changing the thickness of the catalyst layer for the same concentration of platinum on carbon catalyst. **Figure 5.18** presents the model predicted polarization curves for different electrode catalyst layer thicknesses for conditions corresponding to electrode B (air operation). The platinum loading corresponding to each line is proportional to the catalyst layer thickness. The figure shows the increase in performance caused by the increased amount of platinum in a thicker catalyst layer levels-off above a critical thickness that is dependent on the current density. At low potentials the performance of the thicker electrode even drops. These results can be qualitatively explained: as the catalyst layer thickness increases, the ohmic polarization increases. Also, the effect is more dramatic at high current-densities, at which the contribution of ohmic polarization losses is more significant.

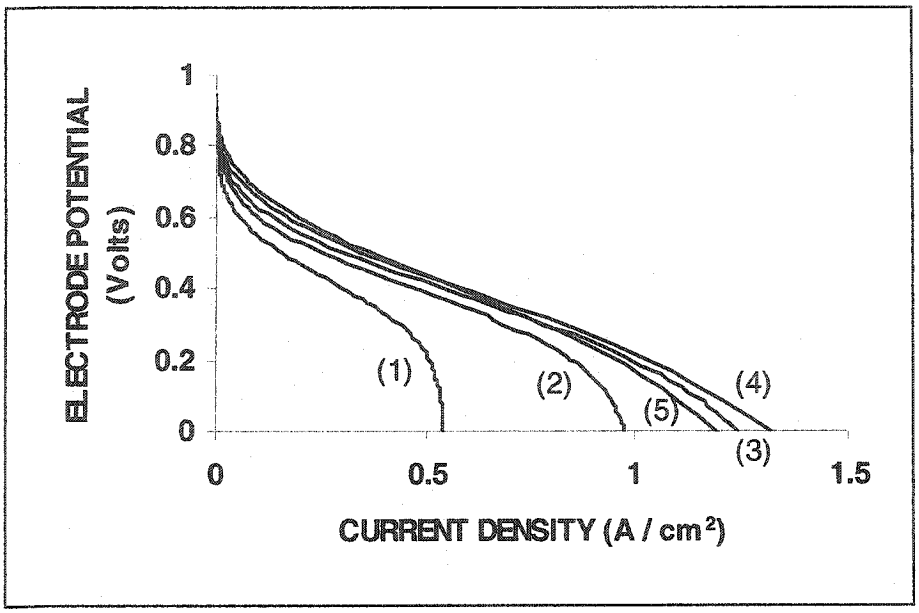

Figure 5.18: Polarization curves predicted by the model for different thicknesses of the electrode's catalyst layer (different platinum loading) for operation of electrode B in air. Catalyst layer thickness = (1) 50μm; (2) 100μm; (3) 150μm; (4) 250μm; (5) 450μm

5.6 The effect of some electrochemical and physicochemical model parameters (Sensitivity analysis)

The results of the cathode mathematical model presented until now are based on specific values of the various electrochemical and physicochemical parameters required. As mentioned earlier, the uncertainties associated with the values of many of these parameters can be quite large. For this reason, it is interesting to examine to what extent some of these variables affect the cathode performance in order to gain some insight of their relative importance. Of particular interest is the exchange current-density for oxygen reduction, the cathodic transfer coefficient for the reaction, the size of the catalyst agglomerates and the thickness of the liquid film, the effective diffusivity of dissolved oxygen in the catalyst layer's liquid-filled pores, the solubility of oxygen in the electrolyte and the effective specific conductivity of the electrolyte in the porous catalyst layer structure. As a base-case condition for this analysis, the values used for these parameters or calculated by the model equations for the simulation of electrode B (air feed), will be used. These values are presented in **Table 5.2** and were calculated for the specific conditions of this electrode (temperature, acid concentration).

Table 5.2: Physicochemical and electrochemical parameters used or calculated for electrode B

Parameter	Value
Exchange current density	5.63×10^{-8} A/cm^2
Cathodic transfer coefficient	1
Agglomerate's radius	4μm
Liquid film thickness	98 nm
Effective oxygen diffusivity in H_3PO_4 in catalyst layer	1.94×10^{-5} cm^2/s
Oxygen solubility in electrolyte	9.41×10^{-8} moles/cm^{3}atm
Effective electrolyte conductivity In catalyst layer	0.029 S/cm

The purpose of this analysis is not only to illustrate the effect of the possible uncertainty in the values of these parameters. It is common for fuel cell electrodes to exhibit very large performance variations when they are different in some respect, for example for electrodes with different electrolyte, catalyst or electrodes prepared in a different manner. This analysis can be useful in understanding the effect of such important differences between electrodes. For example, changing the electrolyte will change the specific conductivity, oxygen solubility and dissolved oxygen diffusivity. Changing the catalyst will affect the exchange current density and transfer coefficient. Electrodes prepared in different ways will be characterized by a different microscopic structure, so that the effective values of the agglomerates or liquid film can be substantially different. The same difference is true between a new electrode and an electrode that has been operating for very long. Taking this into account, the range of variation of the variables presented in Table 5.2 that was used for the analysis of this section is considerably larger than the possible uncertainty of the values that were used for the simulation of the specific electrode. Polarization curves for different values of each of these variables appear are presented in **Figures 5.19- 5.25**.

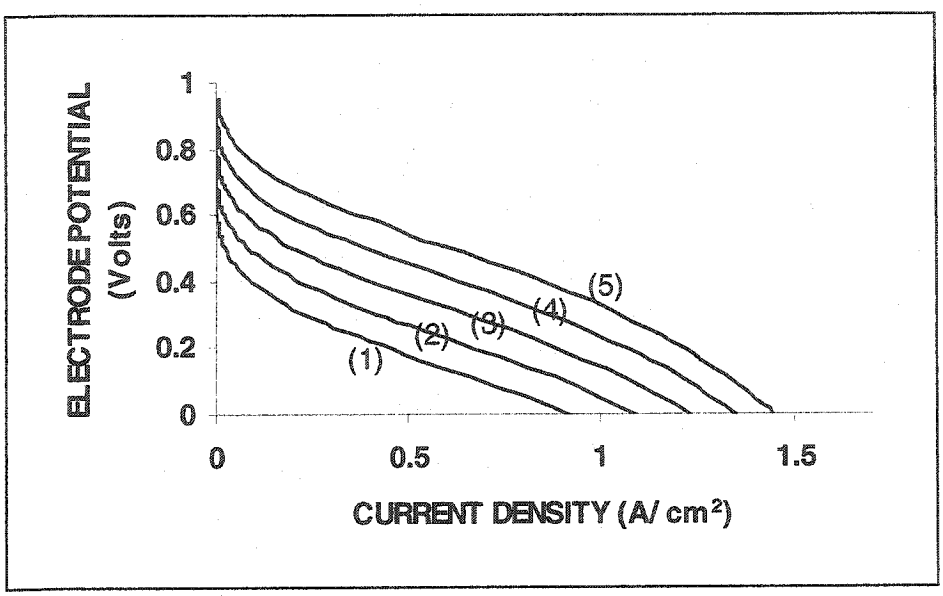

Figure 5.19: Effect of exchange current density for oxygen reduction on electrode performance. Conditions correspond to electrode B; (1) 10^{-10} A /cm^2; (2) 10^{-9} A /cm^2; (3) 10^{-8} A /cm^2; (4) 10^{-7} A /cm^2; (5) 10^{-6} A /cm^2

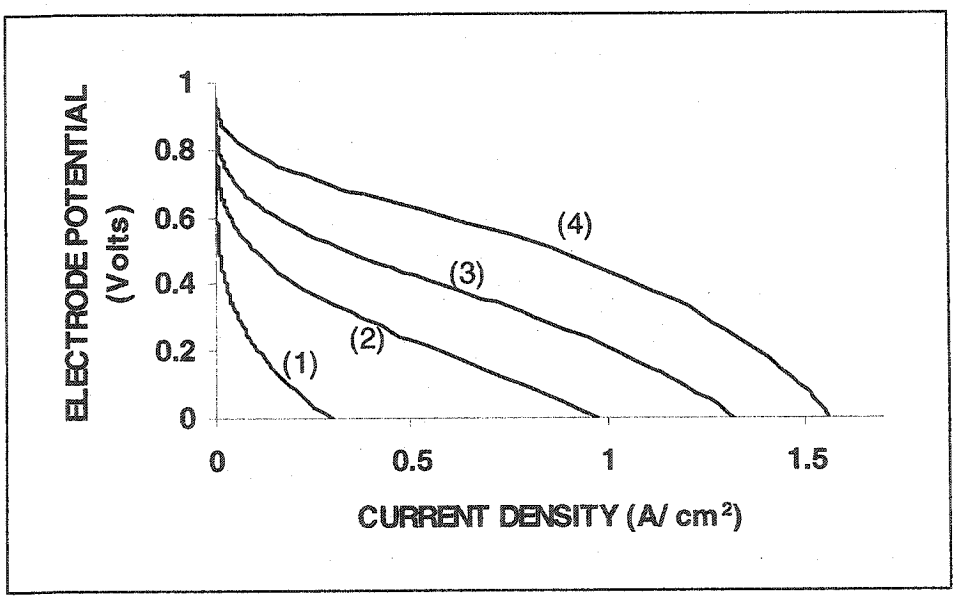

Figure 5.20: Effect of cathodic transfer coefficient for oxygen reduction on electrode performance. Conditions correspond to electrode B; (1) a = 0.5; (2) a = 0.75; (3) a = 1; (4) a = 1.5

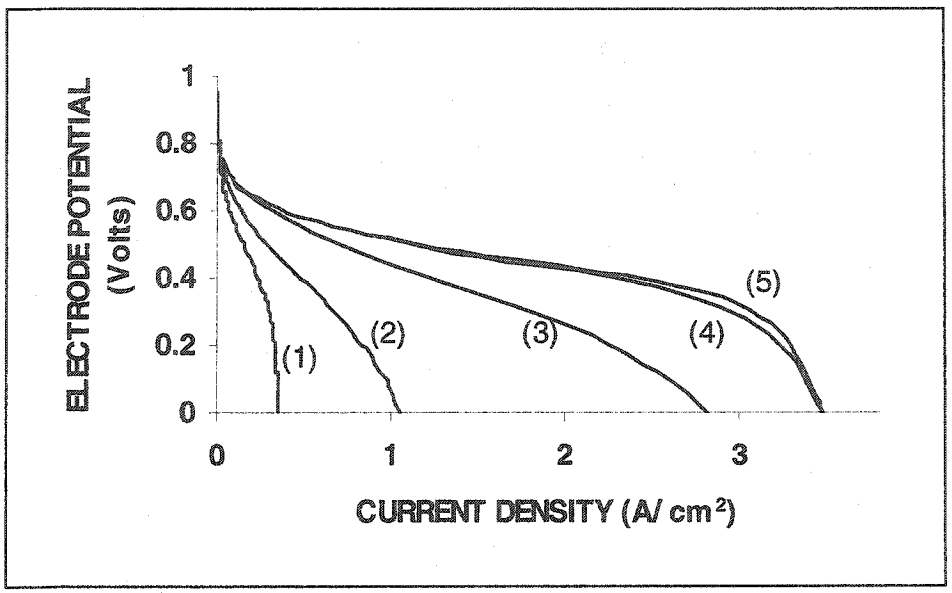

Figure 5.21: Effect of agglomerate's radius on electrode performance. Conditions correspond to electrode B; (1) Ra = 10 μm; (2) Ra = 5 μm; (3) Ra = 1 μm; (4) Ra = 0.1 μm; (5) Ra = 0.05 μm;

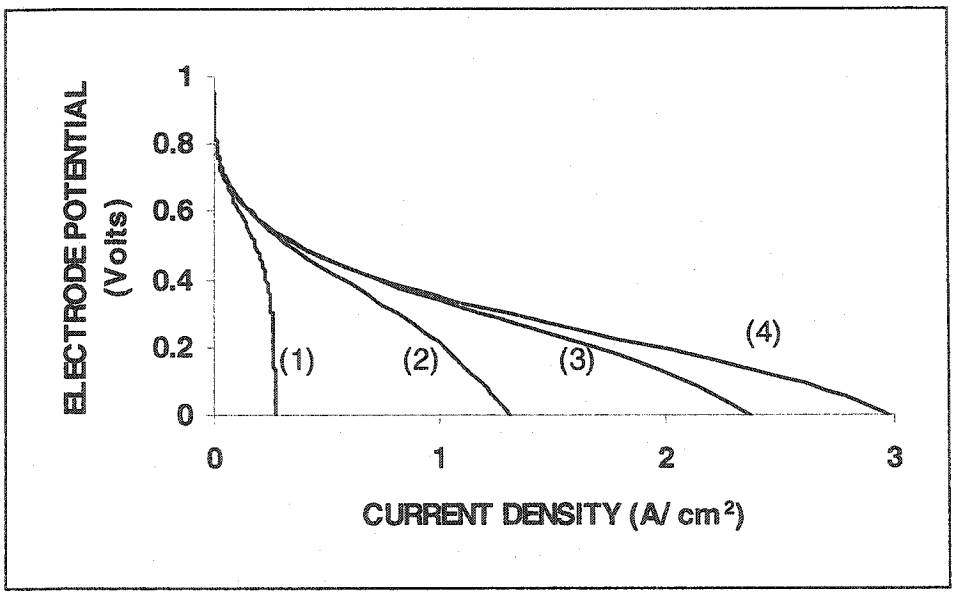

Figure 5.22: Effect of liquid film thickness (Lf) on electrode performance. Conditions correspond to electrode B; (1) Lf = 1 μm; (2) Lf = 100 nm; (3) Lf = 10 nm; (4) Lf = 1 nm

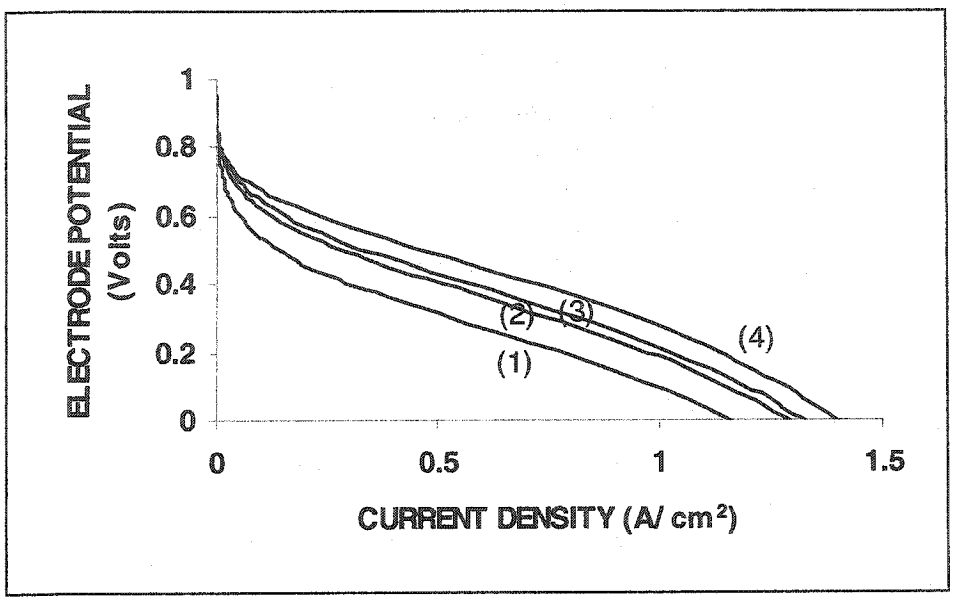

Figure 5.23: Effect of oxygen effective diffusion coefficient Do in the electrolyte-filled pores of the catalyst layer; (1) Do = 10^{-6} cm^2/s; (2) Do = 10^{-5} cm^2/s; (3) Do = $2*10^{-5}$ cm^2/s; (4) Do = 10^{-4} cm^2/s

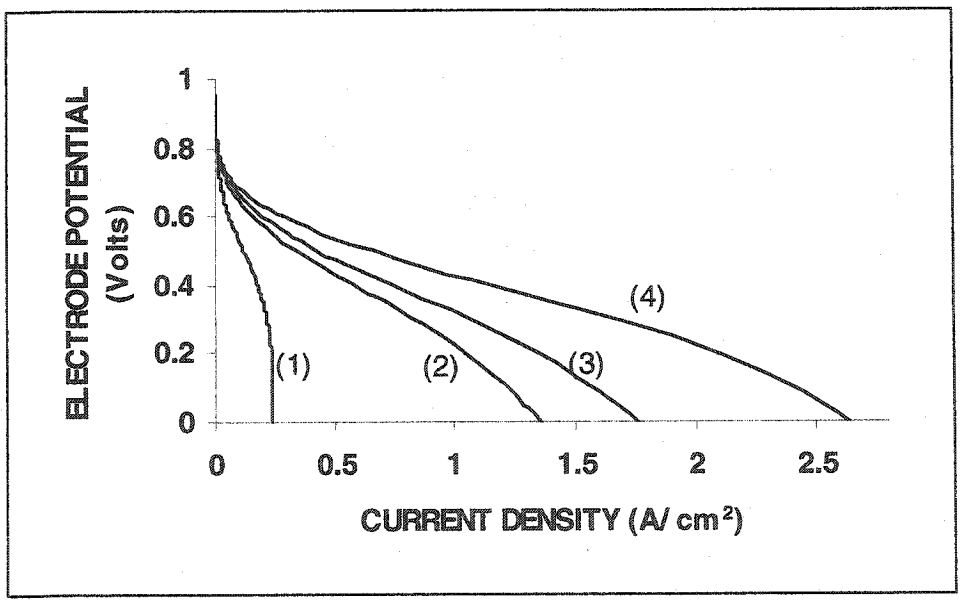

Figure 5.24: Effect of oxygen solubility c* in the electrolyte on the performance of electrode B; (1) c* = 10^{-8} moles /cm^3atm; (2) c* = 10^{-7} moles /cm^3atm; (3) c* = $2*10^{-7}$ moles /cm^3atm; (4) c* = 10^{-6} moles /cm^3atm

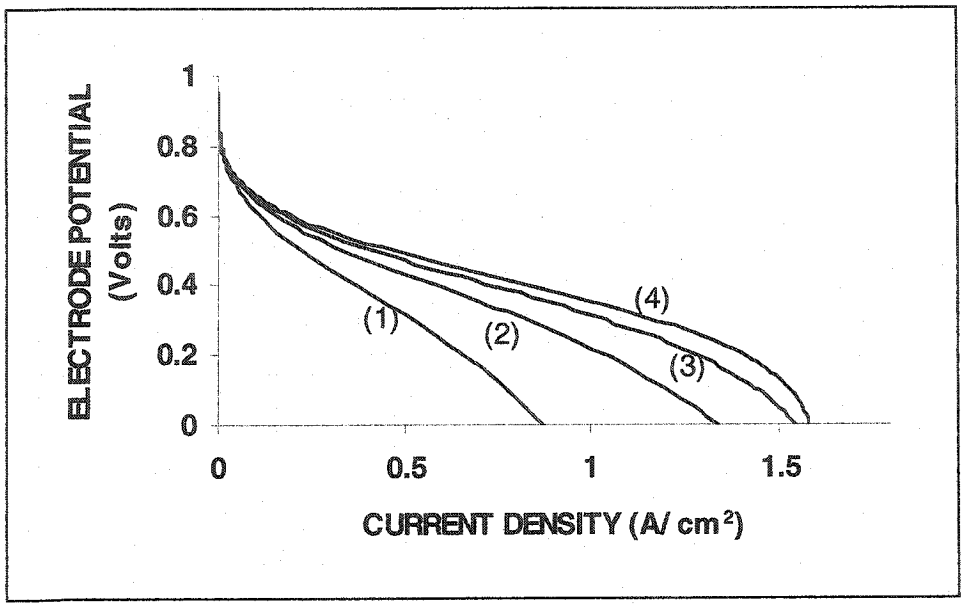

Figure 5.25: Effect of the effective electrolyte's specific conductivity on the performance of electrode B; (1) 0.01 S/cm (2) 0.03 S/cm; (3) 0.06 S/cm; (4) 0.1S/cm

Figures 5.19-5.25 show that all of the parameters considered have a significant effect on the predicted performance of the electrode. As expected, the performance is improved with larger exchange current-density and transfer coefficient for the electrochemical reaction, with smaller agglomerates and liquid film thicknesses and with larger oxygen diffusivity and solubility in the electrolyte and electrolyte conductivity. The figures presented here can give some insight into what extent an order of magnitude change in the values of these parameters affects the performance. The effects of the agglomerate size and the solubility of oxygen in the electrolyte are particularly significant. It has been observed that the severe deterioration in performance for long operating times of fuel cell electrodes is, at least partly, owing to the agglomeration process of the catalyst. Also, one of the important characteristics of a fuel cell electrolyte is its ability to dissolve oxygen (as well as the fuel in the anode). The effect of the reaction parameters (exchange current and transfer coefficient) is also significant. Different catalysts used for the oxygen reduction reaction exhibit different values of these parameters. In short, the choice of catalyst, electrolyte and the specific design of a fuel cell cathode can result in very different values of all the parameters studied in this section.

CHAPTER 6: APPLICATION OF THE MODEL TO A DIRECT PROPANE FUEL CELL

6.1 Introduction

The results of the application of the mathematical model to a direct propane fuel cell are presented in this chapter. Separate programmes were written to describe the performance of the anode and the cathode of the cell. The method used to obtain the cell polarization curves from the individual electrode polarization curves was described in Chapter 3. In this chapter only the model results are discussed. The predicted effect of several operating conditions and electrode structure parameters is also presented. These parameters include the cell operating temperature, the pressure of the gases in the anode and cathode gas channels, the concentration of the phosphoric acid electrolyte and the platinum loadings and catalyst layer thicknesses of the two electrodes. Power density and fuel efficiency curves were also simulated.

Experimental data on the performance of direct propane phosphoric acid fuel cells have been published by Grubb and Michalske (1964). These electrodes were chosen in order to compare the model predictions with available data. The data have been published nearly 40 years ago. Although the unit cells used in these experiments have been greatly improved since then, the authors provide a good description of the electrodes and consider the effect of various parameters that affect the performance, particularly the operating temperature and the concentration of phosphoric acid. These data provide the opportunity to verify the model developed in this work.

Since the time these experiments were performed, the structure of gas-diffusion electrodes and unit cells has been improved. The improvements have resulted from intense research on fuel cells operating on hydrogen. Some performance improvement in direct hydrocarbon fuel cells should also be evident because the same cathode electrode is used for both hydrocarbon and hydrogen fuel. Moreover, a comparison between carbon black electrodes used in the experiments mentioned before (for direct propane/ oxygen cells) and a modern gas-diffusion electrode designed for hydrogen phosphoric acid fuel cells and utilizing platinum dispersed on carbon as the electrocatalyst (Hirschenhofer *et al*, 1998), indicates the following: the platinum surface area available for reaction per unit mass of catalyst has increased nearly 10-fold, the gas-diffusion and the catalyst layers have been better designed to improve gas permeability and attain optimal wettability by a liquid electrolyte and the thickness of the electrolyte compartment between the electrodes has decreased nearly 10-fold by utilizing silicon carbide matrices. The increase in

platinum surface area is particularly significant because the high platinum loading requirements had always been a major problem in hydrocarbon fuel cell development.

For these reasons, the mathematical model was employed in two ways. First, it was used in order to explain experimental results published in the literature for intermediate temperature (150-220°C) direct propane fuel cells that use concentrated H_3PO_4 as the electrolyte. Subsequently, it was used to predict the performance for the same system in current-state unit cells, as well as the influence of several operating and electrode parameters.

6.2 Comparison of model results with experimental data

In order to model the platinum black electrodes for which experimental data are available, the model was appropriately modified. The structure of these electrodes was discussed by Grubb and Michalske (1964) and by Niedrach and Alford (1965), where it is reported that the platinum loading was 45 mg Pt/cm^2 and the spacer between the electrodes is ~0.32cm thick. The active surface area of platinum for these electrodes is reported as 20m^2/g. Furthermore, in order to make one of the electrode's surfaces hydrophobic, a porous Teflon film was attached to the catalyst layer, instead of the carbon paper or carbon cloth that is presently used as the gas-diffusion layer. Gas transport through this film was modeled using a permeability coefficient to account for the pressure drop across the film. Permeability measurements for Teflon films of the specified thickness were reported by Niedrach and Alford (1965).

These electrodes have also been tested as cathodes for H_2/O_2 cells. The performance data and model predictions for the oxygen cathodes are shown in **Figure 6.1**. Examination of the experimental data reveals that these electrodes were limited by iR-drop because of the relatively large thickness of the electrolyte compartment (the electrodes themselves were sufficiently thin, ~210μm). Limiting currents less than 600 mA/cm^2 were observed. It is evident from the data, that at even lower current densities, for which data for the propane cells were reported, the effect of ionic conduction losses is substantial. The iR-free polarization curve predicted by the mathematical model for the cathode (**Figure 6.1**, line (1)) is in good agreement with the reported data, which signifies that the model for the oxygen electrode is sufficiently accurate.

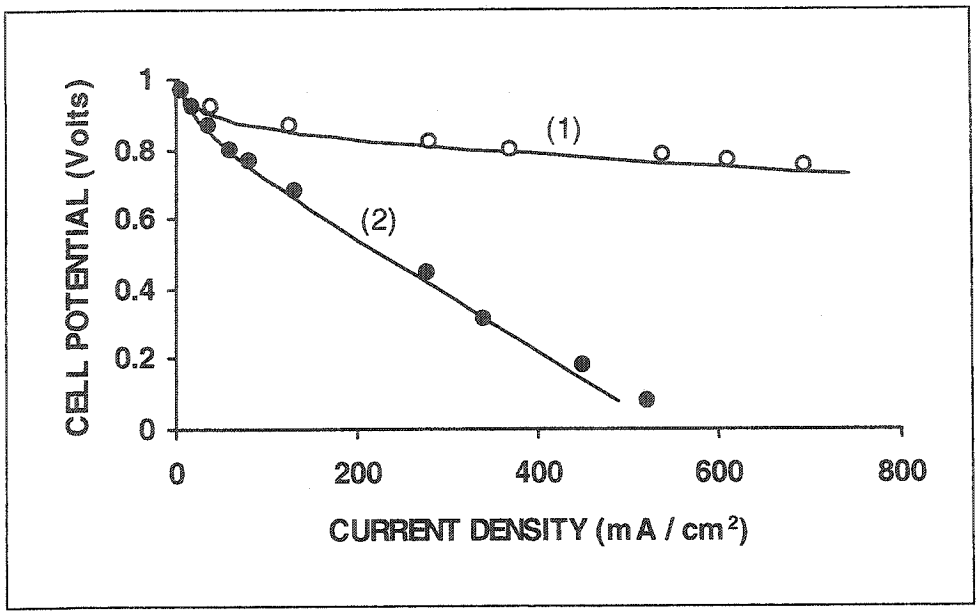

Figure 6.1: Experimental data and model results for H_2/O_2 cells used by Grubb and Michalske (1964). Platinum loading is 45 mg/cm^2 on cathode: • experimental; — (2) model; ○ experimental, IR-free; — (1) model, IR-free.

Figure 6.2 shows experimental results at 150°C for the same Pt black electrodes, used as both anode and cathode in propane/oxygen cells by Grubb and Michalske (1964), and the corresponding model results. The data indicate a substantial decrease in performance as the concentration of H_3PO_4 is increased. The modeling results are in good agreement with the experimental data. It should be noted that the model predicted accurately the effect of acid concentration on the electrode performance by considering the propane oxidation reaction rate to be proportional to the activity of water in solution. This agreement may indicate that the performance decrease in very concentrated acid solutions is indeed caused by the unavailability of free water molecules because water is a reactant in the anode (and not by other effects such as increased adsorption of a phosphoric acid species on Pt at high concentrations (Grubb and Michalske, 1964). It may also indicate that dependence of the propane oxidation rate on water activity is first-order. In addition, if water is required for the hydration of protons, the formation of hydronium ions may be inhibited by the lack of free water. Stoichiometry indicates that every molecule of propane reacts with 6 molecules of water and produces 20 protons. Therefore, the water requirement for transfer of protons will exacerbate the water requirement for the reaction.

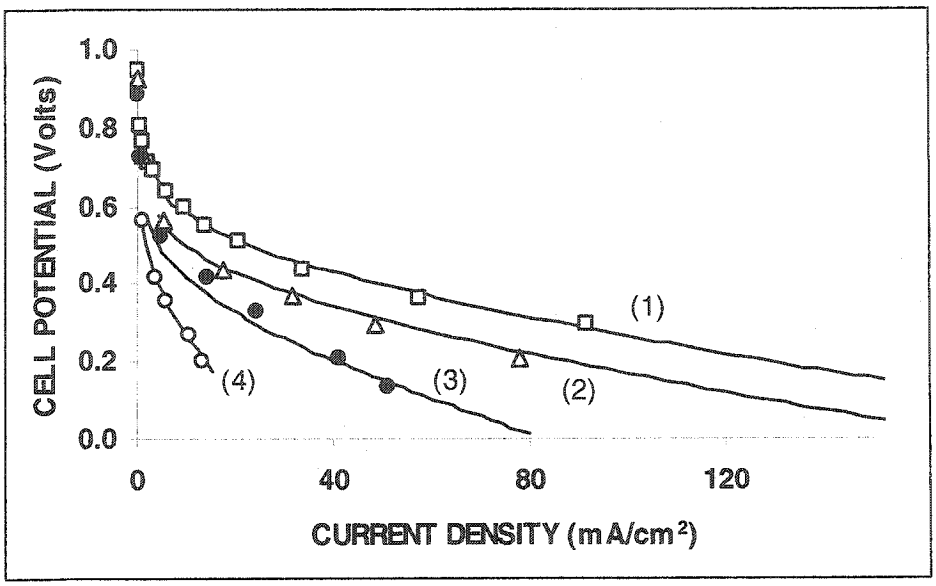

Figure 6.2: Experimental data (Grubb and Michalske, 1964) and model predictions for C_3H_8/O_2 cells for different phosphoric acid concentrations. The numbered solid lines denote model predictions. Platinum loading is 45 mg/cm^2 on each electrode. T=150°C. ف, (1) 85% H_3PO_4; Δ, (2) 96% H_3PO_4; •, (3) 101% H_3PO_4; ○, (4) 105% H_3PO_4

The normalized residuals for the model-predicted curves of Figure 6.2 are shown in **Figure 6.3**. The normalized residuals are defined as the error in the prediction of the cell potential (= Model Predicted Cell Potential – Experimental Cell Potential) divided by the experimental values of cell potential for the experimental data of Figure 6.2. The plot illustrates the close agreement between the model-predicted polarization curves and the experimental values and verifies that there is no apparent trend between the model error and the current-density. The error in the prediction is approximately the same for the whole range of current-densities. Furthermore, the predictions are within 10% of the experimental values.

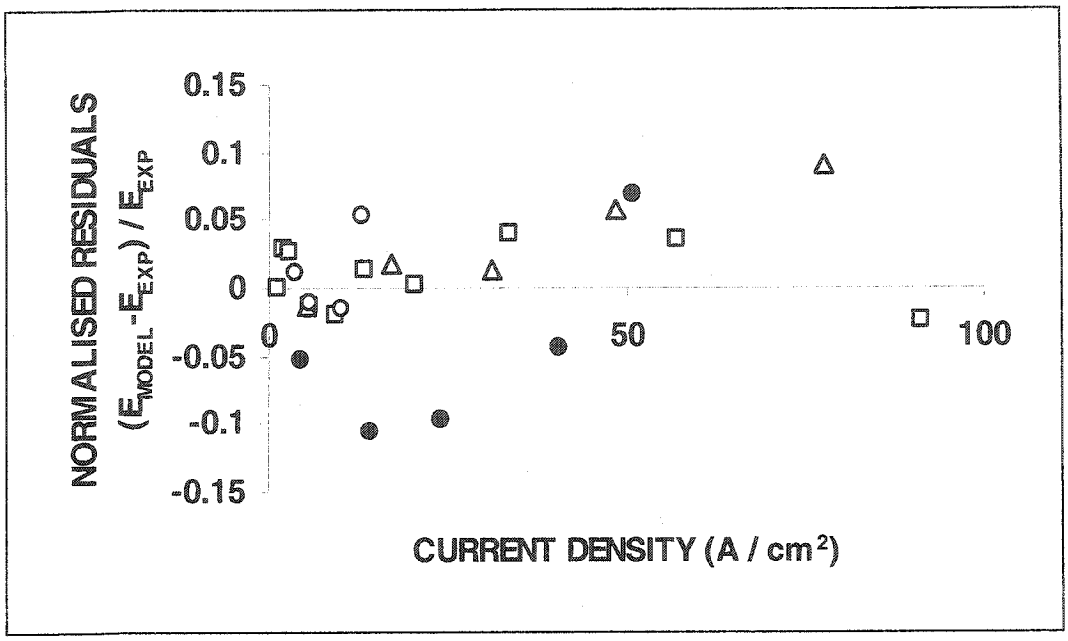

Figure 6.3: Normalised residuals for model predictions of Figure 6.2: ⌓85% H_3PO_4; Δ 96% H_3PO_4; • 101% H_3PO_4; ○ 105% H_3PO_4

The variance of the model predictions for the four lines corresponding to different phosphoric acid concentrations is shown in **Figure 6.4** as a function of acid concentration. The variance was obtained as the sum of the squared residuals corresponding to each line divided by (n-1), where n is the number of data (experimental). The plot verified that there is no apparent trend between the model error and the phosphoric acid concentration. This shows that the effect of phosphoric acid concentration on the performance of the cell has been sufficiently well described.

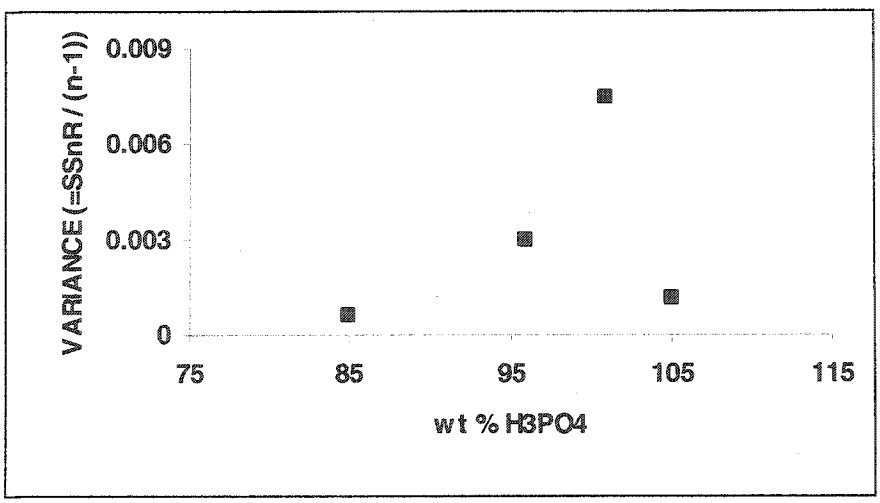

Figure 6.4: Variance of model predicted curves of Figure 6.2 for the four curves corresponding to four different acid concentrations as a function of acid concentration.

Figure 6.5 shows the experimental results and corresponding model predictions for the same electrodes for different combinations of temperatures and electrolyte concentrations that result in the same water vapour pressure above the solution (600 mmHg). It is evident that the advantage of increased temperature operation for the more concentrated solutions more than offsets the concentration effect. Operation at 200°C with 95 wt% H_3PO_4 gives the better performance for the cases considered, and was selected as the operating condition for predicting the effect of other variables on performance in this study. A comparison between lines (1) and (2) in Figure 6.5 indicates the possible increase in performance if iR-loss was decreased in the propane cell. The performance predicted by the model was in all cases in close agreement with the experimental data.

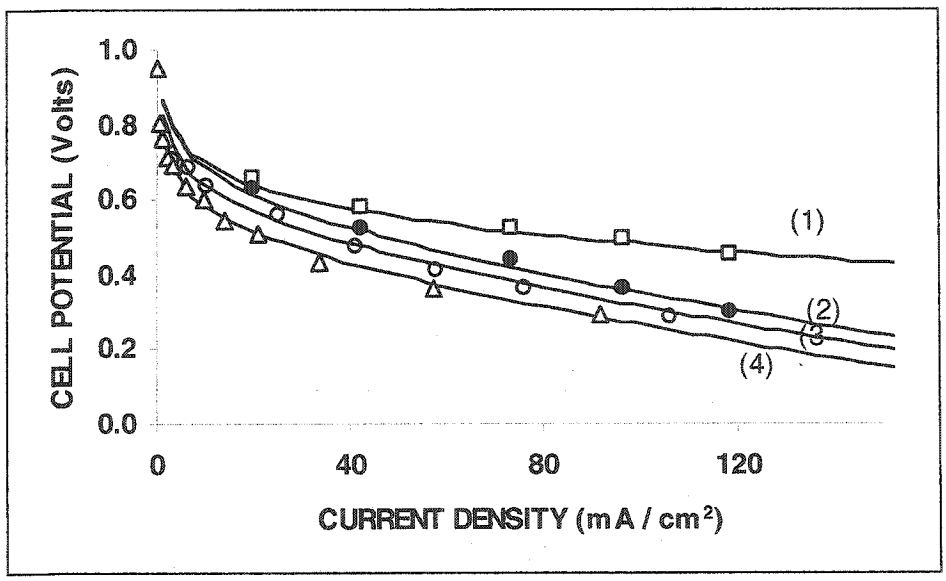

Figure 6.5: Experimental data by Grubb and Michalske (1964) and model predictions for C_3H_8 / O_2 cells for different combinations of phosphoric acid concentration and temperature. The numbered solid lines denote model predictions. Platinum loading is 45 mg/cm^2 on each electrode. ▲, (1) 95% H_3PO_4, 200°C, IR free; ●, (2) 95% H_3PO_4, 200°C; ○, (3) 91% H_3PO_4, 175°C; Δ, (4) 85% H_3PO_4,150°C

The normalized residuals for the model-predicted curves of Figure 6.5 are shown in **Figure 6.6.** The plot illustrates the close agreement between the model-predicted polarization curves and the experimental values and verifies that there is no apparent trend between the model error and the current density. The error in the prediction is again approximately the same for the whole range of current densities. Furthermore, the predictions are within 5% of the experimental values.

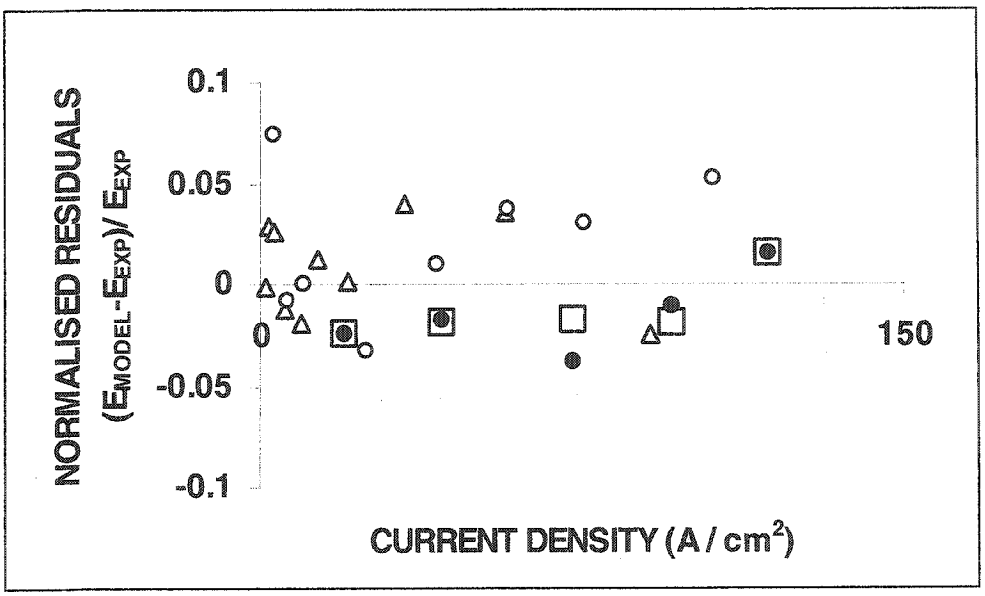

Figure 6.6: Normalised residuals for model predictions of Figure 6.5: ڤ 95% H_3PO_4, 200°C, IR free; • 95% H_3PO_4, 200°C; ○ 91% H_3PO_4, 175°C; Δ 85% H_3PO_4, 150°C

The variance of the model predictions for the four sets of data of Figure 6.6 is shown in **Figure 6.7** as a function of temperature. The plot verified that there is no apparent trend between the model error and temperature. This shows that the effect of temperature on the performance of the cell has been sufficiently well described.

It was concluded from Figures 6.1-6.7 that the form of the model and the used values of the parameters can predict accurately the behaviour of the propane oxidation and oxygen reduction reactions on platinum catalysts in H_3PO_4, for the range of temperatures and acid concentrations of interest in this study. The rest of the work concentrated on predicting the performance of C_3C_8/O_2 cells using present-state PAFC electrode characteristics and on the effect of several operating and electrode-structure parameters on the performance of the unit cell.

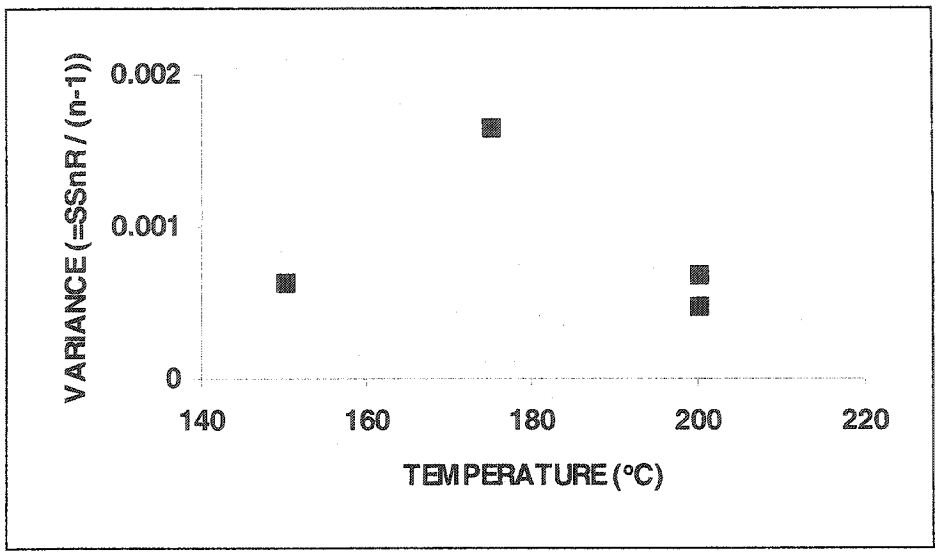

Figure 6.7: Variance of model predicted curves of Figure 6.5 for the four curves corresponding to four different temperatures/ acid concentration combinations as a function of temperature

6.3 Model predictions of the performance of propane-oxygen cells utilizing Pt/C electrodes – Effects of operating conditions and electrode properties

Figure 6.8 shows the predicted performance curves for C_3C_8/O_2 cells with Pt/C electrodes in 95%H_3PO_4, operating at atmospheric pressure at 200°C, at 20% utilization of both propane and oxygen, for different combinations of platinum loadings, catalyst layer thicknesses and weight percentage of Pt-catalyst on C-support, listed in **Table 6.1**. The predicted performance for a total cell loading of 2.5 mg Pt/cm^2 (2mg Pt/cm^2 in the anode and 0.5mg/cm^2 in the cathode) (line 1) is better than that for the Pt electrodes used by Grubb and Michalske (1964) (containing 90 mg /cm^2 total platinum loading) (line 5), for current-densities greater than ~150 mA/cm^2. This is due to the effects of greater Pt surface area per unit mass and lower iR-drop for the thinner SiC electrolyte matrix (~250μm thickness was assumed although they may be even thinner (Caires *et al*, 1997). The predicted performance is much better for double Pt loading (5mg Pt/cm^2) resulting from using thicker electrode catalyst layers (lines 2, 4) but the performance is expected to increase only slightly if the Pt loading is doubled by using higher concentrations of Pt on C catalyst (line 3), because of the decrease in available Pt surface area associated with Pt particle agglomeration in the more concentrated catalyst.

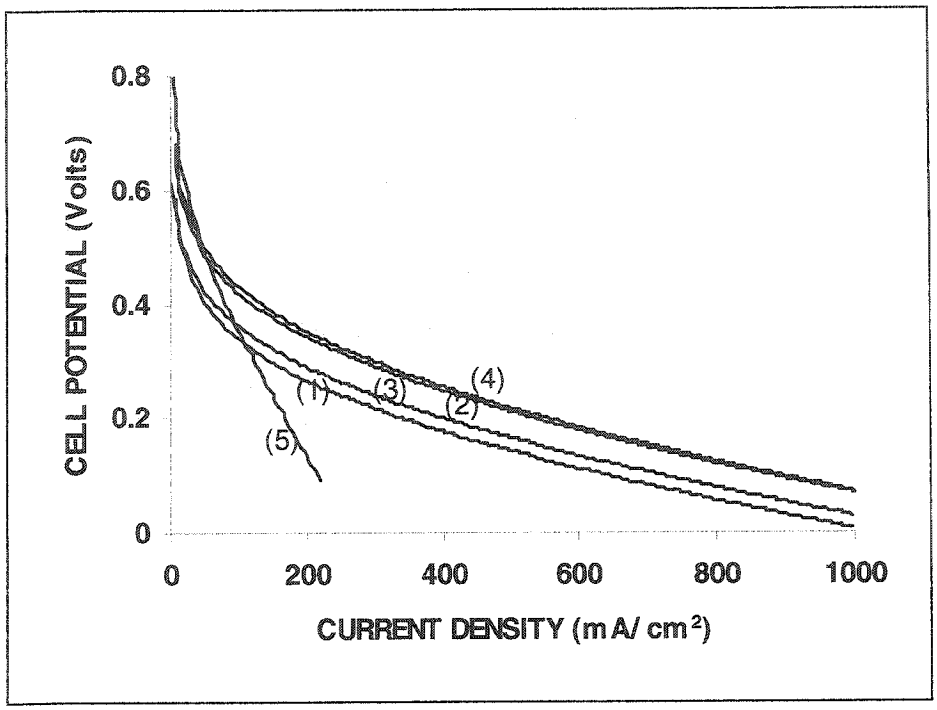

Figure 6.8: Predicted performance curves for C_3H_8/O_2 cells for Pt/C electrodes, 200°C, 95% H_3PO_4, 1 atm and 20% utilization: (1-4) Electrode parameters given in Table 6.1; (5) Pt black electrodes of 45 mg/cm^2 Pt loading (Grubb and Michalske, 1964)

Table 6.1: Electrode parameters corresponding to the polarization curves of Figure 6.8

Line	Pt loading (mg Pt/cm^2)			Catalyst layer thickness (μm)		Catalyst concentration (wt% Pt on C)	
	Cathode	Anode	Total	Cathode	Anode	Cathode	Anode
(1)	0.5	2	2.5	150	150	10%	40%
(2)	1	4	5	300	300	10%	40%
(3)	1	4	5	150	150	20%	80%
(4)	1	4	5	300	450	10%	26.7%

The maximum of the range of current-density presented in Figure 6.8 and the predictions in the plots that follow was chosen to be 1 A / cm^2. This range was chosen because for any hydrocarbon cell data published in the literature, very high current-densities have not been observed and the model does not take into account other possible physical phenomena such as carbon monoxide poisoning of the catalyst and carbon deposition on the catalyst, the effect of which may be substantial, particularly at high current densities (Liebhafsky and Cairns, 1968). However, the electrochemical reaction rate parameters used for the simulation of the predictions of Figure 6.8 are the same as those used for the simulation of the experimental data appearing in Figures 6.2

and 6.5. The program that was written in MATLAB for the anode electrode corresponding to line (2) of Figure 6.8 is given in **Appendix B2**.

The predicted effect of reactant gas pressure is presented in **Figure 6.9**. For lines 1-3, the rest of the parameters were fixed as those corresponding to figure 6.8, line 2. The presented results are for equal gas pressures in the anode and cathode gas channels of the cells. For 10 atm pressure (line 3), a cell voltage of 0.3 volts is predicted for ~1 Ampere/cm^2 current-density for 5 mg Pt/cm^2 total platinum loading (anode and cathode). The predicted performance for 2.5 mg Pt/cm^2 (line 4) is only slightly worse. It should be concluded from the predictions, that operation at high pressure may be particularly beneficial for direct hydrocarbon fuel cells.

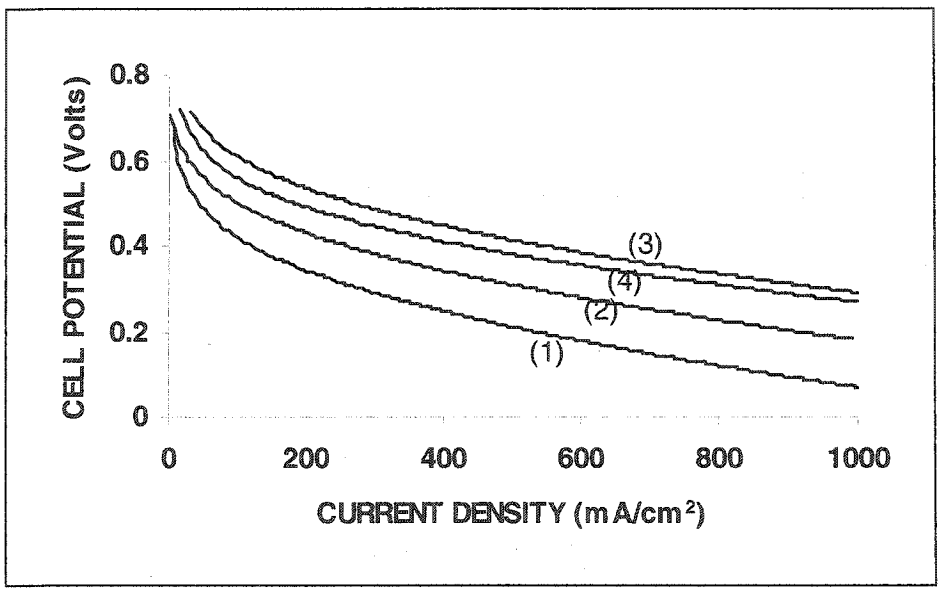

Figure 6.9: Predicted effect of reactant gas pressure on performance of C_3H_8/O_2 cells, 200°C, 95% H_3PO_4, 20% utilization: (1) 1 atm, 5mg Pt/cm^2; (2) 3 atm, 5mg Pt/cm^2; (3) 10 atm, 5mg Pt/cm^2; (4) 10 atm, 2.5mg Pt/cm^2

The predicted effect of propane and oxygen utilizations is illustrated in **Figure 6.10**. The results correspond to instantaneous utilization values at a specific location of the anode and cathode gas channels (and not integral performance of the unit cell, which can only be predicted by two or three-dimensional models). The relative utilisation of oxygen and propane can be independently controlled by adjusting the gas flowrates in the gas-supplying channels or by changing the relative positions of inlet gas manifolds. Thus, it is possible to have high oxygen utilization locations corresponding to low fuel utilization locations in counter-current flow of the fuel and

oxidant in the gas channels, so that several cases were considered. As expected, the performance is decreased at high utilizations and the effect of propane utilization is more significant.

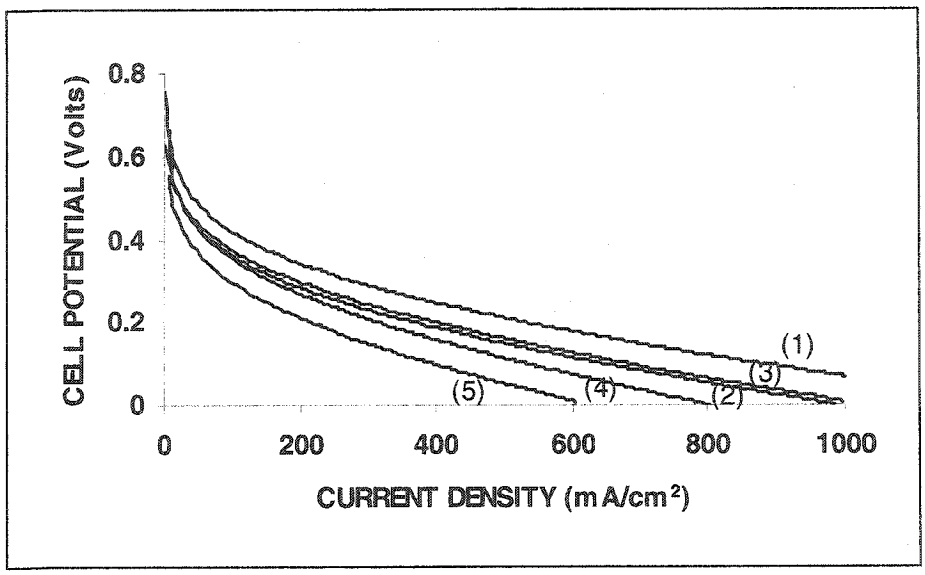

Figure 6.10: Predicted effect of reactant gas utilization on performance of C_3H_8/O_2 cells, 200°C, 95% H_3PO_4, 1 atm, 5 mg Pt/cm^2. Utilization = (1) 20%O_2, 20%C_3H_8; (2) 80%O_2, 20%C_3H_8; (3) 50%O_2, 50%C_3H_8; (4) 20%O_2, 80%C_3H_8; (5) 80%O_2, 80%C_3H_8

The effect of operating temperature, for operation at high pressure (10 atm), is shown in **Figure 6.11**. Operation at high pressures permits higher temperatures of operation owing to increase in the electrolyte's boiling point. It is predicted that increasing the temperature to 215°C (line 3) results in considerable increase in performance. Further increase in temperature, allowed by using more concentrated electrolyte, will not necessarily improve performance (line 4).

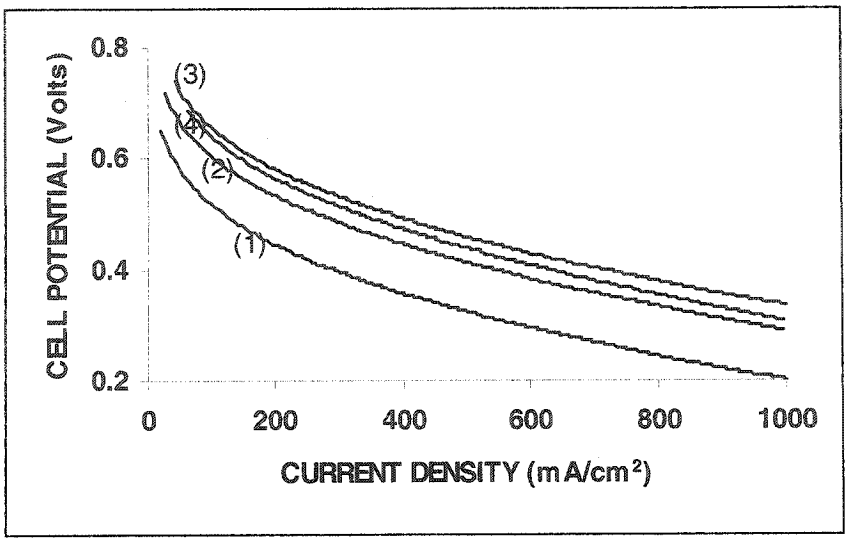

Figure 6.11: Predicted effect of temperature on performance of C_3H_8/O_2 cells for Pt/C electrodes, 10 atm, 5 mg Pt / cm^2: (1) 185°C, 95%H_3PO_4; (2) 200°C, 95% H_3PO_4; (3) 215°C, 95% H_3PO_4; (4) 230°C, 100% H_3PO_4

Figure 6.12 presents a comparison between the predicted performance of two propane cells, one operating with an air cathode and one operating with an oxygen cathode. Owing to the performance loss associated with operation in air and the high polarization of the anode for direct propane fuel cells, operation in pure oxygen may be beneficial, although not always practical.

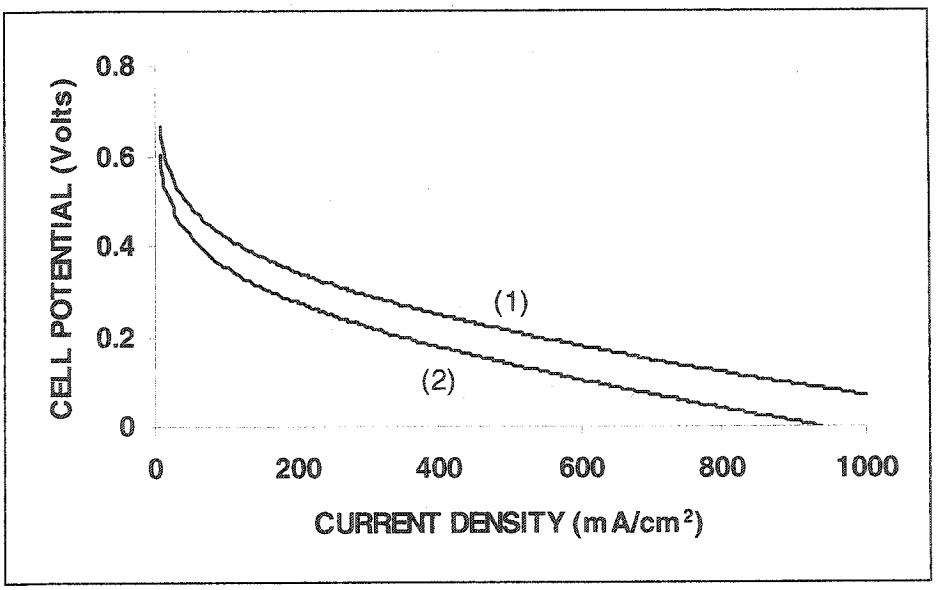

Figure 6.12: Predicted performance curves for C_3H_8 cells for Pt/C electrodes, 200°C, 95% H_3PO_4, 1 atm, 20% utilization, 5 mg Pt/cm^2: (1) oxygen cathode; (2) air cathode

Figure 6.13 shows the predicted polarization (potential loss) for three different electrodes: an anode containing 4 mg/cm^2 Pt, an oxygen cathode containing 1mg/cm^2 Pt and an air cathode containing 1mg/cm^2 Pt. The electrical potential loss for the propane electrode is much greater than that for the oxygen or air cathodes, which shown the need for concentrating the greatest proportion of the total Pt loading in the anodes of direct hydrocarbon fuel cells.

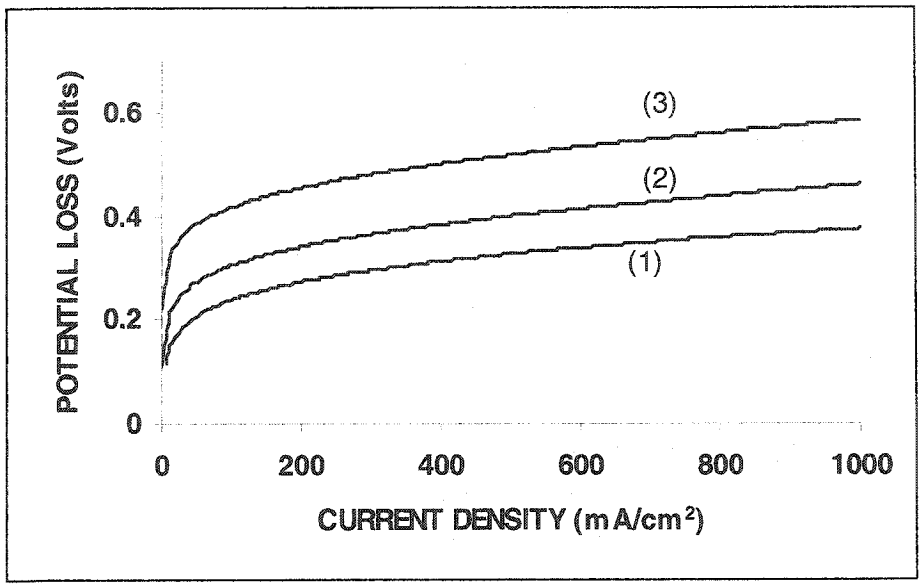

Figure 6.13: Predicted electrode potential loss at 200°C, 1 atm for: (1) An oxygen cathode, 1mg Pt/ cm^2; (2) An air cathode, 1mg Pt/ cm^2; (3) A propane anode, 4mg Pt/ cm^2

On the basis of the present model, no limiting currents are predicted up to current-densities of 1 A/cm^2 other than the case of very low water content in the electrolyte. It is possible that the catalyst deactivation effect which is caused by adsorbed CO on the platinum surface has an impact on the performance of the anode. The present model does not consider this effect. For more sophisticated modeling, detailed description of the adsorption and reaction behaviour of hydrocarbons on the catalyst surface would be required, which is a problem coupled with the need for clarification of the reaction mechanism.

6.4 The effect of some model parameters

In this section, the predicted effects of some physicochemical and electrochemical model parameters on the performance of a propane anode are presented (sensitivity analysis). The effects of many parameters on the performance of a cathode were considered in section 5.7. In

this section, some parameters that affect the anode are considered. Particularly, the effect of the values of the parameters used for the exchange current-density for the propane oxidation reaction, the transfer coefficient for the reaction and the size of the agglomerates of the solid Pt/C catalyst in the anode. The values for these parameters that were used in the simulations that have already been discussed are presented in **Table 6.2**.

Table 6.2: Physicochemical and electrochemical parameters used in the simulation of propane anode electrode

Parameter	Value
Exchange current-density at 200°Cfor propane oxidation	1.5×10^{-7} A/cm^2
Anodic transfer coefficient	1
Agglomerate's radius	1μm

Figure 6.14 presents the anode polarization (total potential loss in the anode) for different values of the exchange current-density of the reaction at 200°C,1 atm pressure and 4 mg Pt /cm^2 platinum loading. The model-predicted plots present the anode polarization (deviation of the anode potential from the equilibrium potential for propane oxidation) as a function of the current-density. It is predicted that about 100 mv of electrode potential is gained for every 10-fold increase in the value of the exchange current for the reaction.

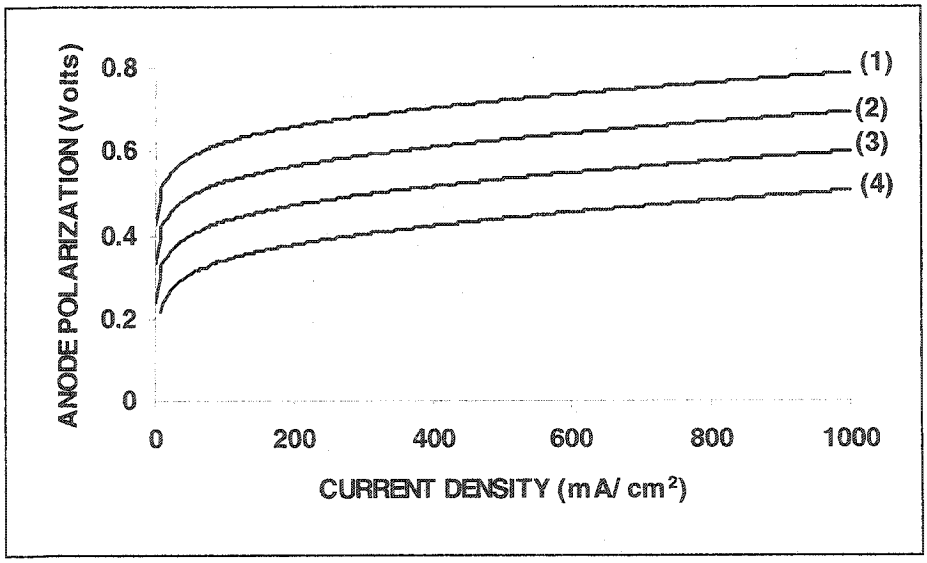

Figure 6.14: Predicted effect of exchange current-density on the performance of a propane anode electrode (200°C, 1 atm, 4 mg Pt/ cm^2). Exchange current-density = (1) 10^{-9} A/cm^2; (2) 10^{-8} A/cm^2; (3) 10^{-7} A/cm^2; (4) 10^{-6} A/cm^2

Figure 6.15 presents the effect of the anodic transfer coefficient for the hydrocarbon oxidation reaction on the performance of the cell. The electrode polarization is plotted against the produced current-density for three different possible values of the transfer coefficient α. As expected, the value of the transfer coefficient is critical because it determines the Tafel slope for the reaction and thus the sensitivity of the surface overpotential to the delivered current density.

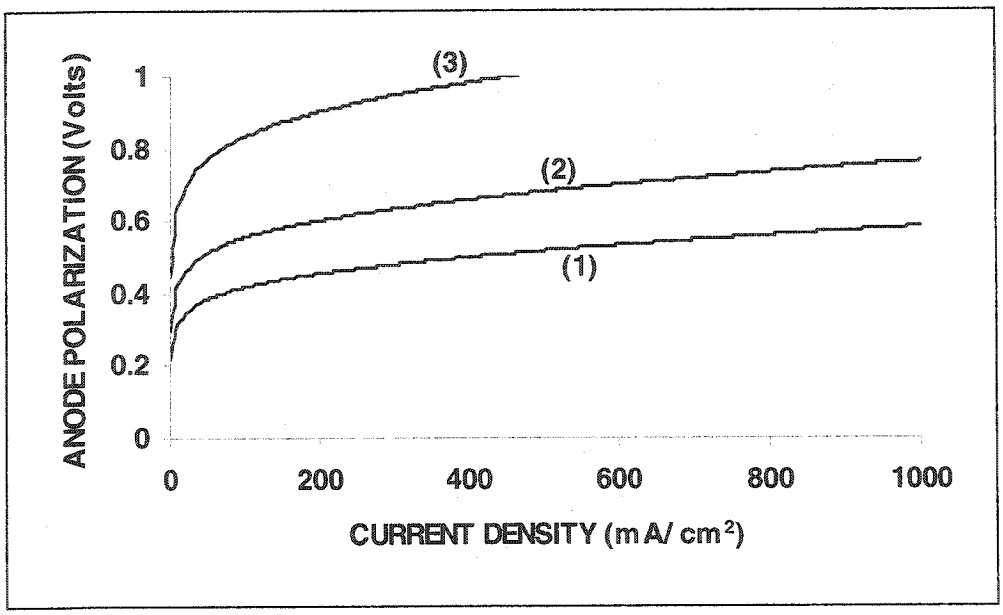

Figure 6.15: Predicted effect of anodic transfer coefficient for the oxidation reaction on the performance of a propane anode electrode (200°C, 1 atm, 4 mg Pt/ cm^2). (1) α=1; (2) α=0.75; (3) α=0.5

Figure 6.16 presents the predicted effect of the value used for the agglomerate's radius on the predicted performance. The effect of the agglomerate size on the predictions is significant for agglomerate radii larger than ~1μm. The limiting current observed in line (4), for which the agglomerate's radius was taken to be 5 μm, is caused by the large propane concentration drop in the agglomerate and the liquid film that surrounds it.

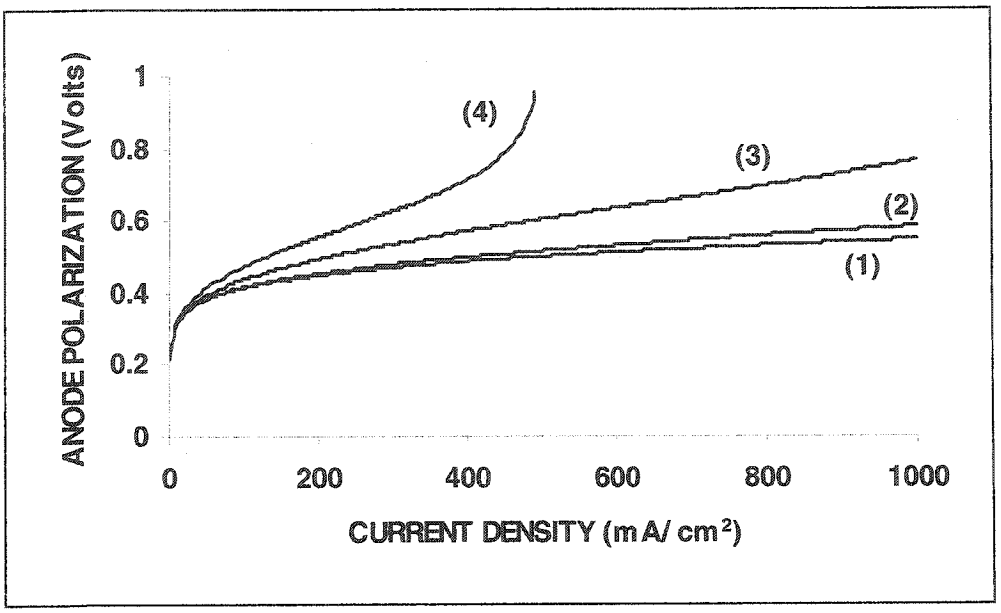

Figure 6.16: Effect of agglomerate radius on the predicted performance of propane anode electrode (200°C, 1 atm, 4 mg Pt/ cm^2). Agglomerate radius = (1) 0.1μm; (2) 1μm; (3) 3μm; (4) 5 μm

6.5 The magnitude of electrical potential-loss contributing processes

In this section the effect of the various resistances that can possibly cause potential losses in a propane anode electrode is examined. These processes are the surface reaction (overpotential), the various diffusion processes (concentration polarization) and ionic conduction (ohmic polarization). Using the mathematical model developed for the anode, the effect of these processes was examined using the method described in section 5.3 in conjunction with the analysis of the cathode electrode. The elimination of each resistance was done by forcing the relevant parameters to extremely high values (10^{10}). For example, to eliminate the ohmic overpotential, it was sufficient to use as an input for the electrolyte ionic conductivity an extremely large number.

Figure 6.17 presents the electrode polarization (the deviation of the electrode potential from the equilibrium potential for the propane oxidation reaction) versus the current-density curves after subsequently eliminating each resistance. The result corresponds to 20% propane conversion.

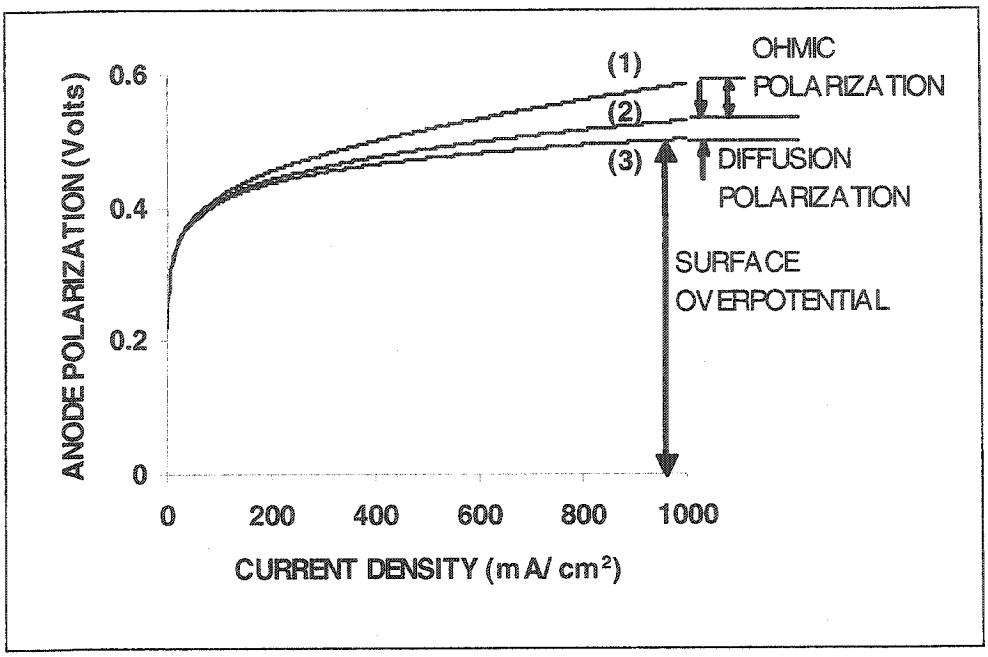

Figure 6.17: Predicted polarization curve for propane anode (200°C, 1 atm, 4 mg Pt/ cm^2) after successive elimination of various resistances at 20% local propane conversion: (1) all resistances included; (2) no ionic conduction loss; (3) no diffusion loss in agglomerates, liquid film and gas phase

Figure 6.17 shows that for all current densities considered the process that overwhelmingly determines the polarization is the electrochemical reaction on the surface of the catalyst. This result is very important because it suggests that possible significant improvement of a direct propane fuel cell anode can only be realized if the electrochemical hydrocarbon oxidation reaction rate is improved. It also suggests that the effect of uncertainties in physicochemical variables not directly related to the surface reaction (such as propane diffusion coefficient in the gas and liquid phase and the electrolyte conductivity) can be considered to be insignificant.

Figure 6.18 is analogous to Figure 6.17, except that, the anode polarization versus current-density curves, correspond to a propane conversion of 80%. In a propane fuel cell, this would correspond to a location downstream from that of Figure 6.17, where most (80%) of the propane would have reacted and therefore the anode polarization is greater. As was evident from the results of Chapter 5, the conversion affects the relative contribution of the various resistances. The potential loss caused by the various modes of oxygen diffusion (the difference between lines (2) and (3) in Figure 6.18) was predicted to be greater as the gas channel propane partial pressure

was decreased. However, even at this high value of propane conversion, the surface polarization still contributes the overwhelmingly greater potential loss in the electrode.

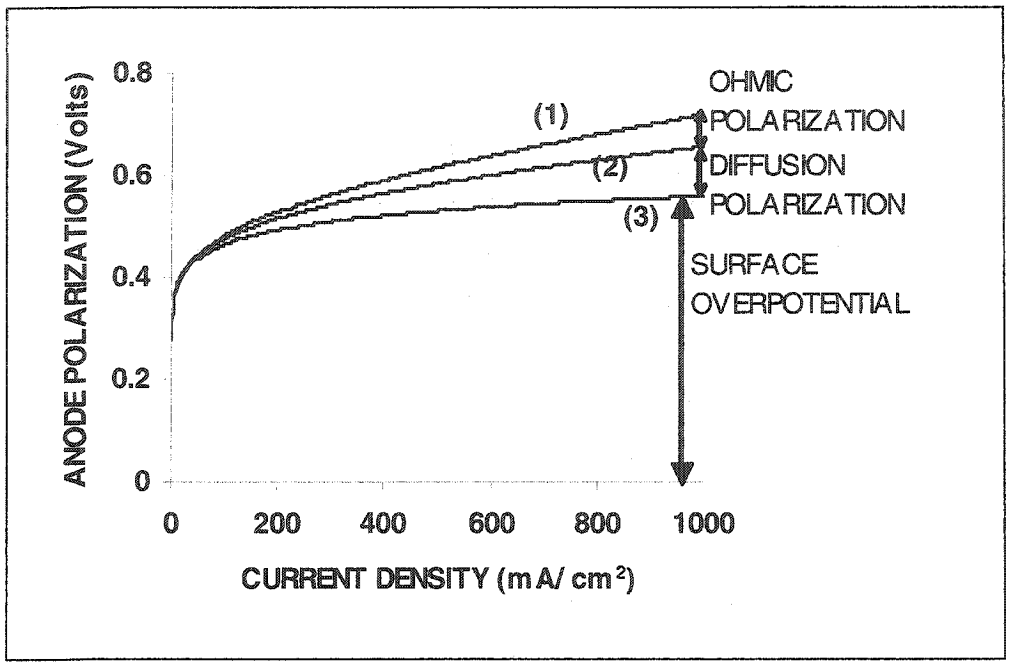

Figure 6.18: Predicted polarization curve for propane anode (200°C, 1 atm, 4 mg Pt/ cm^2) after successive elimination of various resistances at 80% local propane conversion: (1) all resistances included; (2) no ionic conduction loss; (3) no diffusion loss in agglomerates, liquid film and gas phase

6.6 Power density and fuel efficiency

The power density produced by a fuel cell is given by the product of the produced current-density and the terminal cell potential. The model-predicted power density of a direct propane/ oxygen unit cell utilizing Pt /C electrodes, with total platinum loading of 5 mg Pt / cm^2, operating at 200°C and 1 atm pressure is shown in **Figure 6.19** as a function of the current-density. As expected for any such curve, the power density reaches a maximum and then starts dropping with further increase of the current-density (Bockris and Srinivasan, 1969).

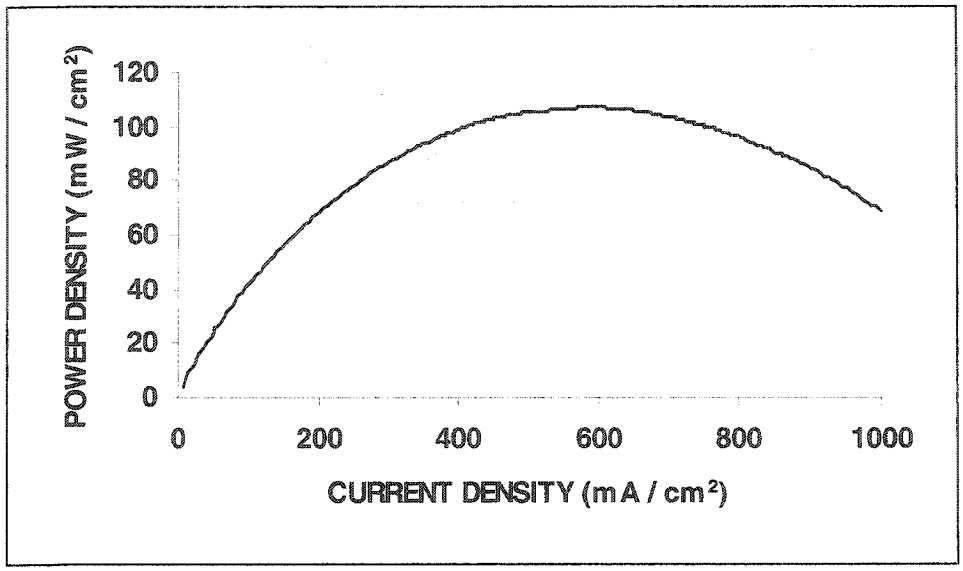

Figure 6.19: Predicted power density versus current density curve for a propane/oxygen cell utilizing Pt/C electrodes and 95% phosphoric acid electrolyte at 200°C, 1atm pressure and 5 mg Pt/cm^2 total platinum loading

It is interesting to note that the maximum power density obtained by Savadogo and Rodriguez (2001) for a direct propane fuel cell utilizing a membrane electrolyte, with Pt catalyst supported on carbon in the anode and total platinum loading 2.4 mg /cm^2, operating at 95°C, showed a maximum power density of 18 mW /cm^2, while that with Pt-CrO_3 catalyst showed a performance maximum 46 mW /cm^2. The predicted performance of the simulated cell of Figure 6.18 should be expected to be superior based on the higher temperature and higher platinum loading.

The maximum energy conversion efficiency for a fuel cell is the conversion efficiency at equilibrium conditions when no current is produced. When a fuel cell is operating at a practical current density the cell output voltage is less than the equilibrium value.The real energy conversion efficiency of the electrochemical cell is lower than the equilibrium value and a function of the produced current density. The real energy conversion (or fuel) efficiency for a fuel cell is given by (Bockris, 1969):

$$\varepsilon = \frac{\text{Electrical Work output}}{\text{Heat input}} = \frac{nFE_{cell}}{-\Delta H_c} \tag{6.1}$$

where E_{cell} denotes the cell output voltage and $-\Delta H_c$ the enthalpy of combustion at constant pressure for the fuel. Therefore the efficiency of the cell becomes decreased as the cell potential is decreased with increasing the load current. **Figure 6.20** shows the efficiency versus current

density curve predicted by the model for a direct propane/ oxygen unit cell utilizing Pt /C electrodes, with total platinum loading of 5 mg Pt / cm^2, operating at 150°C, for 1 atm and 10 atm pressure. In a real cell the energy required for pressurizing the gases would have to be considered.

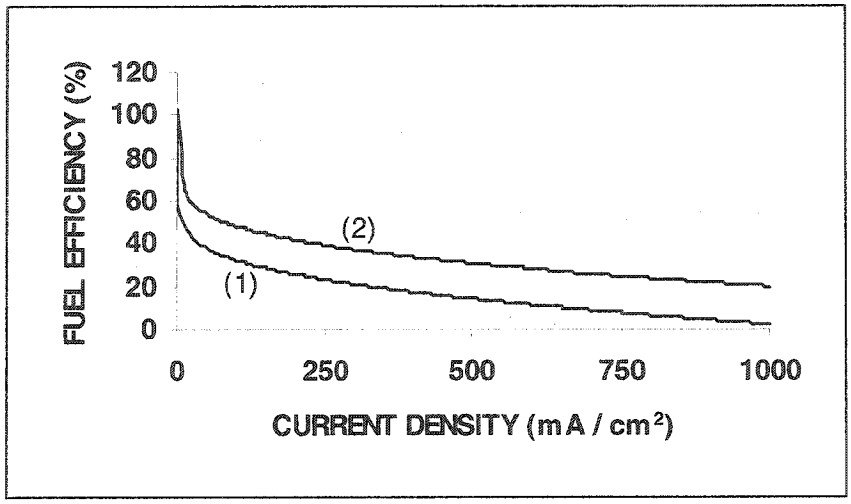

Figure 6.20: Predicted energy conversion efficiency versus current density curve for a propane/oxygen cell utilizing Pt/C electrodes and 85% phosphoric acid electrolyte at 150°C, 5 mg Pt/cm^2 total platinum loading and; (1) 1 atm pressure; (2) 10 atm pressure

CHAPTER 7: CONTRIBUTIONS TO ORIGINAL RESEARCH, CONCLUSIONS AND RECOMMENDATIONS

7.1 Contributions to knowledge

In this thesis, a mathematical model for a direct propane fuel cell was developed. The model was used to predict and analyze the performance of a phosphoric acid fuel cell cathode electrode utilising oxygen or air, a phosphoric acid fuel cell anode electrode utilizing propane and a phosphoric acid unit cell utilizing propane and oxygen as the fuel and oxidant respectively. The contributions to knowledge offered in this work are summarized here.

For the work on the propane unit cell, the following contributions can be identified:

1) The first numerical model that attempted to simulate a direct hydrocarbon fuel cell was developed.

2) The effects of many operating variables and electrode characteristics, including the electrolyte concentration, operating temperature, gas pressure, fuel and oxidant conversion, platinum loading, catalyst layer thickness and Pt/C catalyst composition were predicted.

3) The electrical potential (cell voltage) losses caused by the various phenomena (surface reaction, diffusion and ionic conduction) were predicted.

For the work on the phosphoric acid fuel cell cathode electrode, the following contributions can be identified:

1) A detailed derivation of various model parameters required for the spherical agglomerate model of the electrode's catalyst layer, based on the electrode's morphological and absorptive characteristics, was presented. These include the volume fractions of the various phases in the electrode, the thickness of the liquid film surrounding the agglomerates and the surface area of platinum that is available for reaction.

2) The model that was described in this work is more comprehensive than any other model in the literature. Although several numerical models for the phosphoric acid fuel cell electrode appear in the literature, this is the first to include collectively all of the following: the dependence of oxygen solubility and diffusivity in phosphoric acid on the operating temperature and the electrolyte's concentration, the dependence of the specific conductivity of phosphoric acid on the temperature, the electrolyte concentration and the liquid volume fraction in the catalyst layer, the dependence of platinum surface area on the concentration of the catalyst, the dependence of the equilibrium potential on the temperature, the dependence of the exchange current density on temperature and the effect of the existence of a liquid film and the thickness of the liquid film surrounding the solid phase particles.

3) A detailed description of the shooting method and its usefulness in satisfying the natural boundary conditions of the systems of equations developed for the several fuel cell layers was presented. In particular, the shooting method greatly simplifies the coupling of the numerical solutions over several fuel cell layer while solving the associated differential equations by advancing from left to right along the thickness of the fuel cell, even if the information propagates in both directions within the mathematical model.

4) This is the only fuel cell model that has ever shown how oxygen conversion influences fuel cell performance over the complete range of current-densities. The potential losses caused by the various processes in the electrode (oxygen reduction on the catalyst, diffusion of oxygen in the gas and liquid phase and ionic conduction) were predicted as a function of both the current-density and the local oxygen conversion. Contour plots of constant percentage of the total potential loss contributed by each process as a function of both conversion and current density were prepared. As a result, the regions of current density and oxygen conversion values for which each process has a considerable effect could be identified.

5) The sensitivity of the results of the agglomerate model on the values of the parameters required by the model was described.

7.2 Conclusions

The most important conclusions that can be drawn from the model results on the direct propane phosphoric acid fuel cell can be summarized as follows:

1) The results of the mathematical model used with the optimized parameters for the equations describing the electrochemical oxidation of propane on platinum were in good agreement with experimental performance curves. The predictions on the effect of the concentration of phosphoric acid and the effect of operating temperature agreed well with existing experimental data. It was found that, by considering the rate of the propane oxidation reaction to be proportional to the activity of water in the electrolyte, the strong dependence of the cell performance on the electrolyte concentration could be explained. The result suggests that the unavailability of sufficient amount of water in the electrode pores of a hydrocarbon fuel cell anode can cause significant performance losses.

2) The model predicted that the performance of direct hydrocarbon fuel cells can be improved by making changes to the electrode characteristics and by optimizing the operating conditions.

2a) It was predicted that by utilizing state-of-the-art Pt/C gas-diffusion electrodes, used in phosphoric acid fuel cells, the amount of platinum catalyst required to achieve the performance reported in previous experiments (Grubb and Michalske, 1964) can be significantly decreased.

2b) It was predicted that increasing the fuel gas pressure and the operating temperature can significantly enhance the cell performance.

2c) It was predicted that for any particular platinum loading in the anode electrode, the performance is enhanced if the weight percentage of platinum in the platinum-carbon catalyst is kept to low values, therefore requiring a thicker electrode. The potential loss caused by the decrease in available platinum surface area for a catalyst that is highly concentrated with platinum was found to be more significant than the ionic conduction and gas diffusion losses associated with using thicker electrode's catalyst layer.

2d) It was verified that high propane utilization (conversion) in the electrode can significantly decrease the performance.

3) It was verified that the process that causes the largest potential losses in a direct propane fuel cell at all current-densities is the electrochemical reaction of propane oxidation on the surface of the catalyst.

The most important conclusions that can be drawn from the model results on the cathode of a phosphoric acid fuel cell can be summarized as follows:

1) The model was found capable of predicting the experimental data from two different cathodes reported in the literature by adjusting two model parameters to physically reasonable values.

2) It was predicted that at all current densities the process that contributes the largest potential losses in the electrode is the electrochemical reduction of oxygen on the surface of the catalyst.

3) The effect of oxygen diffusion in the gas-filled electrode pores was predicted to be insignificant. On the other hand, the effects of oxygen diffusion in the liquid filled pores and of ionic conduction losses were found to be significant, particularly at high current densities. The results show that the use of the complicated Stefan-Maxwell equations to describe gas diffusion is unnecessary for simulating the electrode. However, it is critical to describe as accurately as possible the process of gas diffusion in the liquid phase.

4) As the partial pressure of oxygen decreases along the gas channel of fuel cell cathode, the potential losses contributed by the dissolved oxygen diffusion process become progressively larger. As a result, at high values of oxygen conversion the concentration polarization is much larger than at low values of oxygen conversion.

5) For different combinations of phosphoric acid concentration and operating temperature that result in the same value of water vapour pressure of the electrolyte, the difference in performance is negligible.

6) There exists an optimum catalyst layer thickness for which the performance of the electrode is optimized. For a particular electrode, the optimum thickness depends on the operating current density.

7.3 Recommendations

Some recommendations for future work can be based on the conclusions derived from the results of this work. It is suggested that more experimental work on the performance of direct hydrocarbon fuel cells would be required in order to assess the predictions of this model. No experimental data on the performance of direct hydrocarbon phosphoric acid fuel cells have appeared in the recent literature. It is suggested that the work be extended to examine the performance of other catalysts that can be used for direct hydrocarbon fuel cell applications (for example, PtRu alloys are more tolerant to carbon monoxide poisoning, and can possibly increase the surface reaction rate of hydrocarbon oxidation). Furthermore, many hydrocarbon fuels present themselves as candidates for direct hydrocarbon fuel cell applications, including natural gas and liquid hydrocarbons. On the more theoretical level, clarification of the reaction mechanism of hydrocarbon chemisorption and oxidation would be an important step in understanding the limitations of direct hydrocarbon fuel cells. As suggested by the present work, the propane oxidation reaction on the surface of the catalyst contributes the largest proportion of performance loss in the direct propane fuel cell. For this reason, better understanding of the molecular processes on the electrocatalyst surface would be very valuable, using modern methods of theoretical and experimental analysis and electrochemical surface science.

APPENDIX A: SOLUTION OF EQUATION 2.28 (Proof and method of solution)

Proof that the solution to the equation:

$$\frac{1}{r^2}\frac{d}{dr}\left(r^2\frac{dc}{dr}\right)=\Psi c \tag{A1}$$

subject to the boundary conditions:

$$c = c_i \quad \text{at} \quad r = R_A \tag{BC1}$$

$$\frac{dc}{dr}=0 \quad \text{at} \quad r=0 \tag{BC2}$$

is:

$$c = c_i\frac{R_A}{r}\left(\frac{\sinh(\sqrt{\Psi}r)}{\sinh(\sqrt{\Psi}R_A}\right) \tag{A2}$$

.....

It will be shown that A2 satisfies A1 and the boundary conditions BC1 and BC2. From A2:

$$\frac{dc}{dr} = c_iR_A\frac{\frac{d(\sinh(\sqrt{\Psi}r))}{dr}r\sinh(\sqrt{\Psi}R_A)-\sinh(\sqrt{\Psi}r)\frac{d(r\sinh(\sqrt{\Psi}R_A))}{dr}}{r^2(\sinh(\sqrt{\Psi}R_A))^2}$$

$$\frac{dc}{dr} = c_iR_A\frac{\sqrt{\Psi}\,r\cosh(\sqrt{\Psi}r)-\sinh(\sqrt{\Psi}r)}{r^2(\sinh(\sqrt{\Psi}R_A))} \tag{A3}$$

Therefore:

$$r^2\frac{dc}{dr} = c_iR_A\frac{\sqrt{\Psi}\,r\cosh(\sqrt{\Psi}r)-\sinh(\sqrt{\Psi}r)}{(\sinh(\sqrt{\Psi}R_A))}$$

$$\Rightarrow \frac{d}{dr}\left(r^2 \frac{dc}{dr}\right) = \frac{c_i R_A}{(\sinh(\sqrt{\Psi} R_A))} \left\{\sqrt{\Psi}\cosh(\sqrt{\Psi} r) + r\Psi \sinh(\sqrt{\Psi} r) - \sqrt{\Psi}\cosh(\sqrt{\Psi} r)\right\}$$

$$\Rightarrow \frac{d}{dr}\left(r^2 \frac{dc}{dr}\right) = \frac{c_i R_A}{(\sinh(\sqrt{\Psi} R_A))} r\Psi \sinh(\sqrt{\Psi} r)$$

$$\Rightarrow \frac{1}{r^2}\frac{d}{dr}\left(r^2 \frac{dc}{dr}\right) = \Psi c_i \frac{R_A}{r}\left(\frac{\sinh(\sqrt{\Psi} r)}{\sinh(\sqrt{\Psi} R_A}\right)$$

$$\Rightarrow \frac{1}{r^2}\frac{d}{dr}\left(r^2 \frac{dc}{dr}\right) = \Psi c \qquad \text{(A1)}$$

Therefore, equation A1 is satisfied.

Also, for $r = R_A$, from A2: $c = c_i$. Therefore, BC1 is satisfied.

For $r = 0$, from A3, dc/dr is indeterminate (0/0). Thus, De L'Hospital rule can be used to evaluate the limit:

$$\lim_{r\to 0}\frac{dc}{dr} = \lim_{r\to 0}\left[c_i R_A \frac{\sqrt{\Psi}\, r\cosh(\sqrt{\Psi} r) - \sinh(\sqrt{\Psi} r)}{r^2(\sinh(\sqrt{\Psi} R_A))}\right] = \left[\frac{c_i R_A}{(\sinh(\sqrt{\Psi} R_A))}\right]\lim_{r\to 0}\left[\frac{\dfrac{d\left[\sqrt{\Psi}\, r\cosh(\sqrt{\Psi} r) - \sinh(\sqrt{\Psi} r)\right]}{dr}}{\dfrac{d(r^2)}{dr}}\right]$$

$$\lim_{r\to 0}\frac{dc}{dr} = \left[\frac{c_i R_A}{(\sinh(\sqrt{\Psi} R_A))}\right]\lim_{r\to 0}\left[\frac{\sqrt{\Psi}\cosh(\sqrt{\Psi} r) + r\Psi \sinh(\sqrt{\Psi} r) - \sqrt{\Psi}\cosh(\sqrt{\Psi} r)}{2r}\right]$$

$$\lim_{r\to 0}\frac{dc}{dr}=\left[\frac{c_i R_A}{(\sinh(\sqrt{\Psi}R_A))}\right]\lim_{r\to 0}\left[\frac{\Psi\sinh(\sqrt{\Psi}r)}{2}\right]$$

$$\lim_{r\to 0}\frac{dc}{dr}=0$$

Therefore, BC2 is also satisfied, and A2 is the solution to A1 subject to the boundary conditions BC1 and BC2.

APPENDIX B1:

MATLAB CODE FOR CATHODE MODEL

Main code

(Cathode-model.m)

Sub-function for solution of differential equations in the catalyst layer

(CLcathode.m)

Sub-function for solution of differential equations in the gas diffusion layer

(GDLcathode.m)

```
%Program: Cathode-model.m
%This program simulates a half-cell polarization curve
%for a PAFC oxygen electrode

%Global variables (common with subfunctions)
global DowGDL DonGDL DnwGDL;
global DkoGDL DkwGDL;
global DowCL DonCL DnwCL;
global DkoCL DkwCL;
global KsE Eeq;
global SAv Io F DoE Ko SOLo dG R Tk;
global NAu Do DoE Ra Lf cH2Ov;

%For exp by Maoka

K=1;
%Density of platinum (g/cm3)
dPt=21.4;

%Density of Carbon (g/cm3)
dC=2;

%Density of PTFE (g/cm3)
dT=2.2;

% Thickness of catalyst layer (cm)
Lc=0.0200;

% Thickness of gas diffusion layer (cm)
Lgdl=0.0600;

% Weight fraction of platinum on catalyst (gPt/g(Pt+C))
WPt=0.05;
%Pt loading (gPt/cm2 electrode)
MPt=0.63*10^-3;


%Percent of acid occupation
PAO=0.40;

%Fraction of pores that are micropores
fm=0.6;

%Agglomerates radius (cm)
Ra=4*10^-4;

%Weight fraction of PTFE (gPTFE/g(PTFE+C+Pt))
WT=0.50;

%PAO for maximum agglomerates utilization
PAOm=0.70;

%Volume fraction of platinum in catalyst layer
VfPt=(MPt)/(Lc*dPt)

%Volume fraction of carbon in catalyst layer
```

```
VfC=(MPt*(1-WPt))/(Lc*dC*WPt)

%Volume fraction of PTFE in catalyst layer
VfT=(WT*MPt)/(Lc*dT*WPt*(1-WT))

%Volume fraction of solid in catalyst layer
VfS=VfPt+VfC+VfT

%Volume fraction of liquid in catalyst layer
VfL=PAO*(1-VfS)

%Volume fraction of gas in catalyst layer
VfG=(1-PAO)*(1-VfS)

%Total volume fraction of agglomerates in the catalyst layer
VfA=(VfPt+VfC)+fm*(1-VfS)

%Agglomerate porosity=volume fraction of micropores in aggl.
VfmA=(fm*(1-VfS))/(VfA)

%Agglomerates density in the catalyst layer (#/cm^3)
NA=VfA/((4/3)*pi*(Ra^3))

%Fraction of agglomerates that are utilized
if PAO<PAOm
u=PAO/PAOm
else
u=1
end

%Utilized agglomerates density(#/cm^3)
NAu=u*NA

%Non-utilized agglomerates density(#/cm^3)
NAnu=(1-u)*NA

%Utilized agglomerates volume fraction
VfAu=u*VfA

%Non-utilized agglomerates volume fraction
VfAnu=(1-u)*VfA

%Volume fraction of liquid films in catalyst layer
VfLF=(1-VfS)*(PAO-u*fm)

%Thickness of liquid films (cm)
Lf=Ra*(((VfLF/VfAu)+1)^(1/3)-1)

if Lf<0
Lf=0
end

%Surface area of Pt per unit mass(cm^2/g)
SA=10^4*(168.3-302.2*WPt+131*WPt^2)

%Surface area of Pt per unit volume of agglomerate(cm^2 Pt/cm^3 agg)
SAv=(SA*MPt)/(Lc*VfA)
```

```
%Faraday's constant (Cb/eq)
F=96487;
%Universal gas constant (J/moleK)
R=8.3143;

%Weight percentage of phosphoric acid(%)
W=96;
%Temperature in degrees Celsius
Tc=190;

%Maximum permissible temperature
Tcmax=2.208*10^-4*W^3-0.01538*W^2+0.4255*W+97.034-5;

%Density of phopsoric acid in g/ml
dens=1.1015+4.7509*10^-3*W-3.9531*10^-4*Tc+4.0019*10^-5*W^2-
4.1692*10^-7*Tc^2-3.671*10^-6*W*Tc;
%Molecular weight of H3PO4 (g/mole)
MW=105;
% Molarity (moles H3PO4/Lt solution)
Mol=(10*W*dens)/MW;

%Temperature in kelvin
Tk=273.15+Tc;

% Mean gas pore radius in gas diffusion layer (cm)
rGDL=5*10^-4;
% Mean gas pore radius in catalyst layer (cm)
rCL=0.5*10^-4;

%Porosity of gas diffusion layer
eGDL=0.60

%Cahode GC total pressure in Pa
P2=101325;
%Total concentration in cathode GC in moles/cm3
CtGC=(10^-6)*P2/(R*Tk);


%Partial pressure of water vapor at the specified Tc,W
xH2Ov=(1/760)*(-30219.6+790.8*W+129.2*Tc-5.075*W^2+0.527*Tc^2-
4.195*Tc*W+0.0301*Tc*W^2-0.00527*Tc^2*W);
%Concentration of water vapor
cH2Ov=CtGC*xH2Ov;

%Mole fractions of gases in cathode gas channel
Xo=(99/100);
Xn=(1/100);

%Molecular weight of water (g/mole)
MMw=18;
%Molecular weight of oxygen (g/mole)
MMo=32;
%Molecular weight of nitrogen (g/mole)
MMn=28;

%Molecular diffusion volumes for estimation of gas binary
```

```
%diffusion coefficients
Sw=13.1;
So=16.3;
Sn=18.5;

% Effective Knudsen diffusion coefficient for oxygen in GDL gas pores
(cm2/s)
DkoGDL=(10^2)*(eGDL^1.5)*(2/3)*rGDL*sqrt(8000*R*Tk/(pi*MMo));
% Effective Knudsen diffusion coefficient for water vapor in GDL gas
pores (cm2/s)
DkwGDL=(10^2)*(eGDL^1.5)*(2/3)*rGDL*sqrt(8000*R*Tk/(pi*MMw));

% Effective Knudsen diffusion coefficient for oxygen in CL gas pores
(cm2/s)

DkoCL=(10^2)*(VfG^1.5)*(2/3)*rCL*sqrt(8000*R*Tk/(pi*MMo));
% Effective Knudsen diffusion coefficient for water vapor in CL gas
pores (cm2/s)
DkwCL=(10^2)*(VfG^1.5)*(2/3)*rCL*sqrt(8000*R*Tk/(pi*MMw));

%Diffusion coefficient between oxygen and water vapor (cm^2/s)
Dow=(0.00143)*(Tk^1.75)/((P2/10^5)*((2*(MMo^-1+MMw^-1)^-
1)^0.5)*(So^(1/3)+Sw^(1/3))^2) ;
%Diffusion coefficient between oxygen and nitrogen (cm^2/s)
Don=(0.00143)*(Tk^1.75)/((P2/10^5)*((2*(MMo^-1+MMn^-1)^-
1)^0.5)*(So^(1/3)+Sn^(1/3))^2) ;
%Diffusion coefficient between nitrogen and water
Dnw=(0.00143)*(Tk^1.75)/((P2/10^5)*((2*(MMn^-1+MMw^-1)^-
1)^0.5)*(Sn^(1/3)+Sw^(1/3))^2) ;

%Effective Diffusion coefficient between oxygen and water vapor in
GDL(cm^2/s)
DowGDL=(eGDL^1.5)*Dow;
%Effective Diffusion coefficient between oxygen and nitrogen in
GDL(cm^2/s)
DonGDL=(eGDL^1.5)*Don;
%Effective Diffusion coefficient between nitrogen and water in GDL
(cm^2/s)
DnwGDL=(eGDL^1.5)*Dnw;

%Effective Diffusion coefficient between oxygen and water vapor in
CL(cm^2/s)
DowCL=(VfG^1.5)*Dow;
%Effective Diffusion coefficient between oxygen and nitrogen in
CL(cm^2/s)
DonCL=(VfG^1.5)*Don;
%Effective Diffusion coefficient between nitrogen and water in CL
(cm^2/s)
DnwCL=(VfG^1.5)*Dnw;

% Diffusion coefficient of oxygen in the electrolyte (cm^2/s)
Do=0.048*exp(-25769/(R*Tk)+0.034*(98-W));
% Effective Diffusion coefficient of oxygen in the agglomerates
(cm^2/s)
DoE=(VfmA^1.5)*Do;

%Equilibrium voltage at the specified temperature for the ORR
```

```
Eeq=-4.184*(-70650-8*Tk*log(Tk)+92.84*Tk)/(2*F);

% Solubility of oxygen at 1 atm partial oxygen pressure (moles/cm3atm)
SOLo=(6.8646-0.0617*W)*2*10^-6*exp(-9162/(R*Tk));
if Tk>373K
SOLo=(6.8646-0.0617*W)*10^-7;
end

% Henry's law constant defined as solubility of oxygen
% in moles/cm3 in liquid per moles/cm3 in gas
Ko=(R*Tk/101350)*10^6*SOLo;

%Specific conductivity of phosphoric acid (S/cm)
Ks=((8.53*10^-5*W^2-0.0184*W+1.034)*(1+((4.44*10^-6*W^2-1.01*10^-
4*W+0.0114)*(Tc-25))));
%Effective specific conductivity in catalyst layer (S/cm)
KsE=(VfL^1.5)*Ks;

%Activation energy for the exchange current density for ORR (J/mole)
dG=92000;
%Reference exchange current density for ORR (Amp/cm2)
Ioo=1*10^-13;
%Exchange current density for the ORR at the specified temperature
Io=Ioo*exp((dG/R)*(298^-1-Tk^-1));

%Solution intervals
xspanCL=[0 Lc];
xspanGDL=[0 Lgdl];

%Potential in the solid (starting point)
CathVolt=0.95;

optsuper=[];
n2super=[0];
VCP=[];

opt=0.0000001;
last=1

%Voltage step
StepVolt=0.001;

while last==1|(VCP(end,1)>0&VCP(end,2)<10000);
cond=[1 1];
jjj=1;
options = odeset('RelTol',10^-9);

while max(abs((cond(1,1))))>10^-9
optPert=opt;
optPert=optPert+(10^-9)*optPert;
optPert=[opt optPert];
for i=1:2
opt=optPert(1,i);

%Cathode gas diffusion layer solver
%Initial(boundary values)
yGDL0=[opt(1);Xo*CtGC;cH2Ov;Xn*CtGC];
```

```
%The variables represent:
%yGDL(1): Flux of oxygen(moles/cm^2)
%yGDL(2): Concentration of oxygen in gas(moles/cm^3)
%yGDL(3): Concentration of water vapor in gas(moles/cm^3)
%yGDL(4): Concentration of nitrogen in gas(moles/cm^3)

%Apply solver function GDLcathode
solGDL=ode23(@GDLcathode,xspanGDL,yGDL0,options);
%Apply solver function f4
xGDL=[0:solGDL.x(end)/100:solGDL.x(end)];
yGDL=[deval(solGDL,xGDL)]';

%Cathode catalyst layer solver
%Initial(boundary values)

yCL0=[yGDL(end,1);yGDL(end,2);yGDL(end,3);yGDL(end,4);0;0;CathVolt];
%The variables represent:
%yCL(1): Flux of oxygen(moles/cm^2)
%yCL(2): Concentration of oxygen(moles/cm^3)
%yCL(3): Concentration of water vapor(moles/cm^3)
%yCL(4): Concentration of nitrogen(moles/cm^3)
%yCL(5): The electrical potential in the electrolyte(V)
%yCL(6): Ionic current density(amp/cm^2)
%yCL(7): Electrical potential in the solid phase(Fi solid)(V)

%Apply solver function
solCL=ode45(@CLcathode,xspanCL,yCL0,options);
xCL=[0:solCL.x(end)/100:solCL.x(end)];
yCL=[deval(solCL,xCL)]';

n=yCL(:,7)-yCL(:,5)-Eeq;
L=-((SAv*Io/(4*F*DoE*SOLo)).*(exp((F.*n)./(R*Tk))-exp((-
F.*n)./(R*Tk))));


RocNum=NAu.*(4.*pi.*Do.*DoE.*Ko.*Ra*(Ra+Lf).*yCL(:,2).*((sqrt(L).*
Ra.*coth(sqrt(L).*Ra))-1));

RocDen=Do.*(Ra+Lf)+DoE.*Lf.*(sqrt(L).*Ra.*coth(sqrt(L).*Ra)-1);
Roc=RocNum./RocDen;

%Volumetric current consumption rate in the cathode CL(amp/cm3)
Iv=4*F*Roc;

%Integral of current over the CL, cathode
intRoc=trapz(xCL',Roc);
intIv=trapz(xCL',Iv);

cond(1,i)=(yCL(end,1))/K;
end

J=0;
J=(cond(1,2)-cond(1,1))/(optPert(1,2)-optPert(1,1));

if isnan(J)
CathVolt=last-StepVolt/1.5
StepVolt=StepVolt/1.5
```

```
cond(1,1)=1;
else
Dopt=(-cond(1,1))/J;
%Calculate correction for iteration i
opt=optPert(1,1)+Dopt;

%Set new vector of variables to be optimized
optall(1,jjj)=opt;
condall(1,jjj)=cond(1,1);
jjj=jjj+1
end
end

optsuper=[optsuper opt];
newVCP=[(yCL(1,7)-yCL(end,5)) 1000*intIv Eeq-(yCL(1,7)-yCL(end,5)) ];
VCP=[VCP;newVCP];
last=CathVolt;
CathVolt=CathVolt-StepVolt
K=yCL(1,1);
end

semilogx(VCP(:,2),VCP(:,1),'k');
text(VCP(end,2),VCP(end,1),'(1)')
hold on
```

```
% Program: CLcathode.m
% Sub-function for solution of differential equation in cathode
catalyst layer


function dyCLdt2=CLcathode(t2, yCL)
%Solver function for the cathode catalyst layer



global DowCL DonCL DnwCL;
global DkoCL DkwCL;
global KsE Eeq;
global SAv Io F DoE SOLo dG R Tk;
global NAu Do DoE Ko Ra Lf;



Nw=-2*yCL(1);
%Flux of water vapour


Ct=yCL(2)+yCL(3)+yCL(4);
%Total concentration


n2=yCL(7)-yCL(5)-Eeq;
%Overpotential



%Auxiliary parameter
L2=-((SAv*Io/(4*F*DoE*SOLo))*(exp((F*n2)/(R*Tk))-exp((-F*n2)/(R*Tk))));

%Rate of oxygen consumption
% Numerator

RocNum=NAu*(4*pi*Do*DoE*Ko*Ra*(Ra+Lf)*yCL(2)*((sqrt(L2)*Ra*coth(sqrt(L2
)*Ra))-1));

% Denominator
RocDen=Do*(Ra+Lf)+DoE*Lf*(sqrt(L2)*Ra*coth(sqrt(L2)*Ra)-1);


Roc2=RocNum/RocDen;


Iv2=4*F*Roc2;
```

```
dyCLdt2=[-Roc2
-(yCL(1)/DkoCL+yCL(3)*yCL(1)/(DowCL*Ct)-
yCL(2)*Nw/(DowCL*Ct)+yCL(4)*yCL(1)/(DonCL*Ct))
0
(yCL(4)*yCL(1)/(DonCL*Ct)+yCL(4)*Nw/(DnwCL*Ct))
(1/KsE)*yCL(6)
Iv2
0];
```

```
%Program GDLcathode.m
%Sub-function for solution of differential equations in cathode Gas-
diffusion layer

function dyGDLdt=GDLcathode(t,yGDL)
%Solver function for the cathode Gas Diffusion Layer

global DowGDL DonGDL DnwGDL;
global DkoGDL DkwGDL;

%Flux of water vapor
Nw=-2*yGDL(1);
%Total concentration
Ct=yGDL(2)+yGDL(3)+yGDL(4);

dyGDLdt=[0
-(yGDL(1)/DkoGDL+yGDL(3)*yGDL(1)/(DowGDL*Ct)-...
yGDL(2)*Nw/(DowGDL*Ct)+yGDL(4)*yGDL(1)/(DonGDL*Ct))
0
yGDL(4)*yGDL(1)/(DonGDL*Ct)+yGDL(3)*Nw/(DnwGDL*Ct) ];
```

APPENDIX B2:

MATLAB CODE FOR ANODE MODEL

Main code
(Anode-model.m)

Sub-function for solution of differential equations in the catalyst layer
(CLanode.m)

Sub-function for solution of differential equations in the gas diffusion layer
(GDLanode.m)

```
% Program: Anode-model.m
% This program simulates a half-cell polarizarion curve for a
% propane anode electrode

% Global variables (common with subfunctions)
global DpcGDL DpwGDL DcwGDL;
global DkpGDL DkcGDL;
global DpcCL DpwCL DcwCL;
global DkpCL DkcCL;
global KsE Eeq;
global SAv Io F DpE Kp SOLp dG R Tk;
global NAu Dp DpE Ra Lf cH2Ov aw;

K=1;
%Density of platinum (g/cm3)
dPt=21.4;

%Density of Carbon (g/cm3)
dC=2;

%Density of PTFE (g/cm3)
dT=2.2;

% Thickness of catalyst layer (cm)
Lc=0.0300;
%Pt loading (gPt/cm2 electrode)
MPt=4*10^-3;
% Weight fraction of platinum on catalyst (gPt/g(Pt+C))
WPt=0.40;
%Anode GC total pressure in Pa
P1=101325;
%Weight percentage of phosphoric acid(%)
W=95;
%Temperature in degrees Celsius
Tc=200;
%Mole fractions of gases in cathode gas channel
Xp=(80/100);
Xc=(20/100);

% Thickness of gas diffusion layer (cm)
Lgdl=0.0200;
%Percent of acid occupation
PAO=0.60;

%Fraction of pores that are micropores
fm=0.6;

%Agglomerates radius (cm)
Ra=10^-4;

%Weight fraction of PTFE (gPTFE/g(PTFE+C+Pt))
WT=0.50;

%PAO for maximum agglomerates utilization
PAOm=0.70;

%Volume fraction of platinum in catalyst layer
```

```
VfPt=(MPt)/(Lc*dPt)

%Volume fraction of carbon in catalyst layer
VfC=(MPt*(1-WPt))/(Lc*dC*WPt)

%Volume fraction of PTFE in catalyst layer
VfT=(WT*MPt)/(Lc*dT*WPt*(1-WT))

%Volume fraction of solid in catalyst layer
VfS=VfPt+VfC+VfT

%Volume fraction of liquid in catalyst layer
VfL=PAO*(1-VfS)

%Volume fraction of gas in catalyst layer
VfG=(1-PAO)*(1-VfS)

%Total volume fraction of agglomerates in the catalyst layer
VfA=(VfPt+VfC)+fm*(1-VfS)

%Agglomerate porosity=volume fraction of micropores in aggl.
VfmA=(fm*(1-VfS))/(VfA)

%Agglomerates density in the catalyst layer (#/cm^3)
NA=VfA/((4/3)*pi*(Ra^3))

%Fraction of agglomerates that are utilized
if PAO<PAOm
u=PAO/PAOm
else
u=1
end

%Utilized agglomerates density(#/cm^3)
NAu=u*NA

%Non-utilized agglomerates density(#/cm^3)
NAnu=(1-u)*NA

%Utilized agglomerates volume fraction
VfAu=u*VfA

%Non-utilized agglomerates volume fraction
VfAnu=(1-u)*VfA

%Volume fraction of liquid films in catalyst layer
VfLF=(1-VfS)*(PAO-u*fm)

%Thickness of liquid films (cm)
Lf=Ra*(((VfLF/VfAu)+1)^(1/3)-1)

if Lf<0
Lf=0
end

%Surface area of Pt per unit mass(cm^2/g)
SA=10^4*(131*WPt^2-302.2*WPt+168.33)
```

```
%Surface area of Pt per unit volume of agglomerate(cm^2 Pt/cm^3 agg)
SAv=(SA*MPt)/(Lc*VfA)

%Faraday's constant (Cb/eq)
F=96487;
%Universal gas constant (J/moleK)
R=8.3143;

%Maximum permissible temperature
Tcmax=2.208*10^-4*W^3-0.01538*W^2+0.4255*W+97.034-5;

%Molality of phosphoric acid solution
m=0.3714*exp(0.0591*W);
%Activity of water in solution
aw=0.8701*exp(-0.0394*m);

%Temperature in kelvin
Tk=273.15+Tc;

% Mean gas pore radius in gas diffusion layer (cm)
rGDL=5*10^-4;
% Mean gas pore radius in catalyst layer (cm)
rCL=0.5*10^-4;

%Porosity of gas diffusion layer
eGDL=0.60
%Total concentration in cathode GC in moles/cm3
CtGC=(10^-6)*P1/(R*Tk);

%Partial pressure of water vapor at the specified Tc,W
xH2Ov= (1/760)*(-62.671+3044*(W/100)-2990*(Tc/100)-
5176.9*(W/100)^2+3530.8*(Tc/100)^2+2193.9*(W/100)^3+109.07*(Tc/100)^3+
2333.6*(Tc/100)*(W/100)+724.64*(Tc/100)*(W/100)^2-
3704*(Tc/100)^2*(W/100));
%Concentration of water vapor
cH2Ov=CtGC*xH2Ov;

%Molecular weight of water (g/mole)
MMw=18;
%Molecular weight of propane(g/mole)
MMp=44;
%Molecular weight of carbon dioxide
MMc=44;

%Molecular diffusion volumes for estimation of gas binary
%diffusion coefficients
Sp=66.2;
Sc=26.9;
Sw=13.1;

% Effective Knudsen diffusion coefficient for propane in GDL gas pores
(cm2/s)
DkpGDL=(10^2)*(eGDL^1.5)*(2/3)*rGDL*sqrt(8000*R*Tk/(pi*MMp));
% Effective Knudsen diffusion coefficient for carbon dioxide in GDL gas
pores (cm2/s)
```

```
DkcGDL=(10^2)*(eGDL^1.5)*(2/3)*rGDL*sqrt(8000*R*Tk/(pi*MMc));

% Effective Knudsen diffusion coefficient for propane in CL gas pores
(cm2/s)

DkpCL=(10^2)*(VfG^1.5)*(2/3)*rCL*sqrt(8000*R*Tk/(pi*MMp));
% Effective Knudsen diffusion coefficient for carbon dioxide in CL gas
pores (cm2/s)

DkcCL=(10^2)*(VfG^1.5)*(2/3)*rCL*sqrt(8000*R*Tk/(pi*MMc));

Dpc=(0.00143)*(Tk^1.75)/((P1/10^5)*(2*((MMp^-1+MMc^-1)^-
1)^0.5)*(Sp^(1/3)+Sc^(1/3))^2) ;
%Diffusion coefficient between P and CO2(cm2/s)
Dpw=(0.00143)*(Tk^1.75)/((P1/10^5)*(2*((MMp^-1+MMw^-1)^-
1)^0.5)*(Sp^(1/3)+Sw^(1/3))^2);
%Diffusion coefficient between P and H2O(cm2/s)
Dcw=(0.00143)*(Tk^1.75)/((P1/10^5)*((2*(MMc^-1+MMw^-1)^-
1)^0.5)*(Sc^(1/3)+Sw^(1/3))^2) ;
%Diffusion coefficient between CO2 and water(cm2/s)

%Effective Diffusion coefficient between P and CO2 in GDL(cm^2/s)
DpcGDL=(eGDL^1.5)*Dpc;
%Effective Diffusion coefficient between P and H2O in GDL(cm^2/s)
DpwGDL=(eGDL^1.5)*Dpw;
%Effective Diffusion coefficient between CO2 and water in GDL (cm^2/s)
DcwGDL=(eGDL^1.5)*Dcw;

%Effective Diffusion coefficient between P and CO2 in CL(cm^2/s)
DpcCL=(VfG^1.5)*Dpc;
%Effective Diffusion coefficient between P and H2O in CL(cm^2/s)
DpwCL=(VfG^1.5)*Dpw;
%Effective Diffusion coefficient between CO2 and H2O in CL (cm^2/s)
DcwCL=(VfG^1.5)*Dcw;

% Diffusion coefficient of oxygen in the electrolyte (cm^2/s)
Dp=0.38*0.048*exp(-25769/(R*Tk)+0.034*(98-W));
%Effective Diffusion coefficient of oxygen in the agglomerates (cm^2/s)
DpE=(VfmA^1.5)*Dp;

%Equilibrium voltage at the specified temperature
Eeq=-4.184*(-70650-8*Tk*log(Tk)+92.84*Tk)/(2*F)-1.08

% Solubility of oxygen at 1 atm partial oxygen pressure (moles/cm3atm)
SOLp=1.75*10^-7;

% Henry's law constant defined as solubility of oxygen
% in moles/cm3 in liquid per moles/cm3 in gas
Kp=(R*Tk/101350)*10^6*SOLp;

%Specific conductivity of phosphoric acid (S/cm)
Ks=((8.529*10^-5*W^2-0.01838*W+1.035)*(1+((4.444*10^-6*W^2-
1.012*10^-4*W+0.01139)*(Tc-25))));
%Effective specific conductivity in catalyst layer (S/cm)
KsE=(VfL^1.5)*Ks;
```

```
%Activation energy for the exchange current density for propane
oxidation (J/mole)
dG=90000;
%Reference exchange current density for propane oxidation (Amp/cm2)
Ioo=10^-8;
%Exchange current density for the ORR at the specified temperature
Io=Ioo*exp((dG/R)*(423^-1-Tk^-1));

%Solution intervals
xspanCL=[0 Lc];
xspanGDL=[0 Lgdl];

%Potential in the solid (starting point)
AnSolVolt=0.15;

optsuper=[];
n2super=[0];
VCP=[];

opt=0.00000001;
last=1

%Voltage step
StepVolt=0.01;

while last==1|(VCP(end,1)<1&VCP(end,2)<1100);
cond=[1 1];
jjj=1;
options = odeset('RelTol',10^-9);

while max(abs((cond(1,1))))>10^-12
optPert=opt;
optPert=optPert+(10^-9)*optPert;
optPert=[opt optPert];
for i=1:2
opt=optPert(1,i);

%Anode gas diffusion layer solver
%Initial(boundary values)
yGDL0=[opt(1);Xp*CtGC;Xc*CtGC;cH2Ov];
%The variables represent:
%yGDL(1): Flux of propane (moles/cm^2)
%yGDL(2): Concentration of propane in gas(moles/cm^3)
%yGDL(3): Concentration of carbon dioxide in gas(moles/cm^3)
%yGDL(4): Concentration of water vapor in gas(moles/cm^3)


%Apply solver function GDLanode
solGDL=ode23(@GDLanode,xspanGDL,yGDL0,options);
%Apply solver function f4
xGDL=[0:solGDL.x(end)/100:solGDL.x(end)];
yGDL=[deval(solGDL,xGDL)]';

%Anode catalyst layer solver
%Initial(boundary values)

yCL0=[yGDL(end,1);yGDL(end,2);yGDL(end,3);yGDL(end,4);0;0;AnSolVolt];
```

```
%The variables represent:
%yCL(1): Flux of propane(moles/cm^2)
%yCL(2): Concentration of propane(moles/cm^3)
%yCL(3): Concentration of carbon dioxide(moles/cm^3)
%yCL(4): Concentration of water vapor(moles/cm^3)
%yCL(5): The electrical potential in the electrolyte(V)
%yCL(6): Ionic current density(amp/cm^2)
%yCL(7): Electrical potential in the solid phase(Fi solid)(V)


%Apply solver function f4
solCL=ode45(@CLanode,xspanCL,yCL0,options);
xCL=[0:solCL.x(end)/100:solCL.x(end)];
yCL=[deval(solCL,xCL)]';

n=yCL(:,7)-yCL(:,5)-Eeq;

L=((SAv*Io/(20*F*DpE*SOLp)).*(exp((F.*n)./(R*Tk))));


RpcNum=NAu.*aw.*(4.*pi.*Dp.*DpE.*Kp.*Ra*(Ra+Lf).*yCL(:,2).*
 ((sqrt(L).*Ra.*coth(sqrt(L).*Ra))-1));

RpcDen=Dp.*(Ra+Lf)+DpE.*Lf.*(sqrt(L).*Ra.*coth(sqrt(L).*Ra)-1);
Rpc=RpcNum./RpcDen;

%Volumetric current consumption rate in the cathode CL(amp/cm3)
Iv=20*F*Rpc;

%Integral of current over the CL, cathode
intRpc=trapz(xCL',Rpc);
intIv=trapz(xCL',Iv);

cond(1,i)=(yCL(end,1))/K;
end

J=0;
J=(cond(1,2)-cond(1,1))/(optPert(1,2)-optPert(1,1));

if isnan(J)
AnSolVolt=last+StepVolt/1.5
StepVolt=StepVolt/1.5

cond(1,1)=1;

else
Dopt=(-cond(1,1))/J;
%Calculate correction for iteration i
opt=optPert(1,1)+Dopt;

%Set new vector of variables to be optimized
optall(1,jjj)=opt;
condall(1,jjj)=cond(1,1);
jjj=jjj+1
end
end
```

```
optsuper=[optsuper opt];
newVCP=[(yCL(1,7)-yCL(end,5)) 1000*intIv (yCL(1,7)-yCL(end,5))-Eeq];
VCP=[VCP;newVCP];
last=AnSolVolt;
AnSolVolt=AnSolVolt+StepVolt
K=yCL(1,1);

end
figure(1)
plot(VCP(:,2),VCP(:,1),'k');
text(VCP(end,2),VCP(end,1),'(8)')

current=[1:5:1005]';
voltage=interp1(VCP(:,2),VCP(:,1),current)
```

```
%Program: CLanode.m
%Sub-function for differential equations in anode catalyst layer



function dyCLdt2=CLanode(t2,yCL)
%Solver function for the cathode catalyst layer



% Global variables (common with subfunctions)
global DpcGDL DpwGDL DcwGDL;
global DkpGDL DkcGDL;
global DpcCL DpwCL DcwCL;
global DkpCL DkcCL;
global KsE Eeq;
global SAv Io F DpE Kp SOLp dG R Tk;
global NAu Dp DpE Ra Lf cH2Ov aw;



Nc=-3*yCL(1);
%Flux of water vapour


Ct=yCL(2)+yCL(3)+yCL(4);

%Total concentration


n1=yCL(7)-yCL(5)-Eeq;
%Overpotential



%Auxiliary parameter
L1=((SAv*Io/(20*F*DpE*SOLp))*(exp((F*n1)/(R*Tk))));



%Rate of oxygen consumption
%Numerator
RpcNum=NAu*(aw)*(4*pi*Dp*DpE*Kp*Ra*(Ra+Lf)*yCL(2)*((sqrt(L1)*Ra*coth(
sqrt(L1)*Ra))-1));


%Denominator
RpcDen=Dp*(Ra+Lf)+DpE*Lf*(sqrt(L1)*Ra*coth(sqrt(L1)*Ra)-1);
```

```
Rpc1=RpcNum/RpcDen;



Iv1=20*F*Rpc1;



dyCLdt2=[-Rpc1
-(yCL(1)/DkpCL+yCL(3)*yCL(1)/(DpcCL*Ct)-
yCL(2)*Nc/(DpcCL*Ct)+yCL(4)*yCL(1)/(DpwCL*Ct))
-(Nc/DkcCL+yCL(2)*Nc/(DpcCL*Ct)-
yCL(3)*yCL(1)/(DpcCL*Ct)+yCL(4)*Nc/(DcwCL*Ct))
0
-(1/KsE)*yCL(6)
Iv1
0];
```

```
%Program: GDLanode.m
%Sub-function for differential equations in anode Gas Diffusion Layer


function dyGDLdt=GDLanode(t,yGDL)


%Solver function for the cathode Gas Diffusion Layer
%Global variables (common with subfunctions)


global DpcGDL DpwGDL DcwGDL;
global DkpGDL DkcGDL;
global DpcCL DpwCL DcwCL;
global DkpCL DkcCL;
global KsE Eeq;
global SAv Io F DpE Kp SOLp dG R Tk;
global NAu Dp DpE Ra Lf cH2Ov aw;


%Flux of water vapor
Nc=-3*yGDL(1);
%Total concentration
Ct=yGDL(2)+yGDL(3)+yGDL(4);


dyGDLdt=[0
        -(yGDL(1)/DkpGDL+yGDL(3)*yGDL(1)/(DpcGDL*Ct)-
yGDL(2)*Nc/(DpcGDL*Ct)+yGDL(4)*yGDL(1)/(DpwGDL*Ct))
        -(Nc/DkcGDL+yGDL(2)*Nc/(DpcGDL*Ct)-
yGDL(3)*yGDL(1)/(DpcGDL*Ct)+yGDL(4)*Nc/(DcwGDL*Ct))
        0];
```

APPENDIX B3:

MATLAB CODE FOR POTENTIAL DROP IN THE ELECTROLYTE LAYER

```
% Program: IRdrop.m
% This code calculates the iR-drop in the electrolyte layer of a PAFC

W=95;
Tc=200;
Tk=273.15+Tc;
Lel=0.0250;
current=[1:5:1005]'
Ks=((8.529*10^-5*W^2-0.01838*W+1.035)*(1+((4.444*10^-6*W^2-1.012*10^-
4*W+0.01139)*(Tc-25))));
voltage=(current./1000).*(Lel)/(Ks)
```

REFERENCES

Appleby, A.J. and Foulkes, F.R., *Fuel Cell Handbook*, van Nostrand-Reinhold, New York (1989)

Appleby, A.J. in *Modern Aspects of Electrochemistry*, Vol.9, Conway, B.E. and Bockris, J.O'M, Editors, p.369, Plenum Press, New York (1974)

Appleby, A.J., *J.Electrochem.Soc.* **117** (3), 328 (1970)

Austin, L.G. and Lerner, H, *Electrochim. Acta* **9**, 1469 (1964)

Austin, L.G., Ariet, M., Walker, R.D., Wood, G.B. and Comyn, R.H., *Ind.Eng.Chem.Funda.***4**, 321 (1965)

Bacon, F.T., in *Fuel Cells*, Vol.1, Chap. 5, Young, G.J., Editor, Reinhold Publishing Corporation, New York, 1960

Baur, E., *Z. Elektrochem.* **16**, 300 (1910)

Bernardi, D.M. and Verbrugge, M.W., *J.Electrochem.Soc.***139** (11), 2477 (1992)

Bird, R.B., Stewart, W.E. and Lightfoot, E.N., *Transport phenomena*, John Wiley & Sons, New York, (1960)

Bjornbom, P., *Electrochim.Acta* **32** (1), 115 (1987)

Bockris, J.O'M and Srinivasan, S., *Fuel Cells: Their Electrochemistry*, McGraw-Hill, Inc., New York (1969)

Brown, R. and Rockett, J.A., *J.Electrochem. Soc.* **113**, 865 (1966)

Burshtein, R.C., Markin, V.S., Pshinichnikov, A.G., Chismadgey, V.A. and Chirkov, Y.G.,*Electrochim. Acta* **9**, 773 (1964)

Caires, M.I., Buzzo, M.L., Ticianelli E.A. and Gonzalez, E.R., *J.Appl.Electrochem.* **27**, 19 (1997)

Cairns, E.J. in *Advances in Electrochemistry and Electrochemical Engineering Vol.8*, Delahay, P. and Tobias, C.W., Editors, p.339, John Wiley & Sons, New York (1971)

Cameron, D.S., *Platinum Metals Rev.* **47** (1), 28 (2003)

Carrette, L., Friedrich,K.A., and Stimming, U., *Fuel Cells* **1** (1), 5 (2001)

Choudhury, S.R., Deshmukh, M.B. and Rengswamy, R., *Journal of Power Sources* **112**, 137 (2002)

Cutlip, M.B., *Electrochim. Acta* **20**, 767 (1975)

Cutlip, M.B., Yang, S.C. and Stonehart P., *Electrochim. Acta* **36**, 547, 1991

Damjanovic, A., in *Modern Aspects of Electrochemistry*, Bockris, J.O'M. and Conway, B.E., Editors, Plenum Press, New York, 369 (1989)

Damjanovic, A. and Sepa, D.B., *Electrochim. Acta* **35** (7), 1157, 1989

De Sena, D.R., Gonzalez, E.R. and Ticianelli, E.T. , *Electrochim.Acta* **37** (10), 1855 (1992)

Dobos, D., *Electrochemical data*, Elsevier, New York (1975)

E-TEK Corporation website: www.etek-inc.com

Fuller, T.F., Luczak F.J. and Wheeler, D.J., *J.Electrochem. Soc*, **142** (6), 1752-1757, (1995)

Gard, D.R. in *Kirk Othmer Encyclopedia of Chemical Technology*, 4th ed., Kroschwitz, J.I. and Howe-Grant, M., Editors, v.18, John Wiley & Sons, New York (1991)

Geankoplis, C.J., *Mass Transport Phenomena*, Holt, Rinehart and Winston, New York, (1972)

Giner, J. and Hunter, C., *J.Electrochem. Soc.* **116**, 1124 (1969)

Giordano, N., Passalacqua, E., Alderucci, V., Staiti, P., Lino, P., Mirzaian, H., Taylor E.J. and Wilemski, G., *Electrochim.Acta* **36** (5/6), 1049 (1991)

Glass, J.T, Cahen, G.L.Jr., and Stoner, G.E., *J.Electrochem. Soc.* **136** (3), 657 (1989)

Gordon, A.J. and Ford, R.A., *The chemist's companion: a handbook of practical data, techniques and references*, John Wiley and Sons, New York (1970)

Grens, E.A., *Ind.Eng.Chem.Funda.***5**, 542 (1966)

Grove, W.R., *Phil.Mag.***14**, 127 (1839); **21**, 417 (1842)

Grove, W.R., *Phil.Mag.***21**, 417 (1842)

Grubb, W.T. and Michalske, C.J., *J.Electrochem.Soc.* **111** (9), 1015 (1964)

Gubbins, K.E. and Walker, K.E., Jr., *J.Electrochem.Soc.* **112** (5) (19), 469 (1965)

Haber, F. and Moser, A., *Z.Elektrochem.***11**, 593 (1905)

Hahn F. and Melendres C.A., *Electrochimica Acta* **46**, 3525 (2001)

Hirschenhofer, J.H., Stauffer, D.B., Engleman, R.R., and Klett, M.G., *Fuel Cell Handbook*, 4th Ed., Parsons, Inc., under contrant No. DE-AC21-94MC31166, 1998

Honji, A., Mori, T., Tamura, K., and Hishinuma, Y., *J.Electrochem.Soc.***135** (2), 355 (1988)

Iczkowski, R.P. and Cutlip, M.B, *J. Electrochem. Soc.* **127** (7), 1433 (1980)

Iliev, I., Gamburzev, S., Kaisheva, A. and Mrha, J., *J.Appl.Electrochem.* **5**, 291 (1975)

Jacques, W.W., Harper's magazine **94**, 144 (1896)

Kulikovsky, A.A., Divisek, J. and Kornyshev, A.A., *J.Electrochem.Soc.* **146** (11), 3981 (1999)

Kunz, H.R. and Gruver, H.R., *Electrochim.Acta* **23**, 219-222 (1978)

Kunz, H.R. and Gruver, H.R., *J.Electrochem.Soc.***122** (10), 1279-1287 (1975)

Liebhafsky, H.A. and Cairns, E.J., *Fuel Cells and Fuel Batteries*, John Wiley & Sons, 458 (1968)

Maggio, G., *Journal of Applied Electrochemistry* **29**, 171 (1999)

Maja, M., Tosco, P. and Vanni M., *J.Electrochem.Soc.***148**, A1368 (2001)

Maoka, T., *Electrochim.Acta* **33** (3), 371 (1988)

Markovic, N.M., Schmidt, T.J., Stamenkovic, V.and Ross, P.N., *Fuel Cells* **1** (2), 105 (2001)

Mond, L. and Langer, C., *Proc. Roy. Soc., London,* **46**, 296 (1889)

Newman, J. and Tiedermann, W., *AiChE J.***21**, 25 (1975)

Newman, J., *Electrochemical Systems*, Prentice-Hall Inc., Englewood Cliffs, NJ (1973)

Newman, J.S. and Tobias, C.W., *J.Electrochem.Soc.***109**, 1183 (1962)

Niedrach, L.W. and Alford, H.R., *J.Electrochem. Soc.* **112** (2), 117 (1965)

Perry, M.L., Newman, J. and Cairns, J.E., *J.Electrochem. Soc.* **145**(1) 4 (1998)

Poling, B.E., Prausnitz, J.M. and O'Connell, J.P., *The properties of gases and liquids*, 5th ed., McGraw-Hill, New York (2001)

Ralph, T.R. and Hogarth, M.P., *Platinum Metals Review* **46**(1), 3 (2002)

Ross, P.N., *J.Electrochem. Soc.* **127**, 2655 (1980)

Rothfeld, L.B., *A.I.Ch.E. Journal*, **9** (1), 1963

Savadogo O. and Rodriguez Varela, F.J., *Journal of New Materials for Electrochemical Systems* **4**, 93 (2001)

Scharifker, B.R., Zelenay, P. and Bockris, J.O'M., *J.Electrochem.Soc.***134** (11), 2714 (1987)

Schmid, A., *Die Diffusiongaselectrode*, Ferninand Enke, Stuttgart, 1923

Srinivasan S., Hurwitz H.D. and Bockris J.O'M, *J. Chem. Phys.* **46**, 3108 (1967)

Stonehart, P., *Electrochim. Acta* **17**, 2333 (1972)

Sugishima, N., Hinatsu, J.T., and Foulkes, F.R., *J.Electrochem.Soc.***141** (12), 3332 (1994)

Tarasevich, M.R., Sadkowski, A. and Yeager, E., in *Comprehensive Treatise of Eletrochemistry*, Bockris, J.O.M., Conway, B.E., Yeager, E., Khan, S.U.M. and White, R.E., Editors, Plenum Press, New York, 369 (1983)

Vogel,W., Lundquist, J. and Bradford, A., *Electrochim. Acta* **17**, 1735 (1972)

Watanabe, M., Sei, H. and Stonehart, P., *J. Electroanal. Chem.* **261**, 375 (1989)

Will, F.G., *J.Electrochem. Soc.* **110**, 152 (1963)

Yamashita, K. and Taniguchi, T., *J.Electrochem.Soc.***145** (1), 44 (1998)

Yang, S.C., Cutlip, P. and Stonehart, P., *Electrochim. Acta* **34**, 703 (1989)

Yang, S.C., Cutlip, P. and Stonehart, P., *Electrochim. Acta* **35**, 869 (1990)

Yang, S.C., *J.Electrochem. Soc.* **147**, 71 (2000)